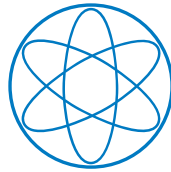


PHYSIK-DEPARTMENT



Monte Carlo Simulation Studies
and Image Reconstruction Methods
for a Small Animal PET Scanner

Dissertation

von

Melanie Hohberg



TECHNISCHE UNIVERSITÄT MÜNCHEN

TECHNISCHE UNIVERSITÄT MÜNCHEN

Lehrstuhl für Experimentalphysik E21

Monte Carlo Simulation Studies
and Image Reconstruction Methods
for a Small Animal PET Scanner

Melanie Hohberg

Vollständiger Abdruck der von der Fakultät für Physik der Technischen
Universität München zur Erlangung des akademischen Grades eines

Doktors der Naturwissenschaften (Dr. rer. nat.)

genehmigten Dissertation

Vorsitzender:

Univ.-Prof. Dr. P. Vogl

Prüfer der Dissertation:

1. apl. Prof. Dr. S. Ziegler

2. Univ.-Prof. Dr. P. Böni

Die Dissertation wurde am 23.10.2012 bei der Technischen Universität
München eingereicht und durch die Fakultät für Physik am 18.12.2012
angenommen.

Zusammenfassung

Die Positronen-Emissions-Tomographie (PET) ist ein nicht-invasives, mehrdimensionales bildgebend Verfahren zur Darstellung physiologischer Prozesse, welches in der Medizin die Diagnose von Krebs, kardiologischen oder neurologischen Erkrankungen ermöglicht. Um neben der physiologischen Information auch eine anatomische Zuordnung zu erhalten, wird PET häufig in der klinischen Routine mit der Computertomographie (CT) kombiniert. Allerdings erfolgt die Datenaufnahme bei kombinierten PET/CT-Geräten sequenziell und die Bildfusion beider Modalitäten erfolgt per Software. Viele Anstrengungen wurden unternommen um die Kombination von PET mit der Magnet-Resonanztomographie (MRT) in einem voll-integrierten System mit simultaner Datenaufnahme beider Modalitäten zu ermöglichen, da die MRT einen besseren Gewebeweichteilkontrast bietet und keine zusätzliche Strahlenbelastung mit sich bringt. Ein kombiniertes PET/MRT-Gerät erfordert allerdings ein technisch anspruchsvolleres Detektorkonzept, welches nicht zu Interferenzen zwischen beiden Modalitäten führt und auch unter Einfluss starker magnetischer Felder funktioniert.

Silizium-Photomultiplier (SiPM) stellen ein neuartiges Detektorkonzept dar, welches sich für kombinierte PET/MRT-Geräte eignet, da sie eine hohe Signalverstärkung, ein schnelles Ansprechverhalten besitzen und unempfindlich gegenüber magnetischen Feldern sind. Basierend auf diesem neuen Detektorkonzept wurde ein Kleintier-PET-Scanner, MADPET-3, entwickelt. Der MADPET-3-Prototyp besteht aus zwei Detektormodulen mit jeweils einer 8×4 Matrix monolithischer SiPMs, die individuell mit Lutetium-Yttrium-Oxyorthosilikat (LYSO) Szintillationskristallen ausgelesen werden. Um eine möglichst hohe Sensitivität und gleichzeitig eine hohe Ortsauflösung zu erreichen, wurde für die Szintillationskristalle eine aussergewöhnliche Geometrie ($1.0 \times 1.0 \times 20.0 \text{ mm}^3$) gewählt. Die Effekte dieser Kristallgeometrie wurden untersucht in Hinblick auf die Lichtsamm- lung und -verteilung für den Einzelkristall und als auch für das gesamte Detektormodul. Neben Systemdesignstudien für einen kompletten Detektorring basierend auf Monte-Carlo-Simulationen (MC-Simulation), wurde in Zusammenarbeit mit der Fakultät für Informatik der Technischen Universität München auch eine Methode zur analytischen Berechnung der Systemmatrix (SM) basierend auf dem Detector-response-function-model (DRF) entwickelt und implementiert. Die Validierung des DRF-Modells erfolgte durch Vergleich mit zwei anderen Systemmatrizen, die zum einen durch MC-Simulationen und zum anderen durch Messungen mit einer Punktquelle für jeden Voxel des zu rekonstruierenden Gesichtsfeldes erzeugt wurden. Der Vergleich der verschiedenen SM wurde mit dem Vorgängermodell MADPET durchgeführt, da MADPET-3 nur aus einem Detektor besteht, während MADPET-3 aus zwei Detektormodulen besteht, die eine Messung der kompletten SM für jeden Voxel mit einer Punktquelle nicht erlauben. Rekonstruktion wurde für verschiedene Phantome mit einem MLEM-Rekonstruktionsalgorithmus durchgeführt, der für die jeweilige SM entsprechend angepasst wurde.

Abstract

Positron Emission Tomography (PET) is a non-invasive, multidimensional imaging technique of physiological processes. It is widely used for medical diagnosis of cancer, heart or brain diseases. To obtain images that provide both, physiological information visualized by PET and anatomical information, the combination of PET with Computed Tomography (CT) has become a standard technology in clinical applications. In state-of-the-art PET/CT devices data acquisition is done sequential and image fusion of both modalities by software. Many efforts were undertaken to establish the combination of PET with Magnetic Resonance Imaging (MRI) in fully integrated system with simultaneous data acquisition of both modalities as MRI provides a better soft tissue contrast and no additional radiation dose. However, a combined PET/MRI scanner requires a more sophisticated detector concept that does not lead to interferences between the two modalities and also provides full functionality under the presence of strong magnetic fields.

Silicon photomultipliers (SiPM) are a promising new detector concept for combined PET/MRI scanners as they have a gain, a fast timing and are insensitive to magnetic fields. Based on this new type of detector a small animal PET prototype scanner, MADPET-3, has been developed. The MADPET-3 prototype consists of two detector modules each with an array of 8×4 monolithic SiPMs which are readout individually by Lutetium Yttrium Oxyorthosilicate (LYSO) scintillation crystals. To achieve a high sensitivity and spatial resolution a quiet extreme geometry ($1.0 \times 1.0 \times 20.0 \text{ mm}^3$) for the scintillation crystals has been chosen. The effects of this crystal geometry were investigated in terms of light collection and distribution for a single crystal and the whole detector module. Apart from system design studies for a complete detector ring which were realized by Monte Carlo (MC) simulations, also a method for an analytical calculation of the system matrix based on the detector response function model (DRF), has been developed and implemented in cooperation with the Department of Informatics of the Technische Universität München. A validation for the DRF model was accomplished by comparison with two other SMs that have been generated by MC simulation and based on point source measurements for each voxel of the field of view. The comparison of the different SMs was done with the predecessor model MADPET, as MADPET-3 consists only of two detector modules not allowing to measure the complete SM for each voxel with a point source. Reconstruction for various phantoms was performed with an ML-EM reconstruction algorithm adjusted for each SM.

Table of Contents

Zusammenfassung	i
Abstract	iii
Table of Contents	v
List of Figures	vii
List of Tables	ix
List of Abbreviations	xi
1 Introduction	1
2 Positron Emission Tomography	5
2.1 Positron Decay and Annihilation	5
2.2 Interactions of Photons with Matter	6
2.3 PET Detectors	7
2.3.1 Scintillators	8
2.3.2 Semiconductor Detectors	9
2.4 Detector Module Designs	12
2.4.1 Block Detector	12
2.4.2 Pixelated Detector	13
2.4.3 Continuous Detector	13
2.5 Coincidences	13
3 Image Reconstruction	17
3.1 Analytic Reconstruction	17
3.1.1 Data Acquisition	17
3.1.2 The Central Slice Theorem	18
3.1.3 Backprojection	19
3.1.4 Filtered Backprojection (FBP)	20
3.2 Iterative Reconstruction	20
4 Monte Carlo Simulations	27
4.1 DETECT2000	27
4.1.1 Surface Models in DETECT2000	28
4.2 GEANT4	33
4.3 GATE	33

5	Small Animal PET Imaging Systems	39
5.1	MADPET	39
5.2	MADPET-3	41
6	System Matrix	45
6.1	System Matrix based on the Analytical Detector Response Function Model	46
6.1.1	Theory	46
6.1.2	Implementation	48
6.2	Monte Carlo based System Matrix	52
6.3	Measurement of the System Matrix	53
7	Results	61
7.1	Simulation Studies for MADPET-3	61
7.1.1	Simulation of a Single Crystal Readout	61
7.1.2	Simulation Results for a Single SiPM Detector Module	72
7.1.3	Simulation of the MADPET-3 System	77
7.2	Measurements with MADPET-3	84
7.3	Results for MADPET	94
8	Summary and Outlook	103
	Appendix	107
A	Properties of LYSO	108
B	SiPM Detector Module	109
C	Description and Usage for the DRF-Code and the ML-EM Reconstruction on a Cluster Architecture	110
	Acknowledgments	113

List of Figures

1.1	FDG	2
1.2	Multi-modality Imaging	3
2.1	Detector ring	6
2.2	Silicon Lattice	10
2.3	p-n junction	11
2.4	SiPM	12
2.5	Block Detector	13
2.6	Detector Designs	14
2.7	Coincidences	15
3.1	Volume of Response	18
3.2	Single projection $p(s, \phi)$ and how it is organized in a sinogram	18
3.3	2D Central Slice Theorem	19
3.4	Single Element of the System Matrix	21
3.5	Flow Diagram of the ML-EM Algorithm	23
3.6	Convergence Properties of the ML-EM Algorithm	24
4.1	Coordinate System	29
4.2	Different surface models in DETECT2000	32
4.3	Adder Module	35
5.1	MADPET	39
5.2	APD Detector Array	40
5.3	SiPM Detector Array	41
5.4	LYSO Crystal Array	42
5.5	SiPM Detector Module	42
5.6	Photograph of MADPET-3	43
6.1	Reference Frame	47
6.2	DRF Model	47
6.3	Bounding Box	49
6.4	Slab Intersection Test	50
6.5	Angular Aperture in 2D	51
6.6	Angular Aperture in 3D	51
6.7	Evaluation Rays	52
6.8	Symmetries	53
6.9	Positioning Device	54
6.10	Alignment	55
6.11	Rotation	55

6.12	Voxel Grid	56
7.1	Position of interaction in one LYSO Crystal	62
7.2	Simulated Single LYSO crystal	63
7.3	Front Side and Back Side Readout	63
7.4	Number of Reflections	67
7.5	Light Collection	71
7.6	Crystal irradiated by radioactive source	72
7.7	Number of Events	73
7.8	Gamma Ray Absorption	74
7.9	Low Energy Threshold	75
7.10	Distribution of Detected Photons in one SiPM Module	76
7.11	MADPET-3 with 20 and 40 Detector Modules	77
7.12	Sensitivity Plots of MADPET-3 with 20 and 40 Detector Modules	79
7.13	Graphical Explanation of the SM	79
7.14	Lines Profiles of the Sensitivity Matrices	80
7.15	Reconstructed Uniform Phantom with an integral precision of 30	81
7.16	Lines Profile for MADPET-3 with 20 and 40 Detector Modules	81
7.17	Reconstructed Uniform Phantom with an integral precision of 60	82
7.18	MADPET-3 with 20 and 40 Detector Modules	82
7.19	Reconstructed Cylinder Phantom	83
7.20	Sensitivity Plots of MADPET-3	85
7.21	Dead Channels	85
7.22	Sensitivity and Weighting Factors for MADPET-3	86
7.23	Reconstructed Uniform Phantom for MADPET-3	87
7.24	Printed Phantom	88
7.25	Simulated Line Phantom	89
7.26	Printed Phantom	90
7.27	Printed Phantom	91
7.28	Cannula	92
7.29	Printed Phantom	93
7.30	Simulated Phantom	93
7.31	Phantom	94
7.32	Sensitivity Plots of the SMs for MADPET	95
7.33	Derenzo Phantom	95
7.34	Reconstructed Derenzo-like Phantom	96
7.35	Reconstructed Uniform Phantom	96
7.36	Line Profile Uniform Phantom	97
7.37	Sensitivity Plots of the SMs for MADPET	98
7.38	Reconstructed Derenzo-like Phantom	98
7.39	Reconstructed Uniform Phantom	99

List of Tables

1.1	Different Imaging Modalities	1
2.1	Commonly used PET radionuclides	5
2.2	Common used Scintillators	9
7.1	Contribution of Detector Layers	63
7.2	Light Collection of a Single LYSO crystal	65
7.3	Light Collection FSR vs. BSR	66
7.4	Light Collection	69
7.5	Light Collection for different Epoxy Layers	69
7.6	Light Distribution in one SiPM Detector Module	76
7.7	Characteristics of the two MADPET-3 Geometries	78
7.8	Reconstructed Uniform Phantom	83
7.9	Reconstructed Derenzo-like Phantom	84
7.10	Characteristics of the MADPET-3 Scanner	84
7.11	Reconstructed Uniform Phantom for MADPET-3	87
7.12	Requirements for the SMs	94
7.13	Reconstructed Derenzo-like Phantom	96
7.14	Reconstructed Uniform Phantom for MADPET	97
7.15	Reconstructed Derenzo-like Phantom	99
7.16	Reconstructed Uniform Phantom for MADPET	99
A.1	Properties of LYSO	108

List of Abbreviations

ADC	Analog to Digital Converter
APD	Avalanche Photodiode
ASIC	Application Specific Integrated Circuit
BGO	Bismuth Germanate
BP	Backprojection
BPF	Backprojection-filtering
BSR	Back Side Readout
CSR	Compressed Sparse Row
CT	Computed Tomography
DRF	Detector Response Function
DOI	Depth of Interaction
FBP	Filtered Back Projection
FDG	Fluoro-deoxy glucose
FOV	Field of View
FSR	Front Side Readout
FWHM	Full Width at Half Maximum
F9S-3-M	Precision Positioning System (UHL)
GATE	GEANT4 Application of Tomographic Emission
GEANT4	Geometry and Tracking
LET	Low Energy Threshold
LRZ	Leibnitz-Rechenzentrum
LSO	Lutetium Oxyorthosilicate
LOR	Line of Response
LY	Light Yield
LYSO	Lutetium-Yttrium Oxyorthosilicate
MADPET	Munich Avalanche Photodiode Positron Emission Tomograph
MC	Monte Carlo
MLEM	Maximum Likelihood Expectation Maximization
MPI	Message Passing Interface
MPPC	Multi-Photon Pixel Counter
MRI	Magnetic Resonance Imaging
NEMA	National Electrical Manufacturers Association
NSLEV	Nanosekunden-Ladungsempfindlicher-Vorverstärker
OSEM	Ordered Subset Expectation Maximization

PDE	Photon Detection Efficiency
PEM	Positron Emission Mammography
PET	Positron Emission Tomography
PMT	Photomultiplier Tube
PSF	Point Spread Function
PTFE	Polytetrafluoroethylene, also known by the DuPont brand name Teflon
QE	Quantum Efficiency
R	Reflectivity
SADC	Sampling Analog to Digital Converter
SM	System Matrix
SiPM	Silicon Photomultiplier Tube
SPECT	Single Photon Emission Tomography
TOF	Time of Flight
TOR	Tube of Responce

Chapter 1

Introduction

A variety of medical imaging modalities is used for the diagnosis and therapy monitoring of human diseases. Radiological imaging methods such as Computed Tomography (CT) and Magnetic Resonance Imaging (MRI) are able to provide anatomic information with high resolution. Although there are contrast agents and dedicated pulse sequences which offer measurement of biological parameters, the sensitivity of MRI is much lower than PET. In contrast to that, nuclear medicine imaging techniques, such as Single Photon Emission Tomography (SPECT) and Positron Emission Tomography (PET), allow functional imaging at the level of cells and proteins. Therefore a large number of biological processes and the various diseases related to them can be monitored with a high sensitivity. A comparison between nuclear medicine imaging modalities with CT and MRI in terms of spatial resolution and sensitivity is given in table 1.1.

Table 1.1: A comparison of spatial resolution and sensitivity of imaging modalities (PET and SPECT) in nuclear medicine to CT and MRI [1], [2].

	CT	MRI	PET/SPECT clinical	PET preclinical
Sensitivity (ng/ml)	1000000	1000	5-15	1-15
Resolution (mm)	< 1	< 1	5-15	1-2

Due to the different information provided by nuclear medicine imaging techniques compared to radiological imaging modalities and the low spatial resolution offered by nuclear medicine modalities, combinations of multiple modalities are nowadays used in one device. Combined PET/CT scanners with serial acquisition are already well established in clinical routine. Typically a very fast CT acquisition of a few seconds is followed by a PET data acquisition of several minutes. As the two data sets are acquired sequentially the images are fused afterwards by software. Recently, increasing effort was put to combine PET with MRI to acquired data simultaneously of both modalities. Joining these two techniques involves many problems because of the high static magnetic field and the fast changing gradient fields in the MRI scanner. The presence of PET hardware components adds additional inhomogeneities to the static magnetic field which may lead to artefacts in the MR image. All the PET hardware components have to work properly inside the high static magnetic and the gradient fields. Photomultiplier tubes, which are commonly used as PET detectors can not be operated in such an environment. Therefore novel detector concepts were proposed to overcome this problems: Avalanche Photodiodes

(APDs) are semiconductor detectors with a low-field depleted region where electron-hole pairs are created by visible light. The electrons or the holes are collected and multiplied in an electrical field region by impact ionization (avalanche multiplication). APDs are used in different experimental small animal PET systems, like the Munich Avalanche Diode Positron Emission Tomograph (MADPET) [3]. PET systems based on APDs were successfully tested in combination with high field MRI systems [4]. APDs are implemented in the first commercial PET/MR whole body system with simultaneous PET and MRI imaging [5]. Recently a new type of semiconductor detectors, the Silicon Photomultipliers (SiPMs), were developed for their use in PET imaging [6]. SiPMs consist of a densely packed matrix of APDs operating in Geiger mode, archiving a higher gains as APDs and similar to PMTs. As APDs they are also insensitive to magnetic fields which makes them to be good candidates for a combined PET/MRI system with simultaneous data acquisition. The combination of PET with MRI offers certain advantages over combined PET/CT scanners. Sequential PET/CT imaging suffers potential misalignment of the two data sets. Movement of the patient e.g. like the heart beat or breathing during the data acquisition time is one of the most limiting problems in PET/CT. The movement leads to smearing artefacts as the reconstructed PET image is an average acquisition over several minutes. Another advantage of MRI compared to CT is that the MRI scan does not involve additional radiation exposure for the patient and offers a higher soft tissue contrast. Figure 1.2 shows exemplary images of a patient with a mamma carcinoma for different images modalities. Data for these images was recorded during an initial study for a dedicated PET scanner for mammography as a part of the project EU FP6 MAMMI [7]. For a PET scan the patient gets an injection of a biological active molecule labelled with a radioisotope. The most commonly used one for this purpose is fluorodeoxyglucose (^{18}F -FDG) [8]. ^{18}F -FDG is a glucose analogue in which one hydroxyl group is exchanged by ^{18}F (see figure 1.1). ^{18}F -FDG metabolises as normal glucose but after phosphorylation, ^{18}F -FDG remains caught inside human cells due to the slight difference in their chemical structure. Thus, leading to an accumulation of ^{18}F -FDG in all cells with a high glucose metabolism. As many malignant diseases such as cancer possess a high glucose metabolism, ^{18}F -FDG-PET has become the most common one to explore cancer cells and metastasis.

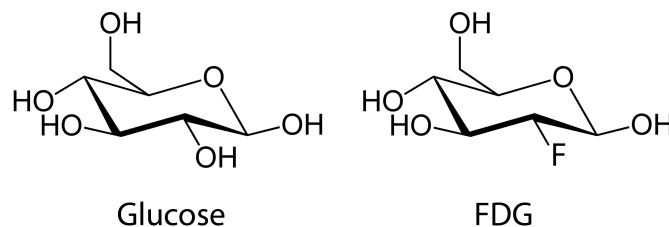


Figure 1.1: Chemical structure of glucose (left) and ^{18}F -FDG (right). One OH^- group is replaced by ^{18}F [9].

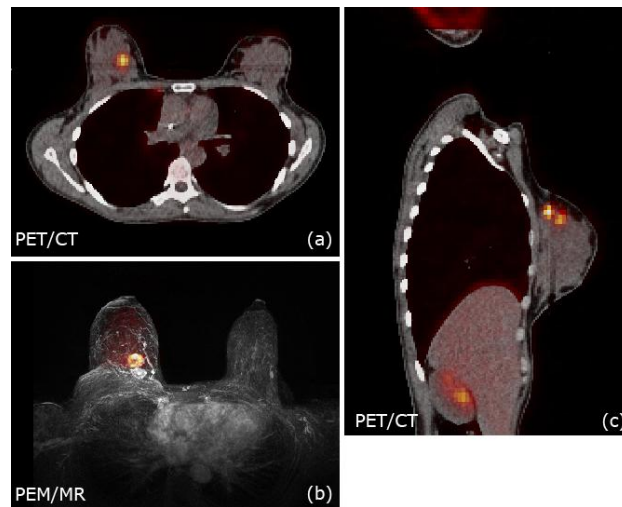


Figure 1.2: Patient with mammary carcinoma: Fused PET/CT images of the transverse (a) and sagittal plane (c). The same patient was scanned after the PET/CT examination with a dedicated breast PET scanner and the reconstructed PET image was fused with data acquired with an MRI scanner (b). Alignment between the data sets was performed through software as for the fused PET/CT images. Data for these images was recorded during an initial study for mammography as a part of the project EU FP6 MAMMI [7].

Overview of This Work

This work is dedicated to two small animal PET systems the MADPET and the MADPET-3 prototype scanners.

The MADPET-3 prototype scanner has been developed as part of this work at the Nuclear Medicine Department at the Klinikum rechts der Isar of the Technische Universität München. The main focus of this work was to develop a reconstruction software for MADPET-3. For this purpose a method for an analytical calculation of the system matrix (SM) based on the detector response function model (DRF), has been developed and implemented in cooperation with the Department of Informatics of the Technische Universität München.

MADPET is a small animal PET scanner built in 1996 at the Nuclear Medicine Department at the Klinikum rechts der Isar of the Technische Universität München and the Max Planck Institute for Physics. MADPET was used to test and validated the DRF model and also to compare the calculated SM with two other SMs based on Monte Carlo simulations and on point source measurements.

References

- [1] R.A. BUNDSCHUH, *Improving Quantification in Combined Positron Emission and Computed Tomography in Oncology*, PhD Thesis in Physics, Technische Universität München, Munich, Germany, 2011
- [2] G.H. HUTCHINS, M.A. MILLER, V.C. SOON, T. RECEVEUR, *Small Animal PET Imaging*, ILAR J. vol. 49(1), pp. 54-65, 2008
- [3] S.I. ZIEGLER, B.J. PICHLER, G. BOENING, M. RAFECAS, W. PIMPEL, E. LORENZ, N. SCHMITZ, AND M. SCHWAIGER, *A Prototype High-resolution Animal Positron Tomograph with Avalanche Photodiode Arrays and LSO-Crystals*, Eur. J. Nucl. Med. Mol. Img., 28(2), pp. 136-143, 2001
- [4] C. CATANA, Y. WU, M.S. JUDENHOFER, J. QI, B.J. PICHLER, AND S. CHERRY, *Simultaneous Acquisition of Multislice PET and MR Images: Initial Results with a MR-Compatible PET Scanner*, Eur. J. Nucl. Med., 47(12), pp. 1968-1976, 2006
- [5] SIEMENS, Biograph mMR, http://www.medical.siemens.com/siemens/en_INT/gg_mr_FBAs/files/multimedia/Biograph_mMR/PET_MR_Applied_Radiology_Supplement.pdf
- [6] V.C. SPANOUDAKI, A.B. MANN, A.N. OTTE, I. KONOROV, I. TORRES-ESPALLARDO, S. PAUL, AND S.I. ZIEGLER, *Use of Single Photon Counting Detector Arrays in Combined PET/MR: Characterization of LYSO-SiPM Detector Modules and Comparison with a LSO-APD Detector*, J. Instr., 2(12), pp. 0-16, 2007
- [7] MAMMI: Mammography with molecular imaging scanner (Oncovision, GEM Imaging S.A., Valencia, Spain), EU funded project: EU FP6 MAMMI
- [8] A. BUERKLE AND W.A. WEBER, *Imaging of Tumor Glucose Utilization with Positron Emission Tomography*, Cancer Metastasis Rev, 27(4), pp. 545-554, 2008
- [9] ACADEMIC, Academic dictionaries and encyclopedias, <http://de.academic.ru/dic.nsf/dewiki/529189>

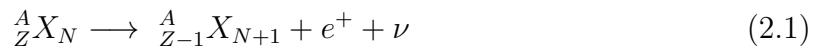
Chapter 2

Positron Emission Tomography

PET is considered to be the most sensitive modality for performing quantitative in vivo imaging in modern medicine. The following paragraphs summarize the special features of PET imaging and describe how these features affect the image quality.

2.1 Positron Decay and Annihilation

PET imaging relies on the nature of the positron and positron decay. The positron is the antimatter counterpart to the electron. When a nucleus undergoes positron decay, the result is a new nuclide with one less proton and one more neutron, as well as the emission of a positron and a neutrino:



The radionuclides that decay via positron emission are proton-rich and move closer to the line of stability while giving off a positive charge. The neutrino is very light and interacts only very weakly with other particles. It is therefore not directly relevant to nuclear medicine. However, its presence in the positron decay makes the energy of the positron variable. The most commonly used PET radionuclides are shown in table 2.1. One characteristic is a short half-life. These radionuclides, which are cyclotron-produced, are also small atoms and can be bound in biochemically relevant molecules [1].

Table 2.1: Commonly used PET radionuclides together with their half-life, their maximum positron energy and their average positron range in water prior to annihilation [1].

Nuclide	Half-life[min]	E_{max} [MeV]	Mean positron range [mm]
${}^{11}\text{C}$	20.3	0.96	1.1
${}^{13}\text{N}$	9.97	1.12	1.5
${}^{15}\text{O}$	2.0	1.74	2.5
${}^{18}\text{F}$	110	0.62	0.6

As positrons pass through matter, they will undergo interactions including loss of kinetic energy through ionization and excitation of nearby atoms and molecules. After losing enough energy, and having travelled a certain distance in the neighbourhood depending on the initial energy, the positron will annihilate with a nearby electron by converting their rest masses into energy. Due to momentum conservation the energy has

to be released in more than one photon. The number of emitted photons during the annihilation is depending on the relative orientations of the spins of the electron and the positron at the moment of annihilation. If both spins are anti-parallel resulting in a singlet spin state of total spin $S = 0$ conservation of energy, momentum and parity requires radiation in form of two gamma rays with an energy of 511 keV each, emitted in opposed directions. In the case of parallel spins of electron and positron yielding to a symmetric triplet spin state of total spin $S = 1$ three photons are created and the available energy is shared between them. Since the creation of three photons is of higher order with a cross section $\sigma_{3\gamma}$ proportional to the electromagnetic coupling constant $\alpha = \frac{e^2}{\hbar c} \approx \frac{1}{137}$, the annihilation in three photons occurs very seldom. Considering all spin states, the ratio for the cross sections for the annihilation in three and two photons accounts to:

$$\frac{\sigma_{3\gamma}}{\sigma_{2\gamma}} = \frac{3}{8}\alpha = \frac{1}{372} \approx 0.003 \quad (2.2)$$

In about 60 of all annihilation events, the electron and positron are not completely at rest and have still small velocity resulting in a deviation for the emission angle of $\pm 0.5^\circ$ [2]. This may lead to inaccuracy in the definition of the corresponding LOR in large scanners and small detector elements, but generally not for small animal PET scanners with a rather small FOV. If two annihilation photons are measured in two detectors placed around the patient, the origin of the annihilation is allocated in the space between the two detectors. This space is named line of response (LOR), which actually represents a volume of response defined by the span of the two detectors. In order to measure coincidence photons, the detector must be placed around the patient at opposing positions usually arrange by ring of detectors as shown in figure 2.1.

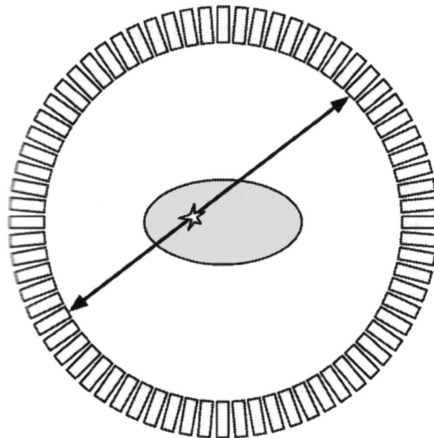


Figure 2.1: Schematic drawing of a PET detector ring arranged around a patient in the transverse plane and one annihilation event and the corresponding line of response [3].

2.2 Interactions of Photons with Matter

After annihilation, the generated photons travel in the surrounding material and interact with charged particles due to their inherent character of being an electromagnetic wave.

The type of interaction with matter depends on the energy of the photons as well as on the atomic number and density of the surrounding material. Pair production, where an electron-positron pair is created from an high energetic photon, can be neglected for photon energy levels occurring in PET, as for this case an energy of at least 1022 keV for the interacting photon is necessary. Rayleigh scattering, where the photon is completely absorbed by an atom and subsequently re-emitted with an altered direction but no loss in energy, is only relevant for photons with an energy below 50 keV [3]. Only optical photons created inside an scintillation crystal, may be affected by Rayleigh scattering. The dominating interactions for 511 keV photons are photoelectric effect and Compton scattering. If photoelectric absorption occurs, the incoming photon transfers its energy completely to an orbital electron of an atom. The kinetic energy of the electron is then sufficient to be ejected from its shell, which equals the difference between the incident photons energy E_γ and the binding energy E_b corresponding to the shell from where it was emitted from:

$$E = E_\gamma - E_b \quad (2.3)$$

The empty place in the shell is refilled by other electron from the proximity generating characteristic X-rays or Auger electrons. The probability for photoelectric interactions is roughly proportional to $1/E_\gamma^{-7/2}$ and Z^5 , where Z is atomic number of the absorbing material [4]. Compton scattering can be described by a photon being scattered at an certain angle θ by an electron of an outer atomic orbital, where the binding energy of the electron is very small such that the electron may be considered as almost "free" in this context. The photon only transfers a part of its initial energy to the electron and it is not absorbed but changes its direction. Due to energy and momentum conservation, the energy of the scattered photon can be determined by:

$$E = \frac{E_0}{1 + \frac{E_0}{m_e c^2} (1 - \cos\theta)} < E_\gamma \quad (2.4)$$

where E is the energy of the scattered photon, E_0 the energy of the incoming photon, θ the angle of scattering, m_e the electron mass and c the speed of light. For 511 keV photons this equation simplifies to:

$$E[\text{keV}] = \frac{511}{2 - \cos\theta} \quad (2.5)$$

The recoil energy $E_{rc} = E_0 - E$, which is transferred to the electron, dissipates inside the medium. The maximum energy loss occurs for the case of backscattering at an angle of 180° resulting in an maximum recoil energy of $E_{rc} = 341$ keV and an energy of $E = 170$ keV. This is important for PET applications as detectors may be able to discriminate the energy of the detected photon. The proportionality for Compton scattering is roughly proportional to $\frac{1}{E_\gamma}$ and Z [4], [5].

2.3 PET Detectors

The most common detector concept in nuclear medicine is based on scintillation crystals coupled to light sensors. A dense scintillation crystal is used to convert the energy de-

posited by the 511 keV photons into visible light that can be detected by a light sensors such as photomultiplier tubes (PMTs) or solid state detectors like avalanche photodiodes (APDs) or silicon photomultipliers (SiPMs).

2.3.1 Scintillators

Light creation in scintillators, also referred as luminescence, can be described by the energy band structure in a crystalline scintillator. An incident gamma ray generates electron-hole pairs by lifting electrons from the valence band to the lowest unoccupied band. The generated electron-hole pairs recombine by emitting photons in the non-visible X-ray range. In order to obtain photons in the visible range, impurities or activator levels are introduced in the crystal energy band structure. The created electron-hole pairs ionize these foreign atoms as their ionization energy is usually smaller than the one of typical lattice site. By de-excitation to the activator ground state, photons are emitted in the visible range at a wavelength corresponding the activator level in the band structure [7]. Half-lives of such excited states are in the range of 50 to 500 ns. Besides fluorescence, also phosphorescence may occur as process in a scintillator. If an electron arrives at an luminescence centre creating an excited state whose transition to the ground state is quantum-mechanically forbidden, an additional increment of energy due to e.g. thermal excitation is necessary to lift the activator to a higher state from where it can de-excite. The process contributes to a slow component of the light yield denoted as afterglow. The ideal scintillator for PET should offer the following conditions:

- ◇ A high efficiency for the interaction of high energetic gamma rays via photoelectric effect or Compton scattering visible. Therefore, scintillation materials with a atomic number Z and high density are preferred.
- ◇ A high light yield is important as the number of generated optical photons define the energy resolution of the detector.
- ◇ The amount of created light has to be proportional to the deposited energy by the incident gamma rays. This is necessary to distinguish between different energies of incident particles or photons and allows to suppress scattered photons with a low energy.
- ◇ The decay time of the scintillator of the luminescence should be as short as possible to create fast signal pulses from the detector.
- ◇ The scintillator should be transparent for the emitted wavelength of the luminescence to provide good light collection.
- ◇ For a good light transmission to the light sensor, the index of refraction should be near to the one of the entrance window of the light sensor.
- ◇ The scintillator should be easy to handle in terms of robustness and hygroscopy.

Unfortunately, the perfect scintillator does not exist, therefore the choice of the adequate material is always a compromise depending on the requirements and the application. Table 2.2 provides an overview of the most frequently used scintillators and their properties.

Table 2.2: Properties of some commonly used scintillators. The crystal materials are doped with the material given in brackets. Data were taken from [6], [7], [8], [9] and [10].

	BGO	LSO(Ce)	LaBr(Ce)	GSO(Ce)	NaI(Tl)
Density (g/cm^3)	7.13	7.40	5.30	6.71	4.67
Effective atomic number Z	76	65	47	59	51
Light yield (photons/511 keV)	8200	30000	60000	10000	37700
Decay time (ns)	300	40	25	60	230
Wavelength (nm)	505	420	370	430	415
Refractive index	2.15	1.82	1.88	1.85	1.85
Attenuation length (mm)	11	12	22	14	29
Hygrosocopy	no	no	yes	no	yes

2.3.2 Semiconductor Detectors

Over a long period of time, photomultiplier tubes were the gold standard used as read-out detector for a scintillation crystal. As semiconductor detectors with new promising properties in terms of an adequate sensitivity for a reasonable price became available, they started to replace the PMTs and allowed new detector designs due to their compact size. Furthermore, they are insensitive to magnetic fields which makes them potential candidates for combined PET/MR systems.

The Basic Principle of Semiconductor Detectors

The working principle for semiconductor detectors relies on their electric band structure. In lattice structure, the atomic orbitals overlap and thus recombine quantum-mechanically. The number of possible discrete energy states increases and the levels move closer together until they fuse which allows to describes them as energy bands. The conduction properties of the solid state are defined by how the energy levels are occupied in the two highest bands, the valence and the conduction band. Usually they are separated by a band gap E_g which represents a quantum-mechanically forbidden region. In semiconductors this band gap is in the range of 1 eV and 5 eV, which is narrow enough, that electrons can be lifted up from the valence to the conduction band by thermal excitation or radiation. The generated electron-hole pairs created by this process are spatially mobile and contribute to the conductivity. As semiconductor material in nuclear medicine silicon (Si) may be used. In pure Si, each atom is bound covalently by four binding electrons from the neighbouring Si atoms in the crystal. Adding certain impurities to the crystal lattice increases the intrinsic conductivity. If elements from the third group (e.g. Boron, 3 binding electrons) of the table of elements are added to the Si lattice, there is one electron less available for the covalent binding. As this creates positive charge, a hole in the crystal lattice such regions are defined as p-doped. Replacing a Si atom by an element from the fifth group (e.g. Phosphorus, five binding electrons) of the table of elements, an additional unbound electron is created in the crystal lattice. That kind of implanted impurity is called n-doped. All cases of d- and n-doped crystal lattices as well as a pure Si lattice are shown in figure 2.2.

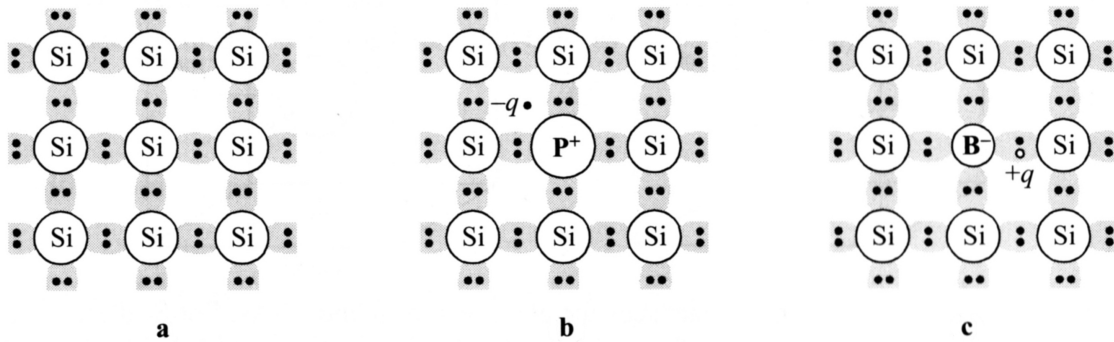


Figure 2.2: Illustration of three lattice schemes: (a) Pure silicon as an intrinsic semiconductor, (b) Si lattice doped with Phosphorus, (c) Si lattice doped with Boron [7].

Silicon Photodiodes

A silicon photodiode consists of two thin layers of a p- and n-doped silicon with electrodes on both layers (figure 2.3). Due to the different concentrations of electrons and holes in the different layers, electrons diffuse from the n- to the p-doped area and holes migrate from the p- to n-doped region. This results in an electric field in the border region which is positive on the n side (less electrons than before) and negative on the p side (less holes and more electrons than before). The region at the border between the two layers contains then no more free charge carriers due to the recombination of electrons and holes and is therefore called depletion zone. The process is at an equilibrium when the forces caused by the diffusion gradient and the electric field compensate each other. If an incident photon reaches the depletion region, it can generate electron-holes pairs by photoelectric effect. The electric field separates the pair by accelerating the hole to the p-region and the electron the n-region. Thus, if the n- and the p-region are inductively connected, a current can be measured. The width of the depletion region can be modified by applying a voltage across the diode. If the diode is operated in forward bias mode with the p material connected to the positive electrode and the n material to the negative electrode, the width of the depletion region will decrease as the holes as well as the electrodes are forced towards the junction and recombine there. Applying a reverse bias voltage to the p-n junction in the same direction as the intrinsic electric field, the depletion region is broaden as the holes in the p layer are pushed away from the junction as well as the electrons in the n layer.

Avalanche Photodiodes

Standard photodiodes have no internal gain as they just generate one electron-hole pair per interaction. The problem of missing amplification may overcome by applying a higher reverse bias voltage across the diode. If the reverse bias voltage is sufficiently high, it accelerates the electron-hole pairs such that on their way towards the anode and cathode, they ionize other lattice atoms. The process is multiplied over and over leading to an avalanche of carries. In such a case, an incoming photon causes the diode to break down. The break down is a reversible and non-destructive process, as long as the generated current does not reach levels that would overheat the semiconductor. For a certain applied voltage the strength of the current generated in the APD is proportional to number of incident photons which defines the operation mode of the APD also addressed as Geiger mode. Avalanche photodiodes usually have a typical gain of 10^2 to 10^3 and a quantum efficiency of 80% [5]. To compensate the lower gain compared to PMTs, scintillation crystals with a high yield are needed to achieve a higher signal output or they are used in combination with an charge sensitive preamplifier. APDs offer a similar performance in terms of energy and time resolution as with PMT detectors, but due to their compact size their allow to assemble more complex detector designs and can be operated in high magnetic fields [11].

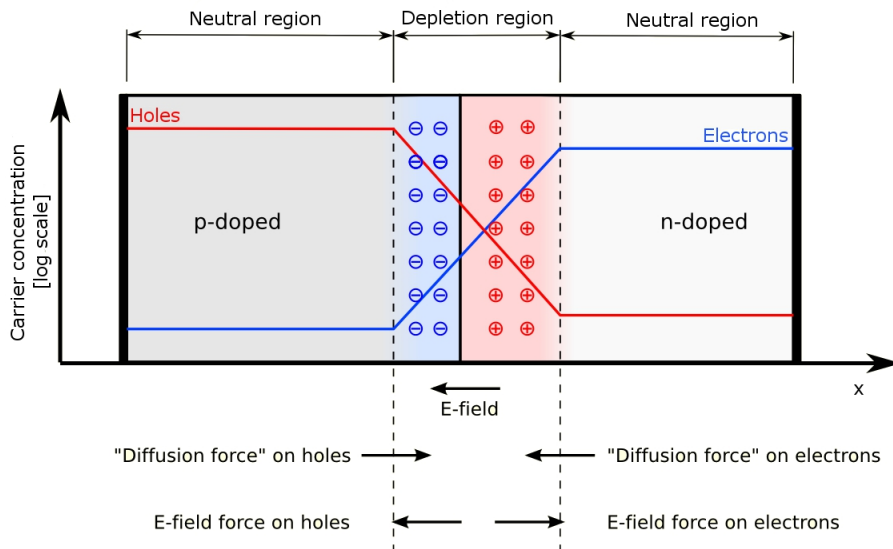


Figure 2.3: Schematic drawing of a p-n junction [12].

Silicon Photomultipliers

The so called silicon photomultipliers (SiPMs) are good candidates to overcome the drawbacks of semiconductor devices and PMTs. A SiPM basically contains an array of 400 to 4000 APDs operated in limited Geiger mode, on a common silicon substrate. The size of a single APD or as they often denoted as cells, ranges between 20 and 100 μm , the whole SiPM has the dimension of 1 to 3 mm^2 . A SiPM is based on a multilayer structure with different doping levels, comprising a thin depletion region with very high electric field of about $5 \times 10^3 \text{V/cm}$ which is necessary to operate the cell in Geiger mode. The generated avalanche of charge carriers form always a current of maximum strength independent of the number of photons that were impinging on the readout surface of the SiPM [13]. Therefore, a SiPM provides only binary information cell fired or cell not fired without any proportionality to the amount of incident photons. The Geiger breakdown current is limited by the charge accumulation in the cell through a capacitor and a quenching resistor in each cell [14]. Although the cells are separated from each other, but based on a common readout line the signal of one SiPM equals the sum of all individual cells. As the number of cells within one SiPM is limited, also the dynamic range is limited by that number. If more than one photon hits one cell in the SiPM at the same time or during the cell recovery time, the additional photons are not counted and thus leading to non-linearity and saturation effects.

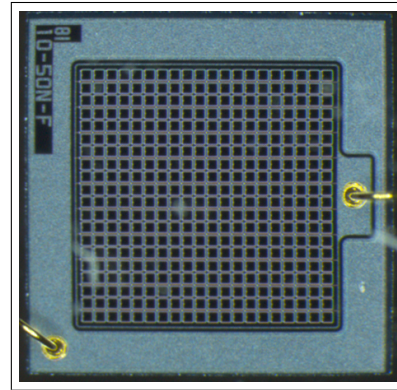


Figure 2.4: Photograph of a SiPM detector with 400 individual Geiger mode APDs. The active area measures 1 mm^2 .

2.4 Detector Module Designs

2.4.1 Block Detector

Conventionally PET detector module designs used in clinical routine are based on PMTs as detectors. To minimize the cost and due to space constraints, the total number of PMTs is always kept as low as possible. In order to avoid loss of sensitivity a block detector design is used. Figure 2.5 shows a photograph of a typical block detector, consisting of four PMTs coupled to one common scintillator block. The scintillator block is segmented into an array of smaller scintillation elements, e.g. 8×8 resulting in 64 channels per detector modules. The gaps between the crystal segments are filled with white high reflecting material such as barium sulphate to isolate the segments among each other and provide proper light collection in each segment. The crystal pattern leads to a specific light distribution between the four PMTs. The centroid of the four PMT signals identifies the scintillator segment where the gamma rays interaction occurred. This detector concept allows to build PET scanners with thousands of crystals, which equals the number of channels, at a reasonable cost. The main disadvantages of this approach are a limited counting rate and a possible false reconstructed position information [5].

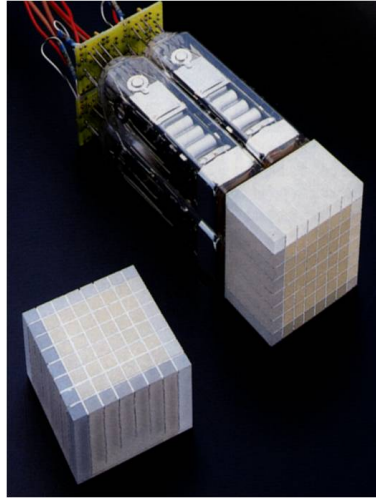


Figure 2.5: Block detector consisting of four PMTs coupled to an array of 8×8 crystal segments.

2.4.2 Pixelated Detector

With the new developed semiconductor devices such as APDs and SiPMs, new detector concepts can be considered. Their relatively small sizes allow a direct one-to-one coupling between the scintillation crystal and the detector. The main advantages of such a design is that the spatial resolution is merely defined by the size of the crystal and the corresponding photo detector can easily identify the crystal where the interaction between the gamma ray and the detector occurred. But this requires on the other side that the crystals have to be well separated and any light crosstalk between the crystals on the SiPM detector has to be avoided. On the other hand individual crystal readout increases the insensitive area in the detector module as the crystal needs to be separated by air gaps and a reflector material put in between.

2.4.3 Continuous Detector

Another approach, which is also quite cost-effective, is the usage of thick continuous crystal blocks read out by several light sensors. By using position-sensitive PMTs the localization of the deposited energy is possible and may also provide information about the depth inside the crystal where the annihilation event was detected. The main advantage over pixelated detectors designs is the increased sensitivity as the dead space is reduced by the crystals [5]. Figure 2.6 provides an overview of the discussed detector modules designs.

2.5 Coincidences

The main task for PET reconstruction is to identify the distribution of the radio tracer inside the FOV. This allows to characterize the biological processes that are directly correlated to the tracer distribution. Each detected photons is defined by its detection time and deposited energy in the detectors. Both informations are used to specify the LOR and therefore the pair of detectors in which the annihilation event was detected within

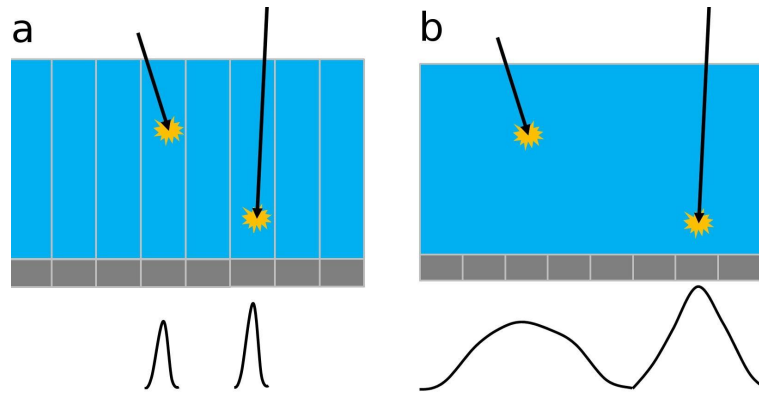


Figure 2.6: (a) Schematic drawing of pixelated detector module design. Two different events can be clearly separated by their corresponding detectors. (b) Schematic drawing of continuous detector module design. The width of the light distribution depends on the distance of the interaction from the photosensor [15].

a certain time coincidence windows. The minimal width of the coincidence time window is defined by the time difference of the photons to travel from the annihilation point to the detector and by the time resolution of the detector. If the two photons are emitted at an exact angle of 180° then the annihilation must have taken place in the volume covered by the two detectors which is usually addressed as LOR. Whereas, the detection of the two annihilating photon are called coincidence events. In a real experiment not all coincidences are emitted at an angle of 180° and several other scenarios as indicated in figure 2.7 are possible.

- ◇ True coincidences: Two photons are emitted in an angle of 180° . On their flight trajectory they are not scattered by the media they travel through. For those events the correct LOR can be addressed.
- ◇ True coincidences, but leading to the wrong LOR due to non-linearity or due to scattering: Two photons are generated but one is scattered into a different direction.
- ◇ Random coincidences: Two photon originate from different annihilations events but are detected by one detector pair.

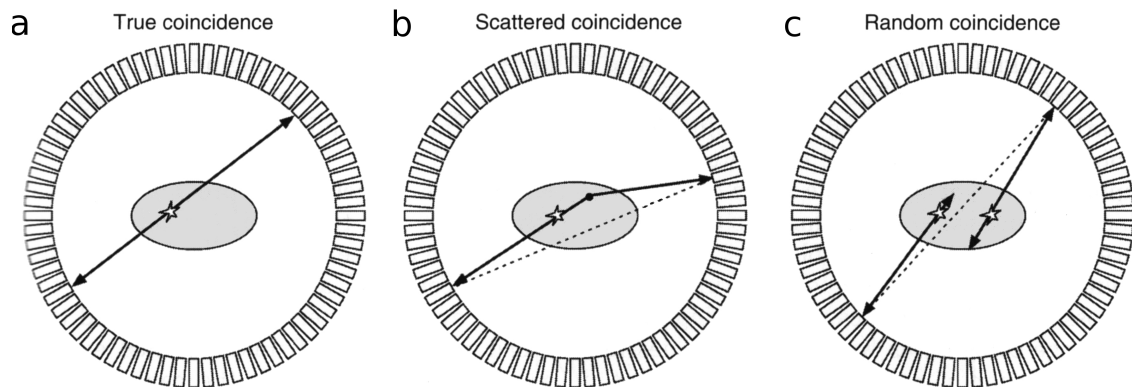


Figure 2.7: Different types of coincidences that may occur during a measurement. (a) True coincidence: Two photons are emitted an angle of 180° . (b) Scattered coincidence: Two photons are generated but one is scattered into a different direction. (c) Random coincidence: Two photons originate from different annihilation events are detected by one detector pair within the coincidence time window [3].

References

- [1] P.E. VALK, D.L. BAILEY, D.W. TOWNSEND, AND M.N. MAISEY, eds., *Positron Emission Tomography: basic science and practical practice*, Springer-Verlag, 2003
- [2] UNIVERSITÄT KARSRUHE, Fortgeschrittenen Praktikum, *Lebensdauer des Positrons*, <http://www.physik.uni-karlsruhe.de/Studium/F-PRAKTIKA/Downloads/Positronium-07.pdf>
- [3] S.R. CHERRY, J.A. SORENSEN, AND M.E. PEHLPS, *Physics in Nuclear Medicine*, 3rd Edition, Saunders, 2003
- [4] DEMTRÖDER, *Experimentalphysik 4, Kern- Teilchen- und Astrophysik*, Springer, 1998
- [5] M.E. PHELPS, *PET - Physics, Instrumentation and Scanners*, Springer, 2006
- [6] M.N. WERNICK, AND J.N. AARSVOLD, *Emission Tomography. The Fundamentals of PET and SPECT*, Elsevier Academic Press, 2004
- [7] G.F. KNOLL, *Radiation Detection and Measurement*, 2nd Edition, Wiley, 2000
- [8] W.W. MOSES, AND K.S. SHAH, *Potential for RbGd₂Br₇:Ce, LaBr₃:Ce, LuI₃:Ce in nuclear medical imaging*, Nucl. Instr. Meth. Phys. Res. A 537, pp. 317-320, 2005
- [9] A.R. KARIMIAN, AND C.J. THOMSON, *Assessment of a new scintillation crystal (LaBr₃) in PET scanners using Monte Carlo methods*, NUKLEONIKA 53, pp. 3-6, 2008
- [10] B. PICHLER, G. BÖNING, M. RAFECAS, M. SCHLOSSHAUER, E. LORENZ, AND S.I. ZIEGLER, *LGSO scintillation crystals coupled to new large area APDs compared to LSO and BGO*, IEEE Trans. Nucl. Sci. 46, pp. 289-291, 1999
- [11] B. J. PICHLER, *Untersuchung der Detektoreigenschaften von Lutetium-Oxyorthosilikat-Szintillationskristallen und Lawinen-Photodioden für die hochauflösende Positronen-Emissions-Tomographie*, Diploma Thesis in Electrical Engineering and Communication, Technische Universität München, Munich, Germany, 1996
- [12] WIKIMEDIA COMMONS, <http://commons.wikimedia.org>
- [13] V. KOVALTCHOUK, G. LOLOS, Z. PAPANDREOU, AND K. WOLBAUM, *Comparison of silicon photomultiplier to a traditional vacuum photomultiplier*, Nucl. Instr. Meth. Phys. Res. A 538, pp. 408-415, 2005
- [14] B. DOLGOSHEIN ET. AL., *Status report on silicon photomultiplier development and its applications*, Nucl. Instr. Meth. Phys. Res. A 563, pp. 368-376, 2006
- [15] A. VELROYEN, *Development of a Novel Detector Module for PET/MR Imaging Based on SiPMs and Fast Scintillation Crystals*, Diploma Thesis in Physics, Fakultät für Physik, Ludwig-Maximilians-Universität München, Munich, Germany, 2010

Chapter 3

Image Reconstruction

THE purpose of tomographic image reconstruction is to provide a cross-sectional image of the distribution of radiotracer activity from the acquired data by the scanner.

The different methods for tomographic reconstruction can be divided into analytic and iterative approaches. Analytic reconstruction methods offer a fast and direct mathematical solution for the image with no attempt to model the statistical nature of the gamma-ray counting process. Statistical, iterative methods are based on a more accurate description of the imaging process resulting in a more complicated mathematical solution requiring multiple steps to get the final image. This chapter will give a brief overview of these two reconstruction methods and offers an introduction of the trade-offs between the methods [1], [2].

3.1 Analytic Reconstruction

3.1.1 Data Acquisition

PET imaging can be described with a line-integral model of the acquisition. The parallelepiped joining two detectors defines the volume of response (VOR) (figure 3.1). Disregarding physical effects such as attenuation, scattered and random coincidences or detector efficiency variations, the total number of detected coincidence events will be proportional to the total amount of tracer activity contained in the VOR, as indicated in the shaded area in figure 3.1 (b).

In the following sections the reconstruction process will be described for the two-dimensional case. Two-dimensional imaging only considers lines of response (LORs) lying within a specified plane. The acquired data are collected along LORs through a two-dimension object $f(x,y)$, as illustrated in figure 3.2. All LORs are organized into sets of projections $p(s, \phi)$ for all distances s between the projection and the coordinate origin for a fixed angle ϕ . The collection of all projections for $0 \leq \phi \leq 2\pi$ forms a two-dimensional function of s and ϕ . This function is called sinogram as a fixed point in the object traces a sinusoidal path in the projection space as shown in figure 3.2. A sinogram for a general object will be the superposition of all sinusoids corresponding to each point of activity in the scanned object. The line-integral transform of $f(x, y) \rightarrow p(s, \phi)$ is equivalent to the Radon transform [3],[4]:

$$\mathcal{T}_R[f(x, y)] = p(s, \phi) = \int_L f(x, y) dl \quad (3.1)$$

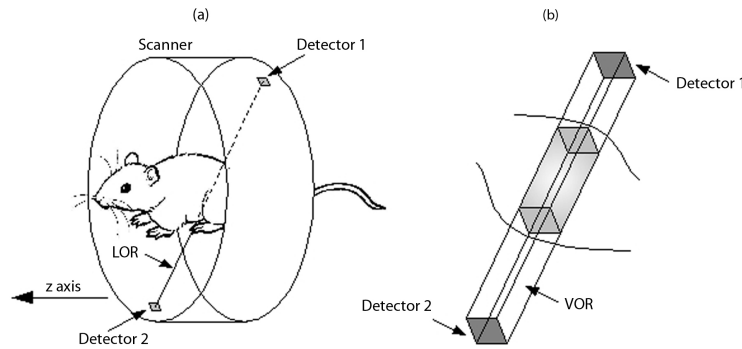


Figure 3.1: Volume of response corresponding to the sensitive region scanned by two detector elements. (a) Overall scheme with the volume indicated as a line of response (LOR). (b) Detail showing the volume of response (VOR) scanned by two detector elements (not to scale) [1].

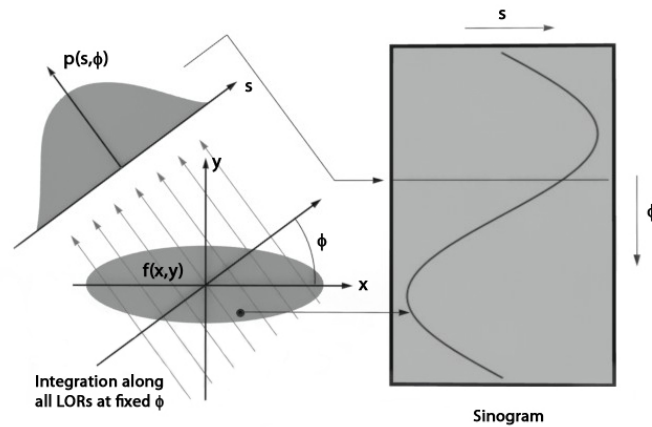


Figure 3.2: A projection $p(s, \phi)$ is formed by integration along all parallel LORs at an angle ϕ . All projections are organized into a sinogram such that each complete projection fills a single row of ϕ in the sinogram. In this format, a single point in the volume $f(x, y)$ traces a sinusoidal path [1].

which is a basis model of the data acquisition process of several imaging modalities such as SPECT, PET and CT.

3.1.2 The Central Slice Theorem

The main goal for the reconstruction of an unknown distribution is to find the inverse Radon transform \mathcal{T}_R^{-1} . The central slice theorem is the fundamental relationship in analytic reconstruction. This theorem states that the Fourier transform of a one-dimensional projection is equivalent to a section at the same angle through the center of the two-dimensional Fourier transform of the object [5]:

$$P(v_s, \phi) = F(v_x, v_y)|_{v_s=0} \quad (3.2)$$

where $\mathcal{F}_{1D}\{p(s, \phi)\} = P(v_s, \phi)$ is the one-dimensional Fourier transform of a projection, $\mathcal{F}_{2D}\{f(x, y)\} = F(v_x, v_y)$ is the two-dimensional Fourier transform of the object and v_x is the Fourier space conjugate of x as illustrated in figure 3.3. The central slice theorem indicates that if $P(v_s, \phi)$ is known at all angles $0 \leq \phi \leq \pi$, then values can be filled in for $F(v_x, v_y)$. The inverse two-dimensional Fourier transform of $F(v_x, v_y)$ will then return

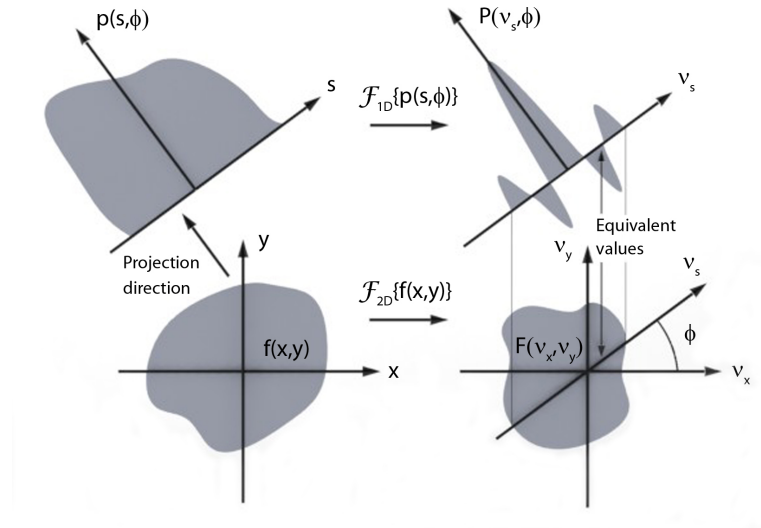


Figure 3.3: Illustration of the two-dimensional central slice theorem, showing the equivalency between the one-dimensional Fourier transform of a projection at angle ϕ and the central section at the same angle through the two-dimensional Fourier transform of the object [1].

the unknown object $f(x, y)$.

3.1.3 Backprojection

An essential step in reconstruction is backprojection $b(x, y)$ which can be described as placing a value of $p(s, \phi)$ back into an image array along the appropriate LOR and a certain angle ϕ which is defined as:

$$b(x, y) = \int_0^\pi p(s, \phi) ds \quad (3.3)$$

As the knowledge where the values came from was lost in the projection step, a constant value will be placed into all elements along the LOR. Due to oversampling in the center of the Fourier transform straight backprojection of all the collected projections will not return the image. Each projection fills in one slice of the Fourier space resulting in oversampling in the center and less sampling at the edges. This oversampling needs to be re-weighted in order to have equal contributions throughout the FOV. In principle the Fourier transform of the backprojected image must be filtered with a two-dimensional cone filter $v = \sqrt{v_x^2 + v_y^2}$ which accentuates values at the edges of the Fourier space and deaccentuates values at the center of the Fourier space. This operation is summarized in:

$$F(v_x, v_y) = vB(v_x, v_y) \quad (3.4)$$

where $B(v_x, v_y)$ is the two-dimensional Fourier transform of the backprojected image and $F(v_x, v_y)$ is the two-dimensional Fourier transform of the backprojected-filtered image. The inverse Fourier transform of $F(v_x, v_y)$ will then yield to the image $f(x, y)$:

$$f(x, y) = \mathcal{F}_{2D}^{-1}\{v\mathcal{F}_{2D}\{b(x, y)\}\} \quad (3.5)$$

This method is known as backprojection-filtering (BPF) image reconstruction, where

the projection data are first backprojected, filtered in Fourier space with a cone filter and then inverse Fourier transformed.

3.1.4 Filtered Backprojection (FBP)

If the order of filtering and backprojection steps in equation 3.4 is interchanged the widely used filtered backprojection method (FBP) is obtained:

$$f(x, y) = \int_0^\pi p^F(s, \phi) d\phi \quad (3.6)$$

where the filtered projection, given by

$$p^F(s, \phi) = \mathcal{F}_{1D}^{-1}\{|v_s| \mathcal{F}_{1D}\{p(s, \phi)\}\} \quad (3.7)$$

can be regarded as precorrected for the oversampling of the Fourier transform of $f(x, y)$. The one-dimensional ramp filter $|v_s|$ is a section through the rotationally symmetric two-dimensional cone filter $v = \sqrt{v_x^2 + v_y^2}$.

The inverse problem of equation 3.1 is ill-posed and its solution from equation 3.7 is unstable in the sense that a small perturbation of the data $p(s, \phi)$ can lead to an unpredictable change in the estimate of $f(x, y)$. Photon detection is a stochastic process. Therefore some sort of regularization is required to constrain the solution space to physically acceptable values. The most common form of regularization in image reconstruction is via simple smoothing. Within the FBP algorithm this can be written as:

$$f(x, y) \approx \tilde{f}(x, y) = \int_0^\pi \mathcal{F}_{1D}^{-1}\{W(v_s)|v_s| \mathcal{F}_{1D}\{p(s, \phi)\}\} \quad (3.8)$$

where $\tilde{f}(x, y)$ is the reconstructed estimate of $f(x, y)$ and $W(v_s)$ is the smoothing function. The effect of the smoothing function in combination with the ramp filter is to suppress amplification of high-frequency noise power above the cut-off frequency $W(v_s)$. The specific shape of $W(v_s)$ will determine the noise/resolution trade-offs in the reconstructed image and affect the noise co-variance in the image. In practice, the proper choice of $W(v_s)$ is difficult to make but at least $W(v_s)$ should be chosen to optimize a specific task, such as lesion detection.

3.2 Iterative Reconstruction

Analytical Reconstruction algorithms such as FBP typically allow fast computation of tomographic images. Because real acquired PET data are not precisely described by the FBP model, the resulting images can exhibit significant inaccuracies. In contrast to analytical methods, iterative approaches can model the mapping from source to detector without explicitly solving a line-integral. Iterative reconstruction algorithms in addition incorporate probabilistic models of noise and attenuation mechanisms in the imaging process. These improvements come at the cost of a more complex mathematical problem which is more difficult to solve than that of Radon transform inversion. They are not providing a direct analytical solution or an analytical solution cannot be found with current processing capabilities. Consequently, these more realistic approaches are often solved with methods that progressively refine the estimated image in a repetitive

calculation. The principal trade-off between iterative techniques and FBP is accuracy versus efficiency. All iterative methods require a certain number of repeated calculations of projection and backprojection operations. Thus, they need a substantially longer computation time than FBP. Advances in computation speed and faster algorithms have helped to overcome the computational burden of iterative methods allowing them to receive growing clinical acceptance.

Generally, iterative methods contain five components. The first component is a model of the image. This is usually a discretization of the image domain into N distinct pixels for two-dimensional image elements or voxels for three-dimensional image elements. Other models have been proposed such as spherical elements [6] with overlapping boundaries.

The second component is a system model that relates the image to the data. The system model or system matrix (SM) characterizes the imaging system where one element H_{ij} represents the probability that an emission from pixel j is detected in projection i . Therefore,

$$\bar{p}_i = \sum_{j=1}^N H_{ij} f_j \quad (3.9)$$

where p_i is the mean of the i -th projection and f_j is the activity in pixel j as illustrated in figure 7.13.

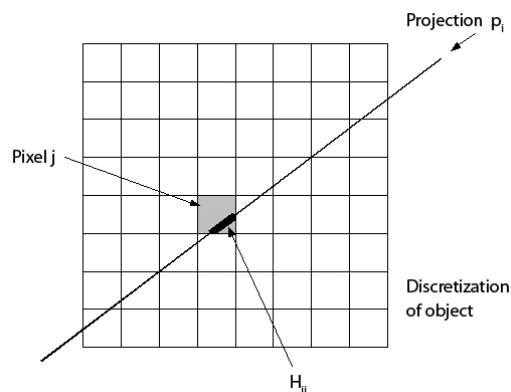


Figure 3.4: Illustration of a single element of the system matrix H_{ij} .

The model of the projection process can become as simple or as complex as required because the intensity of a projection bin i is a weighted sum of intensities of the image pixels. In order to represent the Radon model, the matrix elements are defined in a way that one projection bin receives contributions only from pixels intersected by a given line and contributions of pixels that do not intersect the line are set to zero. In a more realistic case, each projection bin receives contributions from many pixels weighted according to the relative sensitivity of the projection bin to each pixel. All these contributions are affected by physical factors such as attenuation, detector response, scatter and can be estimated from knowledge of the system design and its properties. Different methods to generate a system matrix will be presented in chapter 6.

The third component is a model for the data, which in statistical methods describes the relationship between the value of the measurements and the expected value of the measurements. This model relates how the projection measurements vary around their expected mean values. As photon detection is Poisson distributed the majority of methods

is using a Poisson model. For M projections the Poisson probability law states that the probability L for counting P Poisson distributed photons equals the true photon counts p for a given vector of emission rates, is

$$L(P = p|f) = \prod_{i=1}^M \frac{\bar{p}_i^{p_i} \exp(-\bar{p}_i)}{p_i!} \quad (3.10)$$

Although the Poisson model is a good description of PET imaging, once the corrections for randoms, scatter and attenuation are applied, the data no longer follow Poisson statistics. Other models such as approximations of the Poisson model [7], shifted Poisson [8] and Gaussian models have been proposed to improve model accuracy.

With the description of the image, the measurements and the system relating the two, a principle has to be adopted that defines the best image. The governing principle is often expressed mathematically as a cost or objective function. The most common principle used in iterative reconstruction is the Maximum Likelihood (ML) approach, a standard statistical estimation method proposed by R.A. Fisher [9]. In this approach, the probability relationship in equation 3.10 is a likelihood function of the object f where an estimate of the object \hat{f} has to be chosen that provides the greatest value of L . The ML criterion can be written as the following:

$$\hat{f} = \operatorname{argmax}_f L(P = p|f) \quad (3.11)$$

ML estimators are advantageous because they are asymptotically unbiased, meaning that as the number of observations becomes large, the estimates become unbiased. These estimators are also proven to provide the least variance among all possible unbiased estimators, leading to an estimate with less noise than other unbiased estimators [10].

The final component of iterative methods is an algorithm that optimizes the cost function or finds the best image estimate. Many algorithms have been proposed in literature ranging from gradient-based algorithms [11] to the most commonly used expectation maximization (EM) algorithm first discussed in 1977 by Dempster et al. [12]. The EM algorithm offers a numerical method for determining a maximum likelihood estimate (MLE). The ML-EM algorithm, since its introduction in 1982 by Shepp and Vardi [13], remains a basis for the most popular statistical reconstruction methods and has provided the foundation of many other methods. The ML-EM framework yields the following iterative equation:

$$\hat{f}_j^{(n+1)} = \frac{\hat{f}_j^{(n)}}{\sum_{i'} H_{i'j}} \sum_i H_{ij} \frac{p_i}{\sum_k H_{ik} \hat{f}_k^{(n)}} \quad (3.12)$$

where $\hat{f}_j^{(n+1)}$ is the next estimate of pixel j based on the current estimate $\hat{f}^{(n)}$. This algorithm is qualitatively described with figure 3.5, starting with an initial image guess $\hat{f}^{(0)}$, shown in the upper left of the figure. This initial guess is usually the entire image set to a constant value. The first step (1) forward projects the image to projection domain. In step (2) these projections are compared with the measured projections p . A correction factor for each projection is formed, which is then in step (3) backprojected into image domain to obtain a correction factor for the initial image estimate. This correction factor is multiplied by the current image estimate and divided by a weighting term based on the SM to apply the desired strength of each image correction factor (4). The new image

estimate is then reentered in the algorithm as the next image. The algorithm will be repeated till the estimate approaches the maximum likelihood solution.

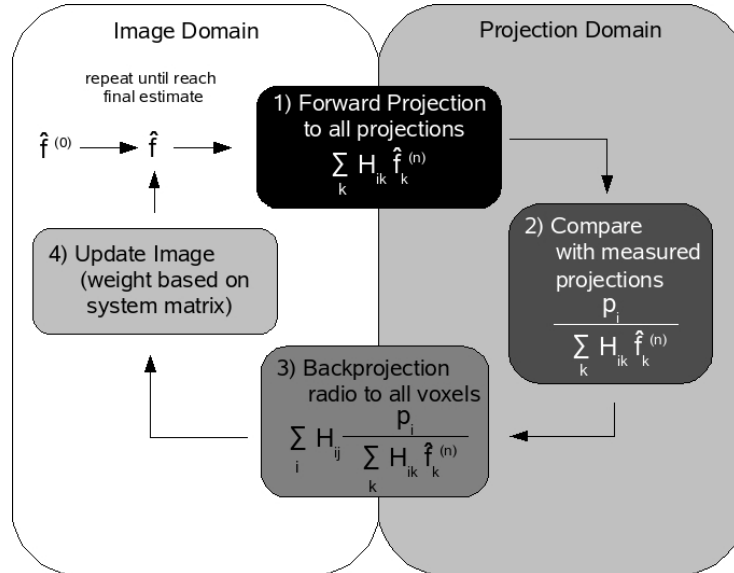


Figure 3.5: Flow diagram of the maxim likelihood-expectation maximization algorithm. Starting with an initial image guess $\hat{f}^{(0)}$ in the upper left, the algorithm iteratively chooses a new image estimate based on the measured projections p [2].

The ML-EM algorithm has two main drawbacks. First, the convergence rate of the algorithm is slow and image dependent. A proper solution may require 20-50 iterations or even more. Considering that ML-EM takes one forward and one backward projection for each iteration, the overall processing can be expected to require in the order of one or two orders of magnitude more time than FBP. Second, the ML criterion yields very noisy reconstructed images, as the estimate approaches the ML solution. In practice, the ML-EM algorithm provides good results if the iterative process is stopped before reaching the ML solution and by post-smoothing the reconstructed images. Several approaches for deciding when to stop the iterations were proposed after the introduction of the ML-EM algorithm [14]. The behavior of the ML-EM algorithm with different iterations is demonstrated in figure 3.6, which shows a phantom consisting of different cylinders with increasing diameter from 1 mm to 5 mm. The ML-EM algorithm has been shown consistently to cause low frequencies to appear first and then gradually to develop higher spatial frequencies as the integrations progress [15]. The figure also shows the image noise increasing as the estimate approaches the ML solution.

To access the problem of slow convergence a variation of the ML-EM algorithm was introduced in 1994 by Hudson and Larkin [16]. The ordered subsets expectation maximization (OSEM) uses, as the name indicates, subsets of the entire data set for each image update in the form

$$\hat{f}_j^{(n+1)} = \frac{\hat{f}_j^{(n)}}{\sum_{i' \in S_b} H_{i'j}} \sum_{i \in S_b} H_{ij} \frac{p_i}{\sum_k H_{ik} \hat{f}_k^{(n)}} \quad (3.13)$$

where the backprojections are performed only over the projections in subset S_b of a total of B subsets. The image is updated during each subiteration and one complete

iteration will have B image updates. When only one subset ($B = 1$) is used, the OSEM algorithm reduces to the ML-EM algorithm.

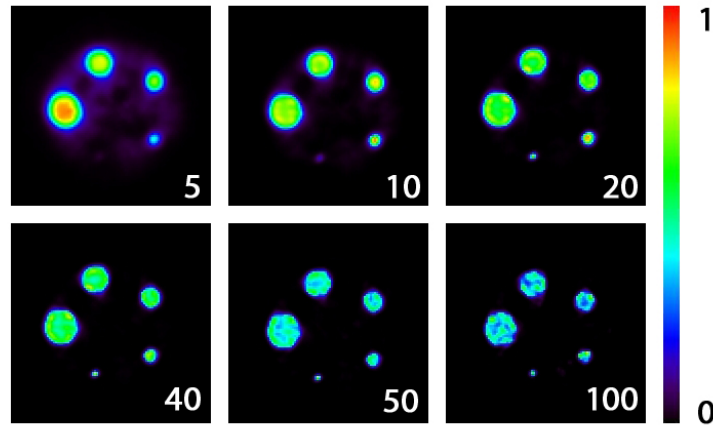


Figure 3.6: Convergence properties of the ML-EM algorithm. Progression of iterated image estimates from simulated data consisting of different cylindrical phantoms. The simulations were done with the software package GATE [17]. The numbers in each subimage indicate the iteration number. The simulations were done for the MADPET-3 scanner, which will be discussed in details in chapter 5.

References

- [1] M.N. WERNICK, J.N. AARSVOLD, *Emission Tomography, The Fundamentals of PET and SPECT*, Elsevier Academic Press, 2004, ISBN 0-12-744482-3
- [2] A. ALESSIO AND P. KINAHAN, *PET Image Reconstruction*, Nuclear Medicine (2nd ed.), Henkin et al., Eds., Philadelphia, Elsevier, 2006, also available under: <http://faculty.washington.edu/aalessio/>
- [3] H.H. BARRETT, *The Radon transform and its applications*, In. E. Wolf, editor, Progress in optics XXI, chapter III, Elsevier Science Publishers B.V., 1984
- [4] J. RADON, *Über die Bestimmung von Funktionen durch ihre Integrale längs gewisser Mannigfaltigkeiten*, Number 69 in Math. Phys. Kl. Ber. Verh. Saechs. Akad. Leipzig, 1917 [Translation by: P.C. Parks in IEEE Trans. Med. Imag., MI-5, 170, 1986]
- [5] A.C. KAK AND M. STANEY, *Principles of Computersized Tomographic Imaging*, New York: IEEE Press, 1988
- [6] S. MATJE AND R.M. LEWITT, *Practical considerations for 3-D image reconstruction using spherically symmetric volume elements*, IEEE Trans. Med. Imag., vol. 15, pp. 68-78, 1996
- [7] C.A. BOUMAN AND K. SAUER, *A Unified Approach to Statistical Tomography Using Coordinate Descent Optimization*, IEEE Trans. on Image Processing, vol. 5, pp. 480-492, 1996
- [8] M. YAVUZ AND J.A. FESSLER, *Statistical image reconstruction methods for randoms-precorrected PET scans*, Med. Imag. Analysis., vol. 2, pp. 369-378, 1998
- [9] R.A. FISHER, *On the "probable" error of a coefficient of correlation deduced form a small sample*, Metron 1, pp. 3-32, 1921
- [10] H.L. VAN TREES, *Detection, Estimation, and Modulation Theory, Part I.*, John Wiley & Sons, New York, 1968
- [11] O. AXELSSONS, *Iterative solution methods*, Cambridge University Press, 1994
- [12] A. DEMPSTER, N. LAIRD, AND D. RUBIN, *Maximum likelihood from incomplete data via the EM algorithm*, Journal of the Royal Statistical Society, vol. 39, pp. 1-38, 1977
- [13] L. SHEPP AND Y. VARDI, *Maximum Likelihood Reconstruction for Emission Tomography*, IEEE Trans. Med. Imag., MI-1, pp. 113-122, 1982
- [14] J. LLACER AND E. VEKLEROV, *Feasible images and stopping rules for iterative algorithms in transmission tomography*, IEEE Trans. Med. Imag., vol. 8, pp. 186-193, 1989
- [15] S.D. WILSON, B.M.W. TSUI, H.H. BARRETT, *Noise properties of the EM algorithm, II Monte Carlo Simulations*, Phys. Med. Biol., vol. 39, pp. 847-871, 1994

- [16] H.M. HUDSON AND R.S. LARKIN, *Accelerated image reconstruction using ordered subsets of projection data*, IEEE Trans. Med. Imag., vol. 13, pp. 601-609, 1994
- [17] GATE, *Geant4 Application for Tomographic Emission: a simulation toolkit for PET and SPECT*, <http://www.opengatecollaboration.org/>

Chapter 4

Monte Carlo Simulations

MONTE CARLO (MC) simulations are frequently used in Nuclear Medicine to deal with a variety of problems that are difficult to study by an experimental or analytical approach [1]. The name Monte Carlo is inspired by the gambling casinos at the city of Monte Carlo in Monaco. The mathematical techniques used by this method are based on repeated random variable sampling. The MC method can be considered as a general mathematical tool for the solution of a diversity of problems. The applications of MC methods can be divided into two major groups. The first group consists of systems that are already statistical in their nature. The second group consists of MC methods invented for the solution of well defined mathematical equations. The majority of real cases is often a mixture of the extreme limits [2]. The simulation of a scintillation detector or a whole PET detector system is a good example. The application of MC techniques into the field of medical radiation physics started quite soon after the introduction of the method [3], [4], [5]. Several MC software packages were developed ranging from general purpose codes, mainly for particle transportation, to dedicated codes, designed specially for SPECT and PET. A wide range of topics can be addressed by MC simulations, among with optimization of imaging system design, development and evaluation of correction methods, assessment of image reconstruction algorithms, pharmaco-kinetic modelling [6], [7]. In addition, MC simulations also allow studies of parameters which are experimentally not measurable, for example the number of random coincidences. This chapter will give a summary of the most common open source MC software packages, that have been used in this work.

4.1 DETECT2000

DETECT2000 is a Monte Carlo simulation software package for studying optical systems with a special emphasis on scintillation detectors [8]. DETECT2000 is one of the successors of the DETECT software that was originally developed at the University of Michigan [9]. Many previous studies show that DETECT2000 is capable of estimating the response of photo-detectors very accurately when compared to measured data [10], [11], [12], [13].

It generates individual scintillation photons in specified position of a scintillation crystal, follows each photon in its passage through the various components and interactions with surfaces and records the final fate (absorption, escape, or detection) of each. Scintillation decay times and delays before detection upon interaction with a photosensor may be sampled from user specified probability distribution functions. In addition, decay and

delay times, total elapsed time to detection, number of reflecting surfaces encountered and last coordinates are recorded for each photon traced.

DETECT2000 defines a very general syntax for geometry specification to allow the representation of complex systems and many different elements. One element may consist of a volume determined by multiple planar, cylindrical, conical or spherical surfaces with arbitrary orientation. More complex shapes can be generated by contiguous elements with common "pseudo surfaces" that will be ignored by the simulation. The optical behaviour of real surfaces may be specified to simulate possible reflection under polished, ground, painted or metallized conditions. Surfaces in optical contact are treated using Snell's law of refraction. Within each optical element, bulk absorption and scattering are taken into account by defining a mean distance of photon travel length for each process.

Photons are isotropically generated within a defined material and volume subset of the system. Photons are tracked on an individual basis until they are absorbed, detected, or have escaped from the system. At each photon reflection or scattering, the program determines the new direction of the photon, identifies the component in which it is travelling and computes the next intersection with a surface. A random sampling is then made to determine if the photon is bulk absorbed or scattered over this path. If none of these processes occur, the optical properties of the next surface determine whether the photon is reflected, refracted, detected or absorbed. The process is then repeated for all subsequent paths in the history. A maximum flight time per history is specified to abort those cases in which a photon becomes internally trapped.

The source code of DETECT2000 was available for download at:
<http://www.gel.ulaval.ca/detect>.

4.1.1 Surface Models in DETECT2000

Six different types of optical finishes are allowed for component surfaces in DETECT2000. Each surface is considered to be build up by micro-facets with normal vectors that follow a given distribution. All surface models may be determined by a certain set of parameters which will be described in the following accordingly to the DETECT2000 user's guide [8]. Figure 4.1 illustrates the coordinate system used in in these models along with the definition of a set of parameters:

- ◇ \vec{d}_i - the direction vector of the incident photon
- ◇ \vec{d}_r - the direction vector of the reflected photon
- ◇ \vec{d}_t - the direction vector of the refracted photon
- ◇ \vec{n} - the average normal of the surface
- ◇ \vec{n}' - the normal of a particular micro-facet
- ◇ θ_i - the angle of incidence relative to the average normal
- ◇ θ_r - the angle of reflection with respect to the average normal
- ◇ θ_t - the angle of refraction with respect to the average normal
- ◇ θ'_i - the angle of incidence relative to the micro-facet normal

- ◇ θ'_i - the angle of reflection with respect to the micro-facet normal
- ◇ θ'_t - the angle of refraction with respect to the micro-facet normal
- ◇ α - the angle between a given micro-facet and the mean surface
- ◇ ϕ_{norm} - the angle between the projection of the micro-facet normal onto the average surface and the plane of incidence
- ◇ ϕ_r - the angle between the projection of the reflected or refracted photon onto the average surface and the plane of incidence

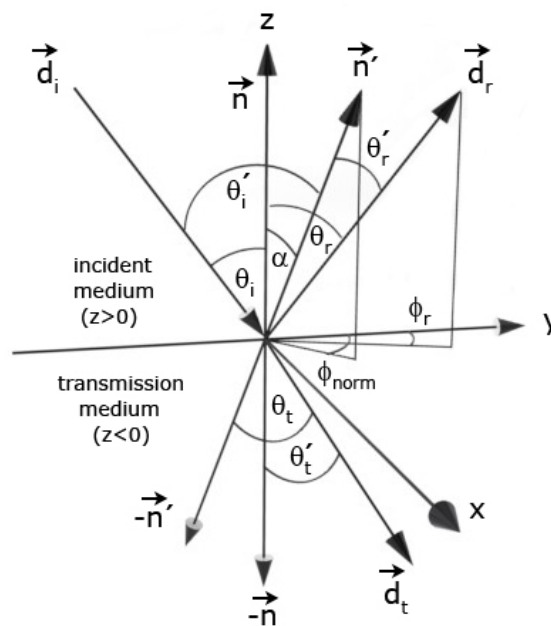


Figure 4.1: Coordinate system used in micro-faceted surface models along with the definition of geometrical parameters [8].

DETECT

This specification represents a photosensor such as a photocathode or any other photon detecting layer. All DETECT surfaces may be specified by a quantum efficiency and a photosensor response time.

METAL

This surface is assumed to be smooth and covered with a metallized coating representing a specular reflector. A random sampling determines whether the photon is absorbed at the surface or undergoes reflection at an angle equal to the angle of incidence. Transmission is not considered and therefore jumps in the index of refraction at the surface interface are irrelevant.

PAINT

This surface is assumed to be painted with a diffuse reflecting material characterized by a reflection coefficient. If random sampling shows that reflection occurs, it is assumed

to be Lambertian. In this case, the angle of reflection is independent of the angle of incidence, and is sampled from a distribution given by $I(\theta) = I_0 \cos(\theta)$, where θ is the angle with respect to surface normal. As with the METAL surface, transmission is not considered.

POLISH

A polished surface may be specified by a reflection coefficient representing the probability that, if a photon escapes from the surface, it is returned to the original medium by Lambertian reflection. Photons incident on the surface are assumed to have random polarization, and are first tested for the possibility of Fresnel reflection if a change in refractive index occurs at the surface. This probability is given by

$$R = \frac{1}{2} \left[\frac{\sin^2(\theta'_i - \theta'_t)}{\sin^2(\theta'_i + \theta'_t)} + \frac{\tan^2(\theta'_i - \theta'_t)}{\tan^2(\theta'_i + \theta'_t)} \right], \quad (4.1)$$

where θ'_i and θ'_t are respectively the angles of incidence and refraction with respect to a local micro-facet's normal which is always taken to be parallel to the average surface normal to treat a perfectly polished surface interface. If reflection is selected, the angle of reflection is set equal to the angle of incidence. If reflection does not occur, the photon is transmitted with the complementary probability of:

$$T = 1 - R, \quad (4.2)$$

and assumed to obey Snell's law of refraction:

$$\frac{\sin(\theta'_i)}{\sin(\theta'_t)} = \frac{n_2}{n_1}, \quad (4.3)$$

where n_1 and n_2 are the refractive indices of the first and second components respectively. The radiant intensity can be used to mathematically describe the distribution of light created by reflection and transmission by the POLISH surface model. The radiant intensity J is defined as the photon flux $d\phi$ passing through the solid angle $d\omega$, $J = d\phi/d\omega$. For a perfect polished surface the radiant intensity may be expressed as follows:

$$J_{POLISH}(\theta_i, \theta_r, \phi_r) = [R(\theta_i, n_1, n_2)\delta(\theta_i - \theta_r) + T(\theta_i, n_1, n_2)\delta(\theta_t - \theta_s)]\delta(\phi_r) \quad (4.4)$$

with $\theta_s = \sin^{-1}(\frac{n_1}{n_2}\sin\theta_i)$. A polar plot of the intensity of the POLISH surface model is shown in figure 4.2 (a).

GROUND

This surface specification simulates a roughened or ground optical surface. It is treated in the same way as the polished surface described above, except that the normal to the surface used in the refraction calculation is randomly distributed, following a Lambertian distribution, around the surface normal as shown in figure 4.2 (b). In addition a reflection coefficient can be specified to simulate an external diffuse reflector for those photons that pass through the surface. A perfect diffuse or Lambertian surface which appears equally bright from all directions is characterized by the radiant intensity: $J_L = \cos(\theta_r)$.

Therefore the radiant intensity for a GROUND surface may be express similar to the POLISH surface model:

$$J_{GROUND}(\theta_i, \theta_r, \phi_r) = \cos(\alpha_r)R(\theta'_r, n_1, n_2) + \cos(\alpha_t)T(\theta'_t, n_1, n_2) \quad (4.5)$$

UNIFIED

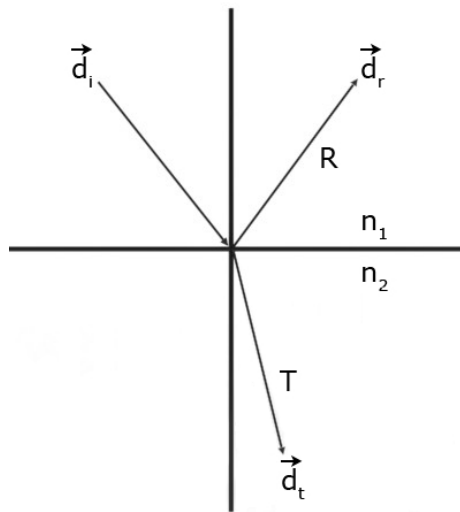
In order to simulate interaction of thin layers with dielectric surfaces a new surface model UNIFIED has been implemented in the latest version of the software package [14]. In contrast to the POLISH and GROUND models of DETECT2000, the UNIFIED model offers to simulate a wide range of surface roughness. The angle between a micro-facet normal and the average surface normal α is assumed to follow a Gaussian distribution with the standard deviation σ_α . In the UNIFIED model also a reflection coefficient RC can be specified to represent an external diffuse reflector with an certain index of refraction N_{rc} for the reflective coating material. In addition to σ_α and N_{rc} , the UNIFIED model offers the possibility to control the radiant intensity of the surface by four more coefficients:

- ◇ C_{sl} , the specular lobe coefficient, represents the probability of specular reflection about the normal of a micro-facet;
- ◇ C_{ss} , the specular spike coefficient, represents the probability of specular reflection about the average normal of the surface;
- ◇ C_{dl} , the diffuse lobe coefficient, describes the probability of internal Lambertian reflection;
- ◇ C_{bs} , the back scatter spike coefficient, controls the probability of backward reflection. This occurs when a photon hits a micro-facet at a normal angle and after multiple reflections within a deep groove, is reflected back along its original path.

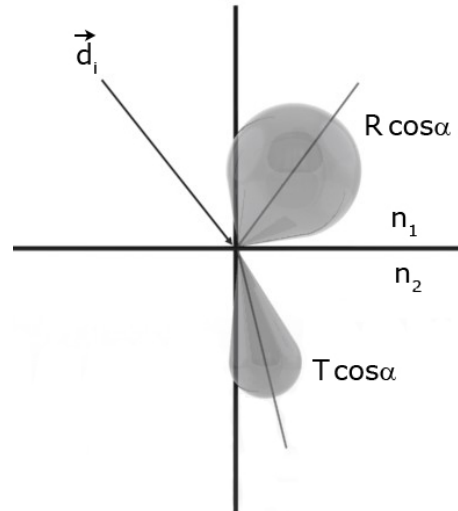
A good approximation for the radiant intensity of the UNIFIED surface model may be expressed by:

$$\begin{aligned} J_{UNIFIED}(\theta_i, \theta_r, \phi_r) \approx & R(\theta'_r, n_1, n_2)[C_{sl}g(\alpha_r, 0, \sigma_\alpha) \\ & + C_{ss}\delta(\theta_i - \theta_r)\delta(\phi_r) + C_{bs}\delta(\theta_i + \theta_r)\delta(\phi_r) \\ & + C_{dl}\cos(\theta_r)] \\ & + T(\theta'_t, n_1, n_2)[C_{sl}g(\alpha_t, 0, \sigma_\alpha) \end{aligned} \quad (4.6)$$

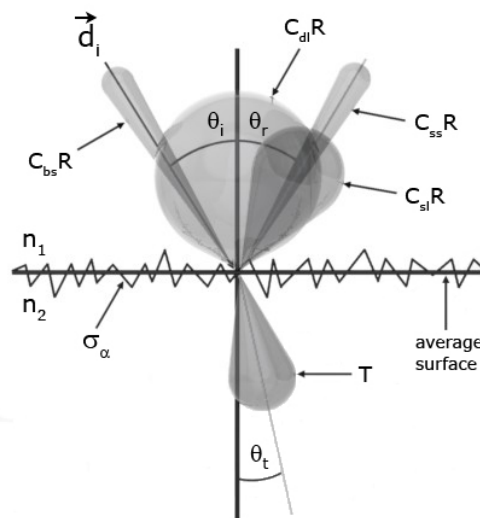
where $g(\alpha, 0, \sigma_\alpha)$ is a Gaussian with a mean of 0° and a standard deviation of σ_α , for $\alpha_t \in [0, 90^\circ]$. A polar plot of the radiant intensity of the UNIFIED model along with all the coefficients that control their probability is shown in figure 4.2 (c). The expression in equation (7.6) for the radiant intensity $J_{UNIFIED}$ emphasizes that several surface models are unified into a single parametrization. For instance, if $n_1 = n_2$, the transmission coefficient T equals 1 and the UNIFIED model reverts to the PAINT surface finishing. Setting $C_{sl} = 1$ and $\sigma_\alpha = 0$ leads to the radiant intensity of the POLISH model.



(a) POLISH surface model



(b) GROUND surface model



(c) UNIFIED surface model

Figure 4.2: Polar plot of the radiant intensity of the POLISH (a), GROUND (b) and UNIFIED (c) surface models in DETECT2000 [8].

4.2 GEANT4

The GEANT4 (**GE**ometry **ANd** **T**racking) toolkit provides a comprehensive software package for simulation applications that involve the interaction and passage of particles through matter. GEANT4 is the newest version from the GEANT series of software toolkits developed by CERN [15], and the first one using object oriented programming in C++. It covers a wide range of physical processes including electromagnetic, hadronic and optical processes, a large set of long-lived particles, material and elements over a broad energy range (from 250 eV to 1 PeV) [16], [17]. In the framework for modelling the optics of scintillation detectors one implementation for the boundary processes between different surfaces employs the UNIFIED model [14] of the DETECT2000 program [8]. Therefore, for modelling light transport with the UNIFIED surface model similar results for DETECT2000 and GEANT4 have to be expected [18]. The physics modelling capabilities are complemented by an extensive validation of existing models against authoritative reference data and experimental results [19], [20], [21], [22], [23], [24]. The software is freely available at source-code level over the Web [25].

4.3 GATE

GATE, the GEANT4 Application for Tomographic Emission, is an object-oriented simulation platform build on top of the multi-purpose simulation toolkit GEANT4. GATE encapsulates the GEANT4 libraries in order to achieve a modular, versatile and scripted simulation toolkit adapted to the field of nuclear medicine. It incorporates all GEANT4 features including validated physics models, geometry modelling tools, visualization and 3D rendering [26]. GATE was developed within the OpenGATE Collaboration [27] with the objective to provide a free software simulation platform dedicated for PET and SPECT.

The core layer closed to the GEANT4 kernel comprises the basic classes that define the mechanism to manage time, geometry, sources and read-out [28]. The application layer implements concrete classes derived from the basic classes of the core layer, e.g. to build specific volume shapes (boxes, spheres) or operations on these volumes such as rotation or translation. It is also possible to extend the functionalities of GATE by developing new classes in the application layer. On the user level a full set-up and control of a simulation is performed using interactive scripting or execution of macros.

GATE allows to handle time dependent phenomena such as geometries with moving objects or sources with time-dependent activities. The synchronizing of all time-independent components allows a coherent description of the acquisition process [29]. Movements of geometrical components are dynamically created and their parameters are controlled by scripting.

Radioactive sources may be specified by their isotope, decay time, position and activity, which may overlap with each other or may overlap with the detector geometry (e.g. the natural radioactivity of Lu of an LSO scintillation crystal). A specific development is integrated in GATE to generate radioactive decay times following a chronicle time flow [28]. If more than one type of source is defined in the simulation, the source manager chooses randomly which source is going to decay from the current activities of all sources. The chronicle time flow allows modelling of time-dependent processes such as count rates, pile up or dead time.

The construction and definition of geometrical components is one of the most time-consuming tasks in a standard GEANT4 simulation. In GATE some tools are available for building a GEANT4 geometry without C++ coding using automated code generation. A dedicated scripting mechanism allows modelling of complex geometries. In a first step basic volume shapes are created together with their parameters (dimensions, material, position). Then, these basic volume shapes may be replicated following regular patterns such as arrays or rings. Visualization options as provided in GEANT4 are also available in GATE. Together with the scripted geometry creation, interactive visualization allows the on-the-fly introduction of new geometrical components and to see the effect of the changes in their parameters and positions.

Once the geometry of a scanner has been defined, a sensitive detector (SD) has to be attached to some geometrical components. These sensitive detectors are used to store information on interactions of a particle from certain steps, also addressed as hits, along a particle track. A hit is a snapshot of a physical interaction of a track in a sensitive region of the detector. With a hit various information is stored such as the energy deposition of a step, position and time of a step.

Two different types of sensitive detectors can be specified:

- ◇ **The crystalSD** records information on interactions inside the volumes belonging to a scanner. These volumes are mainly meant to be scintillating elements but may also be attached to non-scintillating elements such as collimators. In a crystalSD the energy deposition, the positions of interaction, the origin of the particle and the type of interaction are stored.
- ◇ **The phantomSD** may be used to store information on Compton and Rayleigh interactions taking place in some geometrical components in the FOV before the detection in the scanner system. This information is then used to estimate whether a photon reaching a detector is a direct or a Compton-scattered photon.

Gamma-ray interactions which should be considered in the simulation may be selected among those provided by the Geant4 packages:

- ◇ Standard Energy Electromagnetic Processes (SEP)
- ◇ Low Energy Electromagnetic Processes (LEP)

With the SEP, it is possible to simulate photoelectric and Compton interactions with an energy higher than 10 keV. The LEP whereas represents electromagnetic interactions at lower energies down to 250 eV and covers elements with an atomic number between 1 and 99.

To use all the interaction histories, recorded as hits, in order to mimic realistic output data a dedicated module is realized. The purpose of the digitizer module is to simulate the behaviour of the detectors and the signal processing chain. A particle often creates multiple interactions and therefore multiple hits within a given crystal. As illustrated in figure 4.3 one photon may interact by two Compton scattered events and a photoelectric absorption. The digitizer module sums up all the hits that occur within the same crystal or the same volume. This is equivalent to an electronically readout system measuring an integrated signal which is not containing time or energy resolution necessary to distinguish

between the individual interactions of a particle within a crystal. This part of the digitizer module is completed by a module called adder. In order to model the detector output correctly, the readout depth of the adder must be set to the geometrical component, that has the finest readout resolution, otherwise the deposited energies of one gamma ray in different crystals would be summed up to one readout pulse. Apart from the adder other digitizer modules are implemented in GATE allowing to define detector characteristics such as position and energy resolutions, electronics thresholds and dead times.



Figure 4.3: Principe of the adder and readout module [30].

The detection of gamma-rays by scintillating crystals may also include the simulation of all optical processes such as the generation and tracking of optical photons. Although the tracking of optical photons is relatively fast, a simulation with optical photon tracking will be much slower (up to a factor of thousand) than one without [31].

An interface with the ROOT data analysis framework [32] allows real-time visualization. Apart from a ROOT data output format, the simulation results can also be stored in a ASCII file as standard output or in a system dependent output format such as sinogram and ecat7 for the ECAT EXCAT HR+ scanner or List Mode Format (LMF) developed by [33] the for the small animal ClearPET scanner prototypes.

References

- [1] I. BUVAT, I. CASTIGLIONI, *Monte Carlo simulations in SPET and PET*, QJ. Nucl. Med., vol. 46, pp. 48-61, 2002
- [2] C. JACOBONI, AND P. LUGLI, *The Monte Carlo Method for Semiconductor Device Simulation*, Springer-Verlag Wien New York 1989, ISBN 3-2111-82110-4
- [3] R.W. HOCKNEY, R.A. WARRINER, M. REISER, *Two-dimensional particle models in semiconductor-device analysis*, Electron. Lett., vol. 10, pp. 484-486, 1974
- [4] G. BACCARANI, C. JACOBONI, A.M. MAZZONE, *Current transport in narrow-base transistors*, Solid-State Electron., vol. 20, pp. 5-10, 1977
- [5] B. LÜTHI, AND P. WYDER, *A Monte-Carlo Calculation for a Size Effect Problem*, Helv. Phys. Acta., vol. 33, pp. 667-674. 1960
- [6] D. MURRAY, *Using EGS4 Monte Carlo in medical radiation physics*, Australas. Phys. Eng. Sci. Med., vol. 13, pp. 132-147. 1990
- [7] H. ZAIDI, *Relevance of accurate Monte Carlo modelling in nuclear medical imaging*, Med. Phys., vol. 26, pp. 574-608. 1999
- [8] C. MOISAN, F. CAYOUILLE, AND G. McDONALD, *DETECT2000, The Object Oriented C++ Language Version of DETECT*, Laval University, Quebec, Canada, Version 5.0, 2001
- [9] G.F. KNOLL, T.F. KNOLL, T.M. HENDERSON, *Light collection in scintillation detector composites for neutron detection*, IEEE Trans. Nucl. Sci., vol. NS-35, pp. 872-875, 1988
- [10] G. TSANG, C. MOISAN, AND J.G. ROGERS, *A simulation to model position encoding multicrystal PET detectors*, IEEE Trans. Nucl. Sci., vol. 42, pp. 2236-2243, 1995
- [11] F. CAYOUILLE, C. MOISAN, N. ZHANG, AND C.J. THOMSON, *Monte Carlo modelling of scintillator crystal performance for stratified PET detectors with DETECT2000*, IEEE Trans. Nucl. Sci., vol. 49, pp. 624-628, 2002
- [12] F. CAYOUILLE, N. ZHANG, AND C.J. THOMSON, *Monte Carlo Simulation Using DETECT2000 of a Multilayered Scintillation Block to Fit Experimental Data*, IEEE Trans. Nucl. Sci., vol. 50, pp. 339-343, 2003
- [13] C.O. STEINBACH, Á. SZLÁVECZ, B. BENYÓ, T. BÜKKI, AND E. LŐRINCZ, *Validation of DETECT2000-Based PetDetSim by Simulated and Measured Light Output of Scintillator Crystal Pins for PET Detectors*, IEEE Trans. Nucl. Sci., vol. 57, pp. 2460-2467, 2010
- [14] A. LEVIN, AND C. MOISAN, *A More Physical Approach to Model the Surface Treatment of Scintillation Counters and its Implementation into DETECT*, IEEE NSS MIC Conf. Rec. 2, pp. 702-706, 1996

- [15] CERN, *Conseil Européen pour la Recherche Nucléaire*, <http://cern.ch/>
- [16] S. AGOSTINELLI ET. AL., *GEANT4 - a simulation toolkit*, Nucl. Instr. Meth. Phys. Res. A 506, pp. 250-303, 2003
- [17] J. ALLISON ET. AL., *GEANT4 Developments and Applications*, IEEE Trans. Nucl. Sci., vol. 53, pp. 270-278, 2006
- [18] M.A. BLACKSTON, F. HABTE, P.A. HAUSLADEN, *A Comparison of GEANT4 and DETECT2000 for the Simulation of Light Transport in Scintillation Detectors*, IEEE NSS MIC Conf. Rec., pp. 4995-4998, 2008
- [19] K. AMAKO ET. AL., *Comparison of Geant4 electromagnetic physics models against the NIST reference data*, IEEE Trans. Nucl. Sci., vol. 52, pp. 910-918, 2005
- [20] XCOM: Photon Cross Section Database (Version 3.1), M.J. BERGER, J.H. HUBBELL, S.M. SELTZER, J. CHANG, J.S. COURSEY, R. SUKUMAR, D.S. ZUCKER, AND K. OLSEN, <http://physics.nist.gov/pml/data/xcom/index.cfm>
- [21] ESTAR, PSTAR, AND ASTAR: Computer Programs for Calculating Stopping-Power and Range Tables for Electrons, Protons, and Helium Ions, M.J. BERGER, J.S. COURSEY, D.S. ZUCKER, AND J. CHANG, <http://physics.nist.gov/pml/data/star/index.cfm>
- [22] G.A.P. CIRRONE ET. AL., *Precision validation of Geant4 electromagnetic physics*, IEEE NSS MIC Conf. Rec. 1, pp. 482-485, 2003
- [23] A. RIBON, *Physics validation of the simulation packages in a LHC-wide effort*, in Proc. Comp. in High Energy Phys., vol. 493, Interlaken, Switzerland, 2004
- [24] C. ALEXA ET. AL., *Geant4 Hadronic Test Beam Validation With Test Beam Data: First Conclusions*, CERN-LCGAPP-2004-10, <http://sftweb.cern.ch/validation/?q=node/21>
- [25] GEANT4 COLLABORATION, <http://geant4.cern.ch/>
- [26] G. SANTIN ET. AL., *GATE, a Geant4-based simulation platform for PET integrating movement and time management*, IEEE NSS MIC Conf. Rec. 2, pp. 1325-1329, 2002
- [27] GATE: GEANT4 APPLICATION FOR TOMOGRAPHIC EMISSION, <http://www.opengatecollaboration.org/>
- [28] D. STRUL, G. SANTIN, D. LAZARO, V. BRETON, AND C. MOREL, *GATE(Geant4 Application for Tomographic Emission): a PET/SPECT general-purpose simulation platform*, Nucl. Phys. B (Proc. Suppl.), vol. 125, pp. 75-79, 2003
- [29] G. SANTIN, D. STRUL, D. LAZARO, L. SIMON, M. KRIEGUER, M. VIEIRA MARTINS, V. BRETON and C. MOREL *GATE, a Geant4-based simulation platform for PET and SPECT integrating movement and time management*, IEEE Trans. Nucl. Sci., vol. 50, pp. 1516-1521, 2003
- [30] A. VELROYEN, *Development of a Novel Detector Module for PET/MR Imaging Based on SiPMs and Fast Scintillation Crystals*, Diploma Thesis in Physics, Fakultät für Physik, Ludwig-Maximilians-Universität München, 2010
- [31] GATE USERS GUIDE: GATE - Geant4 Application For Tomographic Emission: a simulation toolkit for PET and SPECT, <http://www.opengatecollaboration.org/>

[32] ROOT, *A data analysis framework*, <http://root.cern.ch/>

[33] CRYSTAL CLEAR COLLABORATION - A Multi-disciplinary enterprise,
<http://crystalclear.web.cern.ch/crystalclear/>

Chapter 5

Small Animal PET Imaging Systems

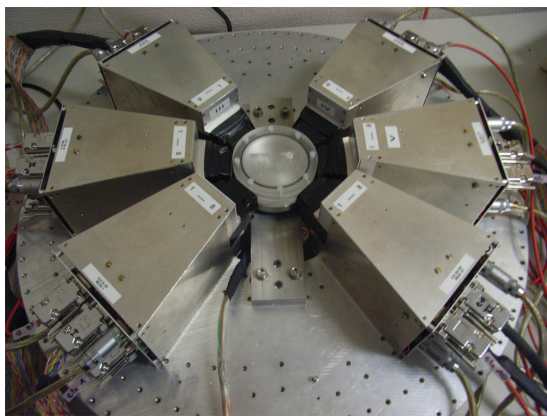
THIS section gives an overview of the small animal PET systems used in this project and concentrates on the most important specifications of the hardware.

5.1 MADPET

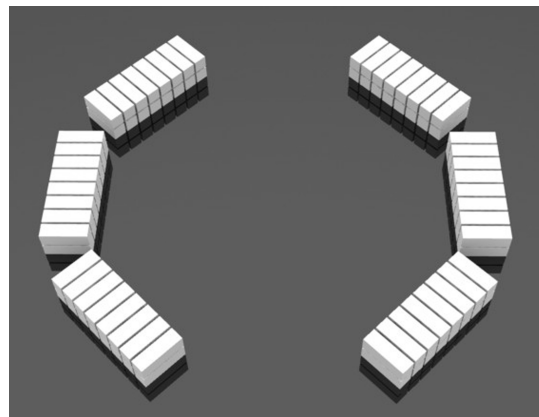
The detector system MADPET is a prototype scanner for small animal PET built in 1996 by the Klinikum rechts der Isar and the Max Planck Institute for Physics [1], [2]. Information about the construction, engineering and development can be found in [3], [4], [5]. Due to the use of APDs as scintillation light detectors, it was called Munich Avalanche Diode Positron Emission Tomograph or short MADPET.

MADPET consists of 6 single layer detector modules arranged in a ring (see figure 5.1). The axial and radial extent of the tomograph are 7.4 cm and 8.6 mm, respectively. Each detector module contains an 2×8 array of APDs (Hamamatsu Photonics) with an active area of $3.0 \times 3.0 \text{ mm}^2$ and a pitch of 4.0 mm as shown in figure 5.2. The whole APD array is covered with a thin layer of epoxy for protection against moisture and mechanical damage.

Because of the relatively low gain of APDs resulting in small pulse heights of the signal,



(a)



(b)

Figure 5.1: (a) Overview of the complete system [6]. (b) Arrangement of the scintillation crystals inside the six detector modules.

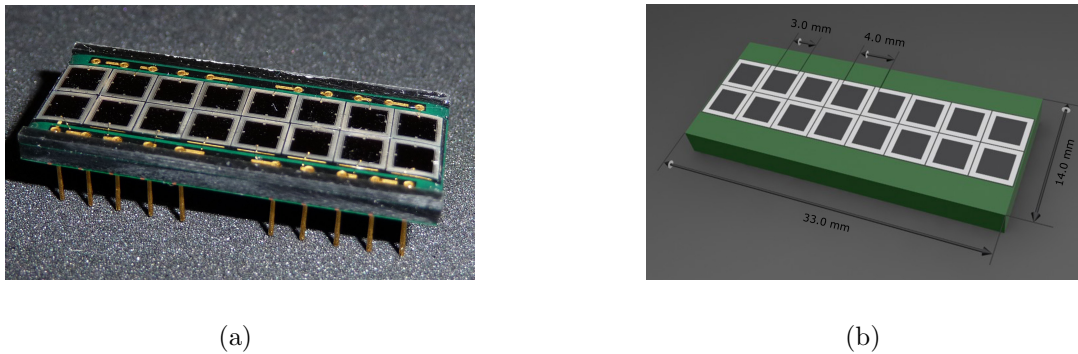


Figure 5.2: (a) Picture and (b) schematic drawing of one 2×8 avalanche photodiode array.

preamplification is done directly after the charge creation with a charge sensitive preamplifier NSLEV (derived from the German expression: Nanosekunden-Ladungsempfindlicher-Vorverstärker). The pulse height after amplification is increased by a factor of 10 [6].

The readout system and data acquisition electronics has recently been refurbished to provide a robust performance. The goal of the refurbishment of MADPET was to build a PET demonstrator for a student's advanced lab course. According to the changed usage the experimental set-up changed as well. Since MADPET is a sector-tomograph not covering a complete ring the detectors were rotated to compensate the missing detector modules. In contrast to its former use as a small animal PET scanner, it is not necessary to rotate the detectors and overcome the problems arising from rotating a rather heavy detector ring and to ensure proper cable handling. Therefore the MADPET ring was arranged in a horizontal position and the scanned objects were rotated instead of the detectors. The signals from each detector channel are processed with three state of the art SADCs (sampling analogue to digital converter). They digitize the analogous detector signals and extract time and amplitude information. A more detailed description of the refurbishment can be found in F.R. Schneider's master thesis [6].

As scintillator material Lutetium Oxyorthosilicate (LSO) has been chosen due to its fast light decay time of 40 ns and high light yield of 32000 optical per absorbed gamma rays with an energy of 1 MeV. The LSO (CTI Inc. now Siemens) crystals with the dimensions of $3.7 \times 3.7 \times 12.0 \text{ mm}^3$ are coupled with one-to-one correspondence to each APD. The 16 LSO crystals are placed in a 2×8 white PTFE matrix. PTFE is an almost perfect diffuse reflecting material in the visible range (reflectivity $R = 98.3\%$). It reduces the optical light crosstalk between neighbouring crystals by preventing photons to scatter from one crystal to the next one. For better optical and mechanical coupling a silicone pad (Wacker SilGel 604, [7]) with a thickness of 0.5 mm is placed between each crystal and APD.

The rotation is done by a stepper motor (Model No. P530 258 004) and an attached planetary gear head (Model No. R40-085.3), both manufactured by Portescap [8]. The gear head is directly coupled to an aluminium table on which the imaged objects can be placed. The stepping motor controller unit was from Isel (Model No. UMS 2G) [9] and can be used together with the data acquisition software.

5.2 MADPET-3

As further development from the MADPET and MADPET-2¹ scanners, a new prototype detector, MADPET-3, based on Silicon Photomultiplier (SiPM) arrays (MPPC, Hamamatsu Photonics) has been constructed. One array has a configuration of 4×4 elements, each element measuring an active area of 1.0 mm^2 with a 1.0 mm pitch in x-direction and a 2.5 mm pitch in y-direction as shown in figure 5.3. One SiPM consists of 400 APDs working in limited Geiger mode.

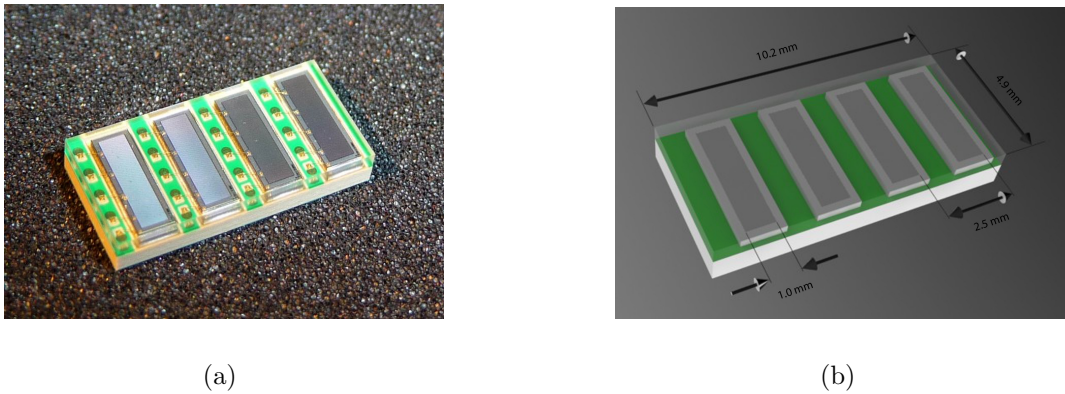


Figure 5.3: (a) Picture and (b) schematic drawing of one 4×8 silicon photomultiplier array.

$1.0 \times 1.0 \times 20.0 \text{ mm}^3$ Lutetium Yttrium Oxyorthosilicate (LYSO) scintillation crystals (Sinocera Inc.) where optically coupled with one-to-one correspondence to each SiPM. The optical coupling between one crystal and the photodetector was achieved by means of UV cured adhesive (Delo-Photobond 400, [11]) with an appropriate refractive index ($n=1.57$) to obtain an efficient light transmission to the entrance window of the SiPM. All surfaces of the crystals are polished. In order to optimize the light collection, the LYSO crystals are covered with a highly reflecting layer of barium sulphate. The whole LYSO crystal array including the barium sulphate layer has been built by Sinocera [12] (figure 5.4).

The relatively large pitch of 2.5 mm in y-direction allows to combine two of those SiPM arrays to one detector module with an individual SiPM detector readout of 16 detectors on the top side and 16 detectors on the bottom side. A custom-built holder made of photopolymer resin is used to assure proper alignment of the crystal array to two SiPM arrays. Figure 5.5 shows the experimental set-up for one detector module except for the resin holder.

The MADPET-3 demonstrator consists of two of those detector modules. In order to perform measurements simulating a complete detector ring the scanned object has to be rotated in similar way as for the MADPET system with the same stepper motor. Due to the size of the readout board for data acquisition the two SiPM detector module are arranged at a distance of 10.0 cm as shown in figure 5.6. The rotation is performed in 15° steps resulting in a virtual detector ring with 24 detector modules and a diameter of 45

¹MADPET-2 is the direct successor model of MADPET. It is also based on APDs and individual readout by LSO crystals. A more detailed description about MADPET-2 can be found in [10]. MADPET-2 is not an object of this work and mentioned merely for completeness.

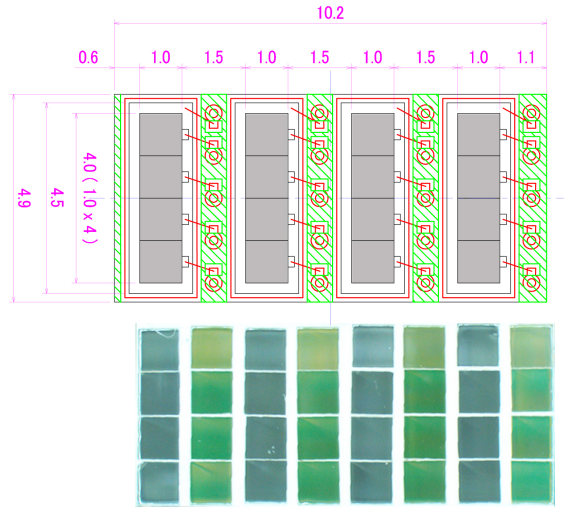
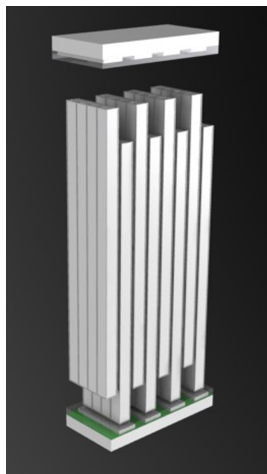
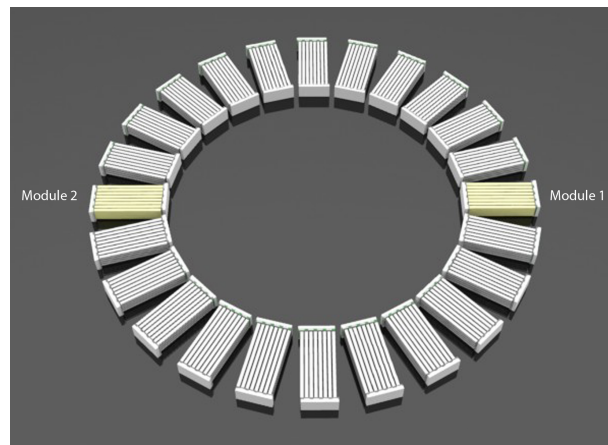


Figure 5.4: Top: Drawing of one SiPM array with in total 16 channels of 1.0×1.0 mm² pixels arranged in 1×4 SiPM sub-arrays. All dimensions of the SiPM array are given in mm. Every second row of the LYSO crystal array is read out by one SiPM array. Bottom: LYSO crystal array composed of $1.0 \times 1.0 \times 20.0$ mm³ single crystals and BaSO₄ reflector in between them.



(a)



(b)

Figure 5.5: (a) Detector module consisting of two SiPM arrays with alternating front and back side readout and 32 LYSO scintillation crystals. (b) Schematic drawing of the whole MADPET-3 system consisting of two detector module (marked in yellow) and the 22 missing detector modules which will be replaced by rotating the two opposite modules.

mm as indicated in figure 5.5 (b). For data acquisition the same readout system as for MADPET is used for MADPET-3. Only slight modifications in the power supply for the SADCs are done and no additional preamplification is needed for the SiPMs.

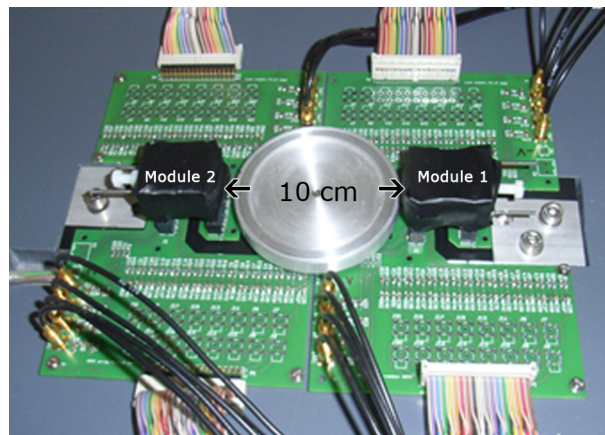


Figure 5.6: Photograph of MADPET-3 consisting of two SiPM detector modules. The detector modules are covered with several layers of black tape to avoid light from the surrounding environment reaching the SiPMs [13].

References

- [1] Nuklearmedizinische Klinik und Poliklinik, Klinikum rechts der Isar der Technischen Universität München, Ismaninger Str. 22, 81675 München, Munich, Germany, <http://www.nuk.med.tu-muenchen.de/>
- [2] Max-Planck-Gesellschaft zur Förderung der Wissenschaften e.V., Hofgartenstr. 8, 80539 München, Munich, Germany, <http://www.mpg.de/>
- [3] S.I. ZIEGLER, B.J. PICHLER, G. BOENING, M. RAFECAS, W. PIMPEL, E. LORENZ, N. SCHMITZ, AND M. SCHWAIGER, *A Prototype High-resolution Animal Positron Tomograph with Avalanche Photodiode Arrays and LSO-Crystals*, Eur. J. Nucl. Med. Mol. Img., 28(2), pp. 136-143, 2001
- [4] B. J. PICHLER, *Untersuchung der Detektoreigenschaften von Lutetium-Oxyorthosilikat-Szintillationskristallen und Lawinen-Photodioden für die hochauflösende Positronen-Emissions-Tomographie*, Diploma Thesis in Electrical Engineering and Communication, Technische Universität München, Munich, Germany, 1996
- [5] B. J. PICHLER, *Entwicklung eines Detektors für die hochauflösende Positronen-Emissions-Tomographie basierend auf Lutetium-Oxyorthosilikat-Szintillatoren, Lawinen-Photodioden-Matrizen, integrierter Elektronik und Doppellagensauslese*, PhD Thesis in Physics, Technische Universität München, Munich, Germany, 2001
- [6] F. R. SCHNEIDER, *Setup and Commissioning of a Positron Emission Tomograph for a Student's Advanced Laboratory Course*, Master Thesis in Engineering Physics, Technische Universität München, Munich, Germany, 2009
- [7] Wacker Chemie AG, <http://www.wacker.com/>
- [8] Portescap, <http://www.portescap.com/>
- [9] Isel Germany AG, <http://www.isel.com/>
- [10] V. C. SPANOUDAKI, *Development and Performance Studies of a Small Animal Positron Emission Tomograph with Individual Crystal Readout and Depth of Interaction Information and Studies of Novel Detector Technologies in Medical Imaging*, PhD Thesis in Physics, Technische Universität München, Munich, Germany, 2008
- [11] DELO Industrie Klebstoffe, Delo PHOTOBOND 400 Data sheet, <http://www.delo.de/>
- [12] Sinocera Inc., <http://www.sinocera.net/>
- [13] F. R. SCHNEIDER ET AL., *Erste Leistungsstudien eines Prototyp-PET-Scanners für kombiniertes PET/MR basierend auf G-APDs*, DGN Conference, oral presentation, Bregenz, Germany, 2011

Chapter 6

System Matrix

ITERATIVE reconstruction algorithms require the computation of the system matrix \mathbf{H} , which represents the imaging process. This chapter is dedicated to show how the system matrix can be built by means of different techniques such as computation based on analytical models, Monte Carlo simulations and calculation by a set of point source measurements over the whole FOV. The comparison of these generated SMs is presented for the MADPET scanner. The comparison in terms of image quality was done using the iterative reconstruction algorithm ML-EM.

As the elements of the system matrix p_{ij} represent the probability to detect an annihilation event emitted from the voxel j by the LOR i defined by the detector pair i , this probability depends on many factors:

- ◇ solid angle subtended by the detector pair
- ◇ range of the positron
- ◇ non-collinearity of the annihilation photons
- ◇ scattering and attenuation of photons in the object to image
- ◇ scattering of photons in the detector ring
- ◇ efficiency of the scintillation crystals
- ◇ dead space in the detector ring
- ◇ ...

In order to include all involved effects the system matrix becomes quite huge and complex. The system matrix may be factorizing in to several components that account for different physical effects that have to be considered [1], [2]. A decomposition can be done as the following:

$$\mathbf{H} = \mathbf{H}(\text{detector})\mathbf{H}(\text{object})\mathbf{H}(\text{geometry})\mathbf{H}(\text{positron}) \quad (6.1)$$

Here $\mathbf{H}(\text{object})$ is a diagonal matrix containing all the attenuation factors of the imaged object. $\mathbf{H}(\text{positron})$ is including positron range and angular separation effects related to the radio-isotope used. $\mathbf{H}(\text{detector})$ and $\mathbf{H}(\text{geometry})$ depend directly on the

scanner. $\mathbf{H}(\text{geometry})$ implies the geometric detection probabilities determined by the intersection of image voxels with the volume of response between detector pairs. The term $\mathbf{H}(\text{detector})$ can be construed as a normalization matrix ensuring that all LORs or detector pairs produce the same response to a given number of annihilation events [3], but it also includes other blurring factors such as scatter events in the scintillation crystal. In the case of small animal PET scanners with a small diameter of the transaxial FOV, the effect of non-collinearity of the two annihilation photons is negligible. The resolution loss for MADPET would be 0.002 mm. The positron range for ^{18}F labelled radio-isotopes is in a submillimeter region in tissue. Therefore, $\mathbf{H}(\text{positron})$ will be set equal to the identity matrix in the following.

6.1 System Matrix based on the Analytical Detector Response Function Model

After the decomposition of the SM according to equation 6.1 it is possible to calculate analytical some components of the SM. Especially the geometrical component $\mathbf{H}(\text{geometry})$ of the SM can be computed with an analytical model of the PET detector response function (DRF). The DRF model is a further development of those previously proposed in the literature [4],[5],[6]. It is based on a set of equations describing the probabilities of the detection processes that take place during the acquisition. While these equations can generally not be solved analytically, they can be implemented into a multi-stage algorithm allowing the estimation of the detection efficiency for any crystal pair. The basic equations of this model are presented below accordingly to [4], and some elements of their implementation are described in the next section.

6.1.1 Theory

Given a reference frame (O, x, y, z) attached to the scanner (figure 6.1), where O is the center of the FOV, (O, z) is the scanner axis and (O, x, y) is the central plane of the scanner. An arbitrary direction may be described either by a normalized vector or by its spherical coordinates (θ, φ) , where $\theta \in [0, 2\pi]$ is the in-plane angle and $\varphi \in [0, \pi]$ is the out-of-plane angle made with the scanner axis. According to figure 6.2 a flux of photons is considered which is emitted by a point source M along a direction \mathbf{n} and reaching a crystal c . The probability $p_c(M, \mathbf{n})$ of detecting these photons is assumed to be equal to the attenuation of the flux by the crystal c :

$$p_c(M, \mathbf{n}) = \{1 - \exp[-\mu_c L_c(M, \mathbf{n})]\} A_c(M, \mathbf{n}) \quad (6.2)$$

where μ_c is the total crystal attenuation coefficient, L_c is the path length of the photon flux across the crystal and A_c represents the attenuation of the photons prior to entering crystal c . The attenuation term A_c can be computed by taking into account each component of the scanner traversed prior to detection in crystal c :

$$A_c(M, \mathbf{n}) = \exp\left[-\sum_i \mu_i L_i(M, \mathbf{n})\right] \quad (6.3)$$

where μ_i is the total attenuation coefficient and L_i the corresponding path length of

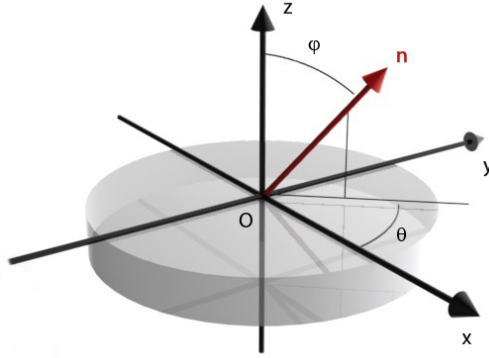


Figure 6.1: Reference frame (O,x,y,z) used for the analytical model (illustration according to [4]).

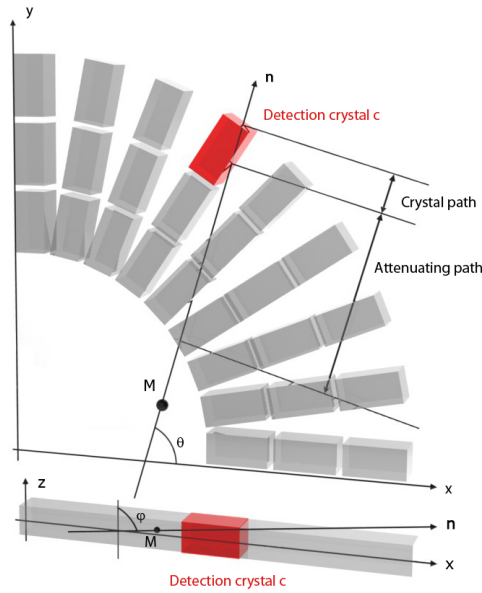


Figure 6.2: Simplified transverse (top) and lateral (bottom) view of the elements for the analytical model (illustration according to [4]).

the photons in the i th component.

Neglecting deviation effects, each photon emitted at a point M moving along \mathbf{n} is paired with an opposite photon emitted along $(-\mathbf{n})$. Therefore the probability of coincident detection $p_{cd}(M, \mathbf{n})$ by a crystal pair (c, d) equals the product of the detection probabilities for the crystals c and d , respectively:

$$p_{cd}(M, \mathbf{n}) = p_c(M, \mathbf{n})p_d(M, -\mathbf{n}) \quad (6.4)$$

Consequently, the total detection efficiency $\varepsilon_{cd}(M)$ for the crystal pair (c, d) , is computed by integrating over all possible directions $\mathbf{n}(\theta, \varphi)$:

$$\varepsilon_{cd}(M) = \frac{1}{4\pi} \int_0^{2\pi} \int_0^\pi p_{cd}(M, \theta, \varphi) \sin\varphi d\varphi d\theta \quad (6.5)$$

Computation of this integral may be broken into two steps in order to separate in-plane effects from axial effects:

$$\varepsilon_{cd}(M) = \frac{1}{2\pi} \int_0^{2\pi} p_{cd}(M, \theta, 0) \alpha_{cd}(M, \theta) d\theta \quad (6.6)$$

with

$$\alpha_{cd}(M, \theta) = \frac{\frac{1}{2} \int_0^\pi p_{cd}(M, \theta, \varphi) \sin\varphi d\varphi}{p_{cd}(M, \theta, 0)} \quad (6.7)$$

In these terms, $p_{cd}(M, \theta, 0)$ describes the detection probability of photons emitted with an arbitrary in-plane angle θ with a zero out-of-plane angle φ . Equation (6.5) gives the total detection efficiency for the crystal pair (c, d) as one single integral of the probability $p_{cd}(M, \theta, 0)$, multiplied by an axial efficiency factor $\alpha_{cd}(M, \theta)$. In a fully three-dimensional simulation, this factor will be calculated using the integral equation (6.6). If only a 2D model is considered all out-of-plane effects could be neglected and equation (6.6) reduces to:

$$\varepsilon_{cd}(M) = \frac{1}{2\pi} \int_0^{2\pi} p_{cd}(M, \theta, 0) d\theta \quad (6.8)$$

6.1.2 Implementation

Intersection Test

The goal of the DRF implementation is to calculate the system matrix entries for arbitrary PET scanner geometries. It provides a method to determine for a given voxel with the center M and given LOR, both specified by a unique number and a crystal pair (c, d) the corresponding probability ε_{cd} . This detection probability will be denoted as the term 'weight' in the following paragraphs. In the current approach of the DRF model different scanner geometries can be applied with only a few limitations for the specified geometries. The scintillation crystals can only be assumed as cuboids for example. More details about how a specific scanner geometry has to be defined can be found in [7].

In order to calculate the weight for a certain voxel and a given crystal pair (c, d) all the intersection lengths from a ray at the center of a voxel intersecting both crystals have to be determined. For this purpose a slab-intersection test [8], [9] is applied. A slab-intersection test allows to calculate the intersection points between an object and a ray passing through it. The intersection method developed by [10] requires a bounding box that surrounds all the primitives of the object. This box is then used to determine if a ray doesn't intersect any of the primitives and if the ray misses the box, it must also miss all of the primitives inside the box. For the particular case of the DRF model the scintillation crystal represents the bounding box and the photon the intersecting ray. One way to generate a bounding box is as an intersection of three slabs, where a slab is the region of space between two parallel planes. To intersect a ray against the bounding box, the ray intersects each of the box's three slabs in turn. All three slabs are aligned with the three coordinate axes of the crystal as indicated in figure 6.3. For reasons of clarity the slabs are drawn only in 2D.

The basic ray-bounding box intersection algorithm works as follows [12]: First a certain

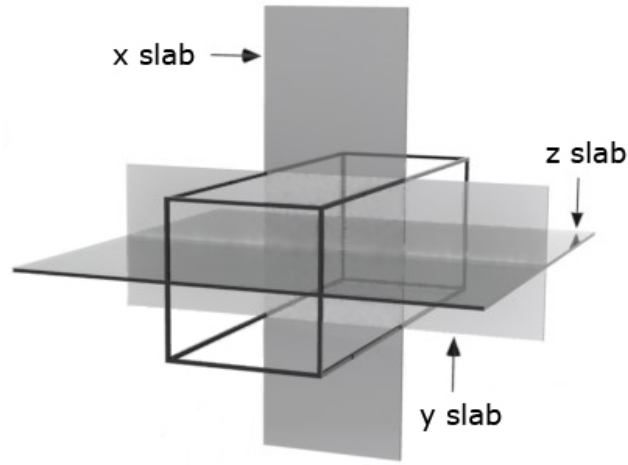


Figure 6.3: Scintillation crystal as bounding box with the three intersecting slabs. For reasons of clarity the slabs are drawn only in 2D.

parametric interval that covers a range of positions t along the ray is defined. In the next step the entry and exit point t_{i1} and $t_{i2} \forall i \in x, y, z$ will be calculated where the ray intersects each slab. Figure 6.4 illustrates this process in the xy plane. The ray $r_1(t)$ intersects the x and y slabs in four points: t_{x1}, t_{x2}, t_{y1} and t_{y2} . From these t -values the maximum and minimum t -values t_{min} and t_{max} are computed, representing the entry and exit point of the bounding box:

$$t_{min} = \max(t_{x1}, t_{y1}, t_{z1}) \quad (6.9)$$

$$t_{max} = \min(t_{x2}, t_{y2}, t_{z2}) \quad (6.10)$$

In a final step it has to be tested, if $t_{min} > 0$ and $t_{max} > 0$ to ensure that the intersection test is orientation dependent and if $t_{min} < t_{max}$. Otherwise the ray would miss the bounding box as depicted in figure 6.4 for the second ray $r_2(t)$. The intersection length l is finally computed by $l = t_{max} - t_{min}$.

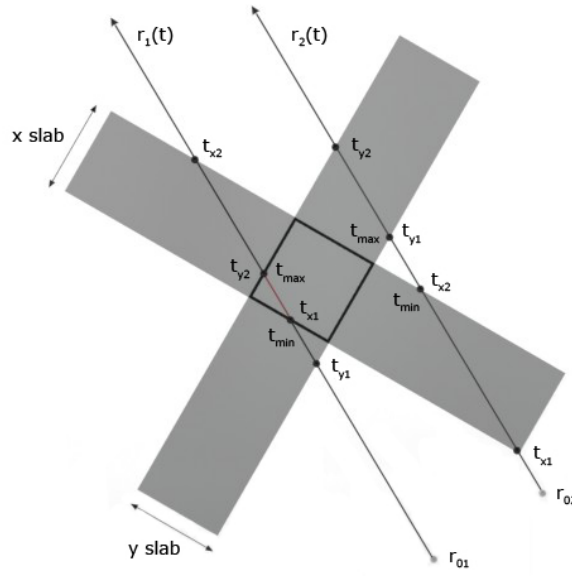


Figure 6.4: Bounding box formed by two slabs in the xy plane. t -values are shown for two rays $r_1(t)$ and $r_2(t)$ where $r_1(t)$ intersects the bounding box $t_{min} < t_{max}$, whereas $r_2(t)$ does not $t_{min} < t_{max}$ [11].

Attenuation and Weight Calculation

For each computation of $p_{cd}(M, n)$, the attenuation of all the rays traversing crystals before entering the crystal pair (c,d) has to be calculated in addition. To avoid the costly search of crystal candidates every time a $p_{cd}(M, n)$ calculation is computed a list of possible attenuation crystals for each LOR is created.

In the 2D implementation as described in [4] the angular aperture range α_θ is calculated first, which represents the span of angles under which a source could be seen by both detectors. One emission angle step $\Delta\theta$ is then computed as a fraction N of this aperture (figure 6.5). The detection efficiency for a crystal pair is then computed as the sum of the detection probabilities $p_{cd}(M, N\Delta\theta)$ for the emission angles $N\Delta\theta$ that are integer multiples of the angular step $\Delta\theta$. N is a parameter which indicates the precision of the integral calculation, since the more evaluation steps are used for the integral calculation, the more precise is the integral value. The number of angular steps N that have to be applied also depends on the geometry of the scintillation crystals. As indicated in figure 6.5 on the right side more angular steps are needed for crystals at the edge. This effect at the edge will be more distinctive e.g. for long, narrow crystals.

In the 3D implementation angular aperture range has to be defined by two aperture angles α_θ and α_φ as indicated in figure 6.6. The calculation of both aperture angles according to the borders of the crystal would result in a time-consuming computation. Therefore the aperture ranges for α_θ and α_φ are set to be equal and denoted as α_c . For this purpose every crystal is entirely enclosed through a bounding sphere, where α_c is given by twice the angle between the ray pointing to the crystal center and a tangent of its bounding sphere, both starting from the voxel center M :

$$\alpha_c = 2 \cdot \arcsin \left(\frac{r_c}{|\mathbf{v}_c|} \right) \quad (6.11)$$

where \mathbf{v}_c represents the direction vector from the voxel center to the center of the respective crystal and r_c the radius of the bounding sphere.

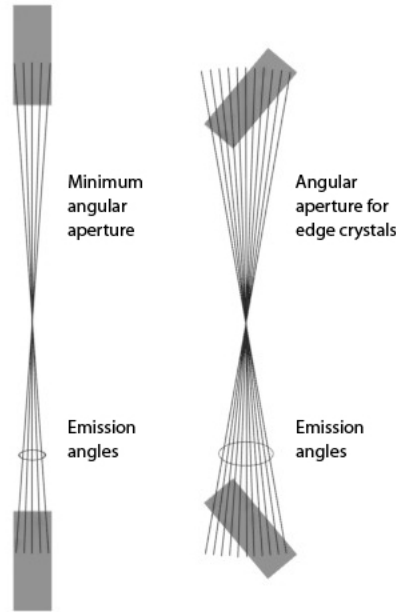


Figure 6.5: Angular apertures and sets of emission angles for crystal pairs near the centre (left) and edge (right) of the FOV [4].

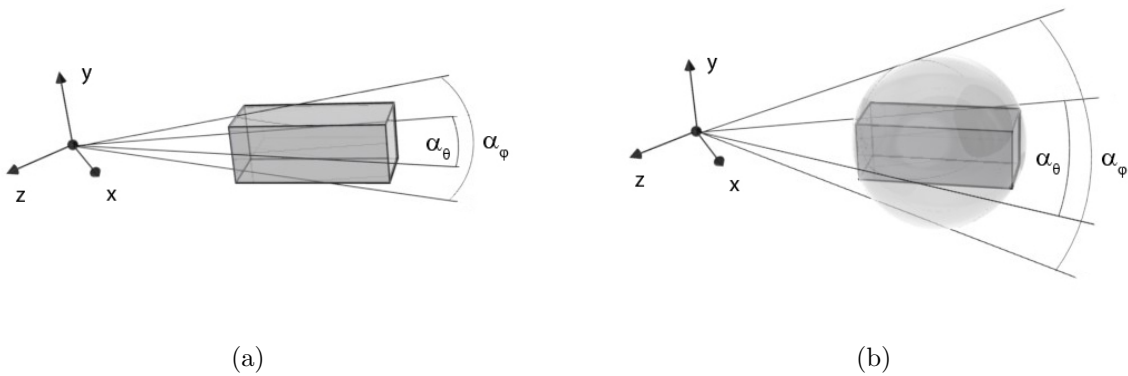


Figure 6.6: Angular aperture range using different approaches: (a) Angular aperture of one crystal defined by α_θ and α_ϕ . (b) Angular aperture of the bounding sphere for one crystal defined by $\alpha_\theta = \alpha_c = \alpha_\phi$ [7].

Considering the fact that the angular aperture range for rays starting at M can be calculated for both crystals (c,d) forming a LOR, which results in α_c and α_d , one has to decide which one of these two angular aperture angles is to be used for further processing. The smaller one has to be chosen as this would lead to smaller angular step sizes and therefore to more rays intersecting both crystals. Once the angular aperture is defined, evaluations points α_Δ for the calculation of the system matrix weights ϵ_{cd} can be generated as shown in figure 6.7:

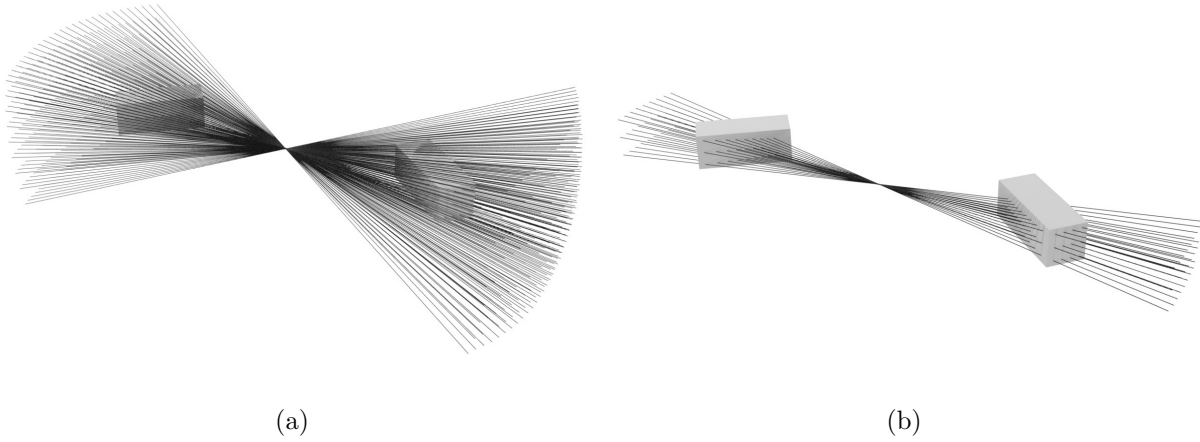


Figure 6.7: Generated evaluation points shown as rays emitted from one voxel: (a) All evaluation rays used for the weight calculation of one voxel (b) Evaluation rays that hit both crystals actually contributing to the matrix weight [7].

$$\alpha_{\Delta} = \frac{\alpha_c}{N} \quad (6.12)$$

Based on the spherical coordinates of the center evaluation point $(\theta_{v_c}, \varphi_{v_c})$ the directions d_{ij} of all evaluation points will be created according to:

$$d_{ij} = (\theta_i, \varphi_j) = (\theta_{v_c} + i \cdot \alpha_{\Delta}, \varphi_{v_c} + j \cdot \alpha_{\Delta}) \text{ where } i, j \in \left[-\frac{N}{2}, \frac{N}{2} \right] \quad (6.13)$$

In a final step all the created evaluation points are used to approximate the integral in equation (6.4):

$$\varepsilon_{cd}(M) = \sum_{i, j = -\frac{N}{2}}^{\frac{N}{2}} p_{cd}(M, \theta_i, \varphi_j) \sin(\varphi_i) \alpha_{\Delta}^2 \quad (6.14)$$

6.2 Monte Carlo based System Matrix

Monte Carlo simulations allow to obtain a realistic and complete response of a system, even before it was built, providing a way to modify and optimize certain features of interest. Due to the random process involved in a MC simulation the matrix elements are affected by statical noise. This effect of noise propagation into the image from the element of a SM can be reduced by increasing the number of simulated events per image voxel [13]. As the results are based on a computer model, the accuracy of the results will depend on the accuracy of the underlying model. GATE is the simulation code employed in this work and there are several publications that validate the model on which it is based on [14], [15], [16], [17], [18], [19], [20].

By using MC simulations to generate the SM, the factors that account for the geometry of the scanner, the scatted events in the detector modules $\mathbf{H}(\text{geometry})$ and partial

$\mathbf{H}(\text{detector})$ are included in the SM. The normalization matrix implied in $\mathbf{P}(\text{detector})$ is also studied in chapter 7.2 and its coefficients are taken from additional measurements.

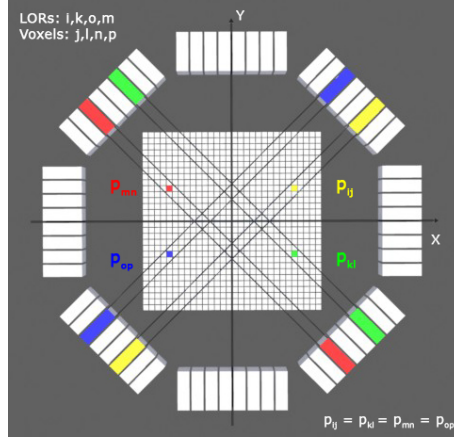


Figure 6.8: Symmetries in MADPET for Cartesian voxelized FOV.

The FOV is subdivided in $30 \times 30 \times 1$ cubic voxels of $1.85 \times 1.85 \times 1.85 \text{ mm}^3$ volume. An individual simulation for 1/4 of the voxels is performed to generate the SM. This reduced number of voxels is sufficient by exploiting certain symmetries. Considering the central transaxial plane as show in figure 6.8, the matrix weight p_{ij} for voxel j and the corresponding LOR i has the value as the matrix weight p_{kl} for voxel l and LOR k after reflection about the y axis. These matrix weights can also be reflected about the x axis to obtain p_{mn} and p_{op} . Four additional identical values can be found after reflection about the axial x - y plane. In total only 225 simulations are necessary to obtain all the elements of the SM. For each simulation 4 million annihilation events were created. This number was chosen in order to obtain a high statistical count rate and to generate the SM in a reasonable computing time. The simulated data were sorted in time, sorted into coincidences and the symmetries as described before were applied. The time necessary for these simulations and the following data processing was three weeks.

6.3 Measurement of the System Matrix

An other way of calculation the SM can be done by a set of point source measurements for each image voxel over the whole FOV. This approach has the great advantage that it includes all possible physical effects as described in equation (3.1), except for the attenuation correction $\mathbf{H}(\text{object})$ related to the imaged object. A simplified approach of measuring the SM was performed by [21], making a reduced number of point source measurements and extracting the acquired data in an elaborate way for the complete SM. An extension to fully 3D PET was accomplished by [22]. In this work a similar approach as described in [22] was used for the generation of the SM for MADPET.

A cylindrical ^{22}Na source (Model MMSO4, Eckert und Ziegler, [29]) with a diameter of 1.0 mm and a length of 0.5 mm with an activity of 3.7 MBq was used for the measurements. The ^{22}Na source is embedded in a small capsule of $3 \times 3 \times 8 \text{ mm}^3$ clear acrylic with a Delrin plug. The availability of high activity concentration in a small volume makes the ^{22}Na source an ideal choice to achieve good counting statistics in a short measurement time.

The long half-life of ^{22}Na allows scanning all point source positions without replacing the source. Fig. 6.9 shows the high precision positioning device (F9S-3-M, Walter Uhl, [30]). This device allows movement of the point source along three orthogonal axes with resolutions up to 0.0001 mm. The F9S-3-M can be operated as a stand-alone unit with a joystick or it can be controlled by a PC through an RS 232 serial interface. For this purpose a C++ Code has been written to control the stepping motor through the RS 232 serial interface.

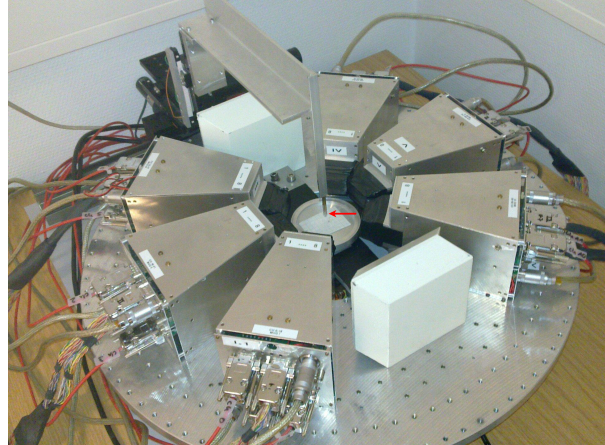


Figure 6.9: Assembled high precision positioning device with holder for the ^{22}Na source. The red arrow marks the position of the point source.

The stepping motor is first aligned with respect to the scanner axes. The alignment process is based on processing data when the point source travels over distances in the FOV. The point source was first moved across the axial FOV along the z axis for several positions and data were taken for 10 seconds. The acquired data were sorted in time, sorted in coincidences and finally reconstructed with an ML-EM algorithm based on a pre-calculated SM with the DRF model as described before. On the reconstructed images a Gaussian fit was applied, whose peak position was used to find the center plane in the axial FOV. The alignment in the transverse plane is again done by processing data for several point source positions. The point source was moved along two diagonal lines where the diagonal brace determines the center of the transverse plane as show in figure 6.10

The FOV is discretized in $30 \times 30 \times 1$ cubic voxels of $1.85 \times 1.85 \times 1.85 \text{ mm}^3$ volume and centred at the middle of the scanner. The point source was positioned according to this Cartesian grid resulting in 900 measurement positions. As MADPET is a sector tomograph not covering a complete ring with detectors it is necessary to rotate the detector modules or in this case the voxel grid in 8 steps by an angle of 45° to account for the missing projection angles. All those rotation steps taken together represent a full detector ring with 8 detector modules. Fortunately, it is not necessary to perform 8 different measurements as one could take advantage of certain symmetries which are implicit in those rotations. One scanned source position and one specific LOR in the initial voxel grid position (rotation angle 0°) corresponds to the information for the rotation by an angle of 180° . Figure 6.11 clarifies this issue for one arbitrarily chosen voxel and LOR. For example the blue marked voxel in figure 6.11(b) and the corresponding LOR between detector module no.I, crystal no.V and detector module no.IV, crystal no.II contains also

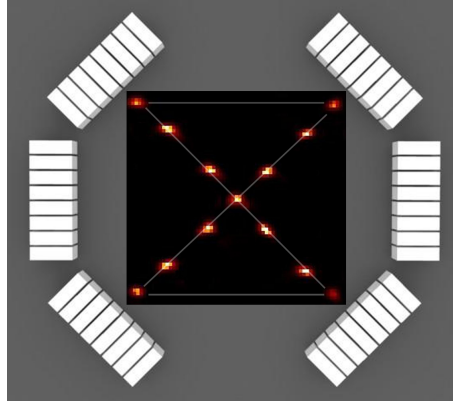


Figure 6.10: Alignment of the stepping motor according to the scanner axes in the transverse plane. The image shows the fusion of all the reconstructed point source positions. Reconstruction was done with an ML-EM algorithm based on a pre-calculated SM with the DRF model.

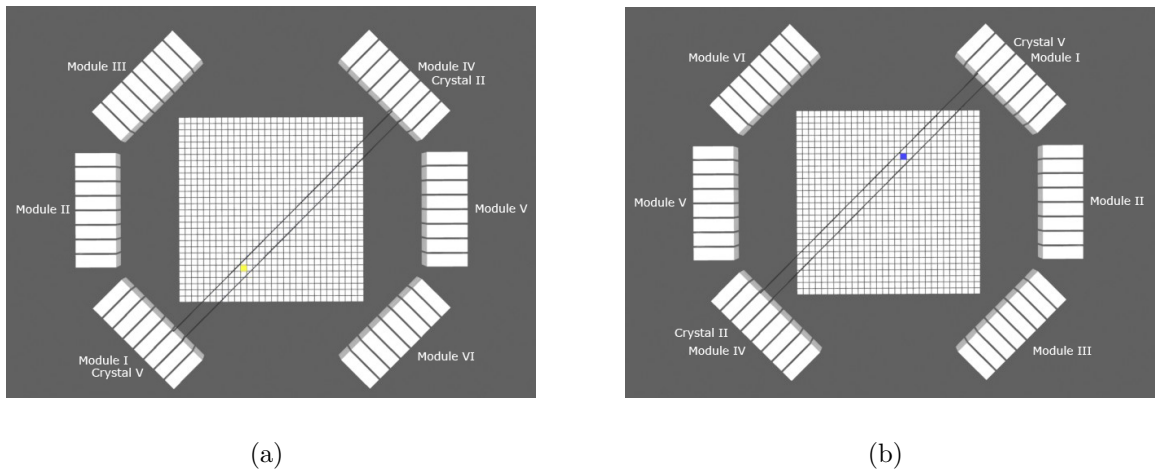


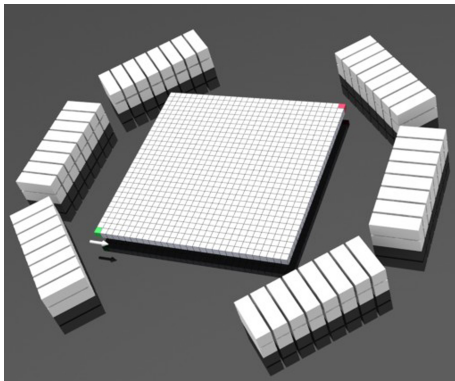
Figure 6.11: (a) Initial module position (b) Rotated module position of 180° : The blue marked voxel contains also information for the yellow marked voxel (The picture shows the rotation of the hardware components not of the voxel grid).

information for the yellow marked voxel in figure 6.11(a). For simplification figure 6.11(b) shows the 180° rotation of the hardware components and not the voxel grid. The same symmetries as for the 0° and 180° rotation are applied for the rotations steps 45° - 225° , 90° - 270° and 135° - 310° . Therefore, measurements have to be performed only for rotation steps of 45° , 90° and 135° to account for the missing projection angles as visualized in figure 6.12. In total 3600 measurements are accomplished.

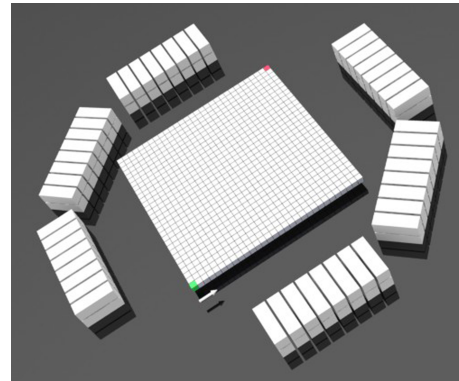
As the gain of the APD detectors and also the light output of the scintillation crystals are temperature dependent, the relation between the detected photon energy and the amplitude of the measured signal is not constant [23]. Additionally the APD detector channels have slightly different signal properties like rise time and propagation delay values caused by unmatched cable lengths or preamplifier variations. Therefore it is essential that the detector system is calibrated to ensure operation under well defined environment conditions. A complete description of the calibration protocol for MADPET can be found in [24] and [25], which has been applied for each measured voxel and point

source position.

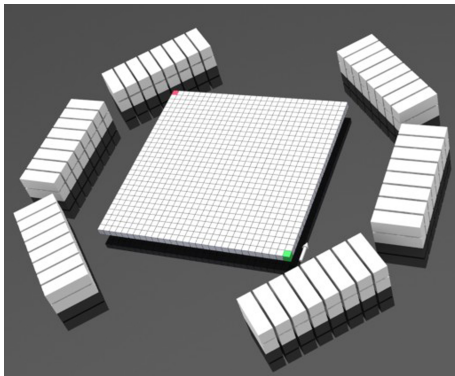
For each point source position projection data have been obtained and stored in a binary file format allowing maximum flexibility in further data processing. For data analysis the ROOT framework developed by CERN is used [26], [27]. After applying the energy and time calibration, the projection data were stored in a ROOT tree file format similar to the ones supported by the software GATE and GEANT4 allowing an ideal subsequent comparison between the different methods for the generation of the SM. First the rotation steps and symmetries as described in figure 6.12 and figure 6.11 were applied for each voxel, then all the detected events were sorted in time and finally sorted into coincidences. Since there were no scattering media except the small capsule of the ^{22}Na source, the recorded data were assumed to be unscattered true events. The data were acquired for 40 seconds per source position, so the total acquisition time took about 20 days and resulted in about 2 TB data. For data analysis and storage an 8-way AMD Opteron cluster provided by the Leibniz-Rechenzentrum (LRZ) [28] was used. The LRZ Linux Cluster offers a flexible usage due to various available memory sizes and parallelization by message passing (MPI) which is essential especially for a fast image reconstruction.



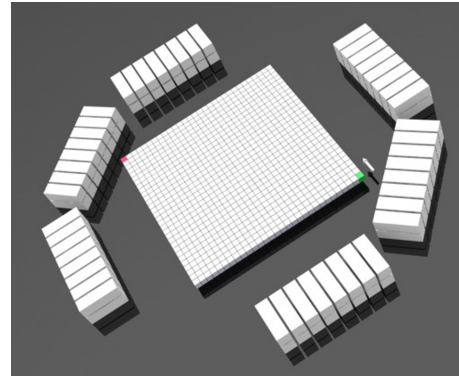
(a) Voxel grid at 0°



(b) Voxel grid at 45°



(c) Voxel grid at 90°



(d) Voxel grid at 135°

Figure 6.12: Voxel grid at different angles. The green voxel indicates the start position and the red voxel the last measurement position. The white arrow assigns the measurement direction.

References

- [1] E.U. MUMCOUGLU , R.M. LEAHY, S.R. CHERRY, *Bayesian reconstruction of PET images: methods and performance analysis*, Phys. Med. Biol., vol. 41, pp. 1777-1807, 1996
- [2] J. QUI, R.M. LEAHY, S.R. CHERRY, A. CHATZIOANNOU, T.H. FARQUHAR, *High resolution 3D Bayesian image reconstruction using the microPET small animal scanner*, Phys. Med. Biol., vol. 43, pp. 1001-1023, 1998
- [3] T.R. OAKES, V. SOSSI, T.J. RUTH, *Normalization for 3D PET with a low-scatter planar source and measured geometric factors*, Phys. Med. Biol., vol. 43, pp. 961-972, 1998
- [4] D. STRUL, R.B. SLATES, M. DAHLBOM, S.R. CHERRY, AND P.K. MARDSEN, *An improved analytical detector response function model for multilayer small animal PET scanners*, Phys. Med. Biol., vol. 48, pp. 979-994, 2003
- [5] R. LECOMTE, D. SCHMITT, AND G. LAMOUREUX, *Geometry study of high-resolution PET detection system using small detectors*, IEEE Trans. Nucl. Sci, vol. 31, pp. 556-561, 1984
- [6] D. SCHMITT, B. KARUTA, C. CARRIER, AND R. LECOMTE, *Fast point spread function computation from aperture functions in high-resolution positron emission tomography*, IEEE Trans. Med. Img., vol. 7, pp. 2-12, 1988
- [7] P. PEDRON, *Implementation of an analytical 3D model for generation the system matrix of a PET scanner*, Bachelor Thesis in Informatics, Technische Universität München, 2009
- [8] T. AKENINE-MÖLLER, E. HAINES, AND N. HOFFMAN, *Real-Time Rendering 2nd Edition*, A.K. Peters, Ltd., Natick, MA, USA, 2002
- [9] E. HAINES, P. HANRAHAN, R.L. COOK, J. ARVO, D. KIRK, P.S. ECKERT, A.S. GLASSNER *An Introduction to Ray Tracing*, A.S. Glassner, ed, Academic Press Limited, ISBN 0-12-286160-4, 1989
- [10] T.L. KAY, AND J.T. KAJIYA *Ray Tracing Complex Scenes*, Computer Graphics, 20(4), pp. 269-78, 1986
- [11] ACM SIGGRAPH, *Association for Computing Machinery's Special Interest Group on Graphics and Interactive Techniques*, <http://www.siggraph.org/education/materials/HyperGraph/raytrace/rtinter3.htm>
- [12] M. PHARR, AND G. HUMPHREYS *Physically Based Rendering - From Theory to Implementation*, Morgan Kaufmann, 2nd edition, ISBN-13 978-0123750792, 2010
- [13] M. RAFECAS, G. BÖNING, B.J. PICHLER, E. LORENZ, M. SCHWAIGER, S.I. ZIEGLER, *Effect of Noise in the Probability Matrix Used for Statistical Reconstruction of PET Data*, IEEE Trans. Nucl. Sci., vol. 51, pp. 149-156, 2004

-
- [14] S. JAN, C. COMAT, D. STRUL, G. SANTIN, R. TRÉBOSSSEN, *Monte Carlo simulation for the ECAT EXACT HR+ system using GATE*, IEEE Trans. Nucl. Sci., vol. 52, pp. 627-633, 2005
- [15] F. BATAILLE, C. COMAT, S. JAN, R. TRÉBOSSSEN, *Monte Carlo simulation for the ECAT EXACT HRRT using GATE*, IEEE NSS MIC Conf. Rec. 4, pp. 2570-2574, 2004
- [16] C. MICHEL, L. ERIKSSON, H. ROTHFUSS, B. BENDRIEM, D. LAZARO, I. BUVAT, *Influence of crystal material on the performance of the HiRez 3D PET scanner: A Monte Carlo study*, IEEE NSS MIC Conf. Rec. 4, pp. 1528-1531, 2006
- [17] F. LAMARE, A. TURZO, Y. BIZAIS, C.C. LE REST, D. VISVIKIS, *Validation of a Monte Carlo simulation of the Philips Allegro/GEMINI PET systems using GATE*, Phys. Med. Biol., vol. 51, pp. 943-962, 2006
- [18] C.R. SCHMIDTLEIN, A.S. KIROV, L.M. BIDAUT, S.A. NEHMEH, Y.E. ERDI, A. GANIN, C.W. STEARNS, D.L. MCDANIEL, K.A. HAMACHER, J.L. HUMM, H.I. AMOLS, *Validation of GATE Monte Carlo simulations of the GE Advance/Discovery LS PET scanner*, Med. Phys., vol. 33, pp. 198-208, 2006
- [19] S. JAN, A. DÉESBRE, F. PAIN, D. GUEZ, C. COMAT, H. GURDEN, S. KERHOAS, P. LANIÈCE, F. LEFEBVRE, R. MASTRIPPOLITO, R. TRÉBOSSSEN, *Monte Carlo simulation of the microPET FOCUS system for small rodents imaging applications*, IEEE NSS MIC Conf. Rec. 3, pp. 1653-1657, 2005
- [20] C. MERHEB, S. NICOL, Y. PETEGNIEF, J.N. TALBOT, I. BUVAT, *Assessment of the Mosaic animal PET system response using list-mode data for validation of GATE Monte Carlo modelling*, Nucl. Instr. Methods A A569, pp. 220-224, 2006
- [21] V.Y. PANIN, F. KEHREN, H. ROTHFUSS, D. HU, C. MICHEL, M.E. CASEY, *PET reconstruction with system matrix derived from point source measurements*, IEEE Trans. Nucl. Sci., vol. 53, pp. 152-159, 2006
- [22] V.Y. PANIN, F. KEHREN, C. MICHEL, M.E. CASEY, *Fully 3-D PET reconstruction with system matrix derived from point source measurements*, IEEE Trans. Med. Imag., vol. 25, pp. 907-921, 2006
- [23] V.C. SPANOUDAKI, D.P. MCELROY, K. ZELL, S.I. ZIEGLER, *Effect of Temperature on the Stability and Performance of an LSO-APD PET Scanner*, IEEE Nuclear Science Symposium 5, 3014-3017, 2005
- [24] A.B. MANN, *Sampling ADC Based Data Acquisition for Positron Emission Tomography*, PhD Thesis in Electrical Engineering and Communication Technology, Technische Universität München, Munich, Germany, 2009
- [25] F. SCHNEIDER, *Setup and Commissioning of a Positron Emission Tomograph for a Student's Advanced Laboratory Course*, Master Thesis in Engineering Physics, Technische Universität München, Munich, Germany, 2009
- [26] ROOT, *A data analysis framework*, <http://root.cern.ch/>
- [27] CERN, *Conseil Européen pour la Recherche Nucléaire*, <http://cern.ch/>

- [28] LRZ, *Leibniz-Rechenzentrum der Bayerischen Akademie der Wissenschaften*, <http://www.lrz.de/services/compute/linux-cluster/overview/>
- [29] Eckert & Ziegler, Strahlen- und Medizintechnik AG, <http://www.ezag.com/>
- [30] Walter UHL, Technische Mikroskopie GmbH & Co. KG , <http://www.walteruhl.com/>

Chapter 7

Results

7.1 Simulation Studies for MADPET-3

PRIOR to the arrangement of MADPET-3 as described in chapter 5.2 various simulation studies have been performed. GATE [1] was used to model the SiPM detector module to evaluate potential performance properties in terms of gamma ray absorption through photo electric effect and Compton scattering, as well as the influence of the alternating front side and back side readout structure. Additionally the generation of optical photons within the scintillation crystals and their light transportation and collection through the SiPMs have been modelled with the DETECT2000 software package [2]. Two different small animal PET systems based on the SiPM detector modules were simulated with the GATE framework. Corresponding system matrices were calculated with the analytical detector response function model as delineated in the previous chapter. The two different scanner geometries were compared with NEMA phantoms [3] based on physical parameters such as spatial resolution and detection efficiency. The NEMA phantoms were reconstructed with pre-calculated system matrices and an iterative ML-EM reconstruction algorithm.

7.1.1 Simulation of a Single Crystal Readout

Simulation of Gamma Ray Interaction

In a first step a single LYSO crystal measuring $1 \times 1 \times 20 \text{ mm}^3$ was modelled with GATE and DETECT2000 with a simplified detector structure.

For the GATE simulations a single LYSO crystal was irradiated by a collimated beam source of 511 keV gamma quanta with an activity of 3.7 MBq. The source was directly pointing towards the center of one front side of the crystal. The crystal was defined as sensitive detecting volume, in which all occurred single events were stored. From the list of all possible physical gamma ray interactions only photo electric absorption and Compton scattering have been investigated as e.g. the probability of Rayleigh scattering is negligible at the high photon energy level in PET [4]. This set-up was simulated for 30 seconds, an energy window of 100 to 700 keV. All recorded single events were stored and analysed with ROOT [5].

Of the 111 000 000 gamma rays that were directed to the crystal, 79.41% could be detected in the crystal by depositing an energy > 0 . Analysing all detected single events for their deposited energy, 49.60% of them are absorbed through photo electric effect and

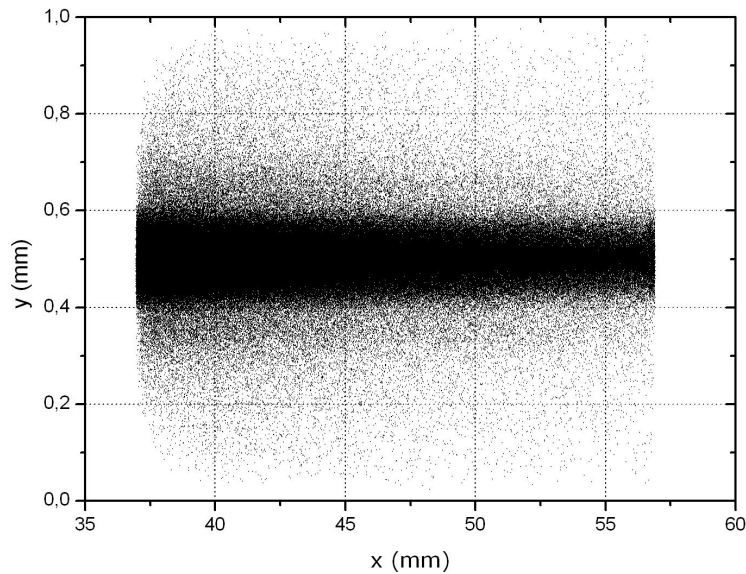


Figure 7.1: Position of interaction in one LYSO crystal. Each black dot represents one gamma ray absorption. The crystal coordinates are ranging from 37.0 to 57.0 mm in x-direction and from 0.0 to 1.0 mm in y-direction, respectively.

49.40% are Compton scattered. The error can be estimated according to the $\frac{1}{\sqrt{N}}$ scaling of the law of large numbers, resulting in an uncertainty of $\pm 0.01\%$. Figure 7.1 describes where the experimental absorption of the gamma rays in the scintillation crystal occurs. Around 53.00% gamma rays will be absorbed within the first third of the crystal in x-direction. Another 34.60% will be absorbed in the second third and only 12.40% in the remaining millimetres at the end of the crystal. Regarding the alternating front and back side readout structure of the SiPM detector modules this aspect is quite important as it indicates that half of the crystals in one detector modules will detect most of the gamma rays close to the SiPM readout surface. The other half of the crystal will register most of the gamma rays at the rear end of the crystal. In this case the generated photons after the gamma ray conversion to optical light, will have to travel longer distances and undergo multiple reflections inside the crystal before being detected by the SiPM. As this alternating front and back side readout cannot be used for recovering additional DOI information for the reconstruction it is important to ensure similar light collection capability for all crystals in one detector module.

In a second step a SiPM detector was added with the same base area of $1 \times 1 \text{ mm}^2$ as the crystals front face (see figure 7.2). A thin layer of optical glue with a thickness of 0.1 mm was directly attached to the LYSO crystal. The SiPM detector unit was modelled as a stack of 4 different layers. According to the MPPC data sheet [6] and the manufacturer's information [7] the detector unit can be described by the following components, with their respective layer thickness in brackets: epoxy resin (0.5 mm), silicon (0.3 mm), aluminium glue (0.02 mm), plastic circuit board (0.6 mm). The simulation was repeated twice: Once with the collimated beam directly pointing at the center of the front side of the crystal, and once with the beam pointing at the SiPM detector unit first (see figure 7.3). The first case will be referred to as back side readout (BSR) and the second one as front side readout (FSR) in the following. By comparison of these two scenarios, it is possible

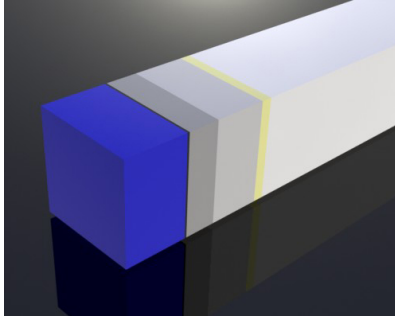


Figure 7.2: Simulated crystal (white) with 5 different layers, representing the optical coupling and the SiPM detector: optical glue (yellow), epoxy resin (bright grey), silicon (dark grey), aluminium glue (black), plastic circuit board (blue).

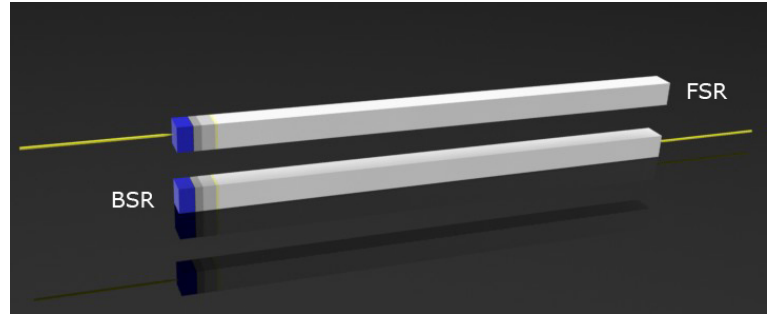


Figure 7.3: Simulated single LYSO crystal and SiPM detector unit with front side (FSR) and back side readout (BSR) structure.

to estimate the influence of the alternating FSR and BSR structure in terms of loss in sensitivity due to scattering in the detector layers. In order to keep the simulation times and output files sizes reasonable, a simulation time of 10 seconds with a source activity of 3.7 MBq was used.

For the BSR geometry a detection efficiency of 79.41% was calculated and 78.01% for the FSR. With these numbers the loss in sensitivity amounts to $1.40\% \pm 0.01\%$. In both geometries more than half of all registered single events involve a Compton scattering inside the crystal or in the SiPM detector layers for the FSR geometry. $1.48\% \pm 0.01\%$ of all single events passed Compton scattering in the detector layer before being detected in the crystal. Table 8.1 presents the contribution of the individual detector layers with respect to the total amount of all Compton scattered events in the different layers.

Table 7.1: Contribution of the individual detector layers to the total amount of Compton scattered events. The uncertainty on the given percentage values is in the range of $\pm 0.05\%$.

Layer (thickness in mm)	Fraction of Compton scattered events in the different detector layers (%)
Optical glue (0.10)	5.10
Epoxy resin (0.50)	27.73
Silicon (0.30)	31.10
Aluminium (0.02)	2.32
Plastic board (0.60)	33.75

Table 7.1 indicates that the scattering in the epoxy resin, the plastic board and the silicon layer are in the same order of magnitude. As the silicon layer is an essential part for the functionality of a SiPM detector and as the plastic board is necessary for mounting the detector on a readout board, only the thickness of the epoxy can be decreased to reduce the amount of scattered events in the detector. Thus, the thickness of the epoxy layer is not only interesting in terms of light collection, but also in terms of sensitivity. Regarding

a single SiPM detector according to [6] the sensitive area of the SiPM is embedded in a ceramic shell with a thickness of 0.68 mm. Since this layer is not part of the design of the SiPM array, its influence has not been considered here, but in [8] the contribution of the ceramic shell to the total scattered events was calculated to be more than 50%.

Light Collection

Additionally the light collection of optical photons for a single LYSO crystal was modelled with the DETECT2000 software package. A scintillation crystal with $1 \times 1 \times 20 \text{ mm}^3$ rectangular volume was modelled, composed of LYSO according to the properties listed in table A.1. To avoid infinite photon trapping an absorption length as well as a scattering length of 30 cm were included in the model of the crystal. In order to study the influence of different surface treatments one front side surface ($1 \times 1 \text{ mm}^2$) of the crystal was defined as sensitive area with a quantum efficiency of 1.00. For each simulation 16352 optical photons have been generated in the first third of the crystal total length, which corresponds to the number of generated photons through photo electric absorption [9]. The first third of the crystal total length refers to the part of the crystal, which is close to side where the crystal is irradiated by the beam source in the case for BSR. The crystal surfaces were defined as polished, ground as well as coated with a metal layer and covered with a diffuse reflecting white paint. The reflection coefficient (RC) has been varied over a wide range from 0.98% to 0.48% for each surface finish material. All results for the light detection and absorption depending on the crystal surface treatment are summarized in table 7.2.

Table 7.2 points out that the number of counted photons increases with the reflection coefficient of the external reflector. The highest amount of counted photons can be achieved with a polished surface and a ground surface both with an external reflector of $\text{RC}=0.98$, resulting in 52.54% or 62.26% detected photons, respectively. Regarding the number of counted photons for a polished surface, this number is only slightly depending on the reflection coefficient of the external reflector. Even for a pure polished crystal without any external reflector around 42% of all generated photons can be detected. Whereas for the three other surface types the number of detected photons shows a strong dependence on the external reflector. The light collection in a perfect polished crystal is therefore mainly based on total internal reflection. This also explains why the amount of escaped photons through the reflector has similar values for all the different reflection coefficients. The main difference between a polished and a ground surface compared to a paint and a metal surface is that total internal reflection due to jumps in the refractive indices is maintained. A paint or metal surface is assumed to be in direct contact with the crystal. As transmission is not considered in the model for a paint and metal surface the number of escaped photons equals zero.

Table 7.2: Light collection of a single LYSO crystal for different surface finishes and reflectors. The given values are mean values out of 10^6 simulations. The uncertainty on the percentage values is in the range of $\pm 0.01\%$.

RC = 0.98	polish	ground	paint	metal
counted photons (%)	52.54	62.26	21.49	31.54
escaped photons (%)	32.52	28.52	0.00	0.00
bulk absorbed photons (%)	14.95	9.22	5.77	4.99
surface absorbed photons (%)	0.00	0.00	72.74	63.46
RC = 0.88	polish	ground	paint	metal
counted photons (%)	48.84	31.86	3.32	12.49
escaped photons (%)	39.68	64.57	0.00	0.00
bulk absorbed photons (%)	11.48	3.56	1.25	1.19
surface absorbed photons (%)	0.00	0.00	95.43	86.32
RC = 0.78	polish	ground	paint	metal
counted photons (%)	48.53	21.69	1.33	7.45
escaped photons (%)	40.85	75.89	0.00	0.00
bulk absorbed photons (%)	10.62	2.42	0.70	0.61
surface absorbed photons (%)	0.00	0.00	97.96	91.94
RC = 0.68	polish	ground	paint	metal
counted photons (%)	47.52	16.56	0.72	4.51
escaped photons (%)	41.97	81.64	0.00	0.00
bulk absorbed photons (%)	10.51	1.80	0.41	0.50
surface absorbed photons (%)	0.00	0.00	98.87	94.99
RC = 0.58	polish	ground	paint	metal
counted photons (%)	46.09	13.70	0.48	2.84
escaped photons (%)	42.10	84.92	0.00	0.00
bulk absorbed photons (%)	10.52	1.38	0.32	0.38
surface absorbed photons (%)	0.00	0.00	99.19	96.77
RC = 0.48	polish	ground	paint	metal
counted photons (%)	45.96	11.25	0.43	1.85
escaped photons (%)	42.91	87.60	0.00	0.00
bulk absorbed photons (%)	11.14	1.15	0.14	0.29
surface absorbed photons (%)	0.00	0.00	99.42	97.85

As the light collection performance is better for a polished and ground surface, the influence for the alternating FSR and BSR has been studied for these two surface treatments. For BSR and FSR optical photons were generated in one third of the crystal which is close to side where the crystal is irradiated by the beam source. Table 8.3 summarizes the results for FSR and BSR for a polished and ground surface with and without an external reflector. For a perfect polished crystal the difference of light detection for FSR and BSR with and without an external reflector is below 1%. Whereas for a crystal with ground surfaces the light detection for FSR and BSR varies by 5.52% without an additional reflector and 20.08% with an external reflector. Additionally the light detection seems to be better in the case for BSR geometry. Before discussing these numbers two more aspects need to be studied which are playing an important role for FSR and BSR.

The first one refers to the question how many photons are reaching the readout surface directly without being reflected before. This portion is equal to the fractional solid angle covered by the detector, which differs for FSR and BSR. As the solid angle is generally defined by

$$\Omega = \int_S \frac{\mathbf{r} \cdot \mathbf{dS}}{r^3} \quad (7.1)$$

, the solid angle covered by the detector depending on the position of generated photons (x_0, y_0, z_0) can be calculated by [10]

$$\Omega = \int_{-0.5}^{0.5} \int_{-0.5}^{0.5} \frac{z_0}{((x - x_0)^2 + (y - y_0)^2 + (z - z_0)^2)^{\frac{3}{2}}} dx dy. \quad (7.2)$$

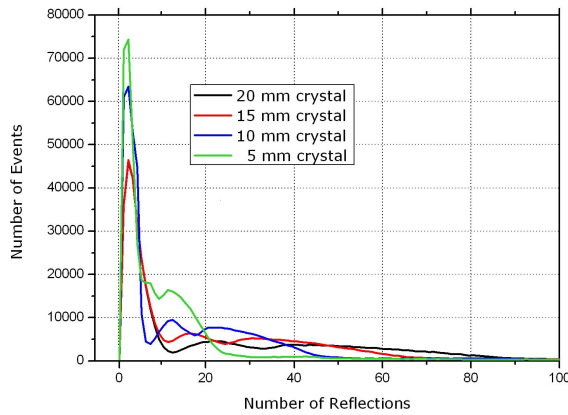
Equation 7.2 counts only for photons which were emitted in the center of the crystal. For an interaction point of photons at a distance of 2.0 mm from the sensitive readout area less than 2% of all generated photons directly hit the detector [10]. For the case of FSR with an interaction point at (0.5 mm, 0.5 mm, 5.0 mm) only 0.32% all generated photons reach the readout surface directly and for the case of BSR only 0.04%. According to these numbers the number of photons directly hitting the readout surface can be neglected for FSR and BSR in the used crystal geometry.

Table 7.3: Light collection for FSR and BSR with different surface finishes and reflectors. The given values are mean values out of 10^6 simulations. The uncertainty on the percentage values is in the range of $\pm 0.01\%$.

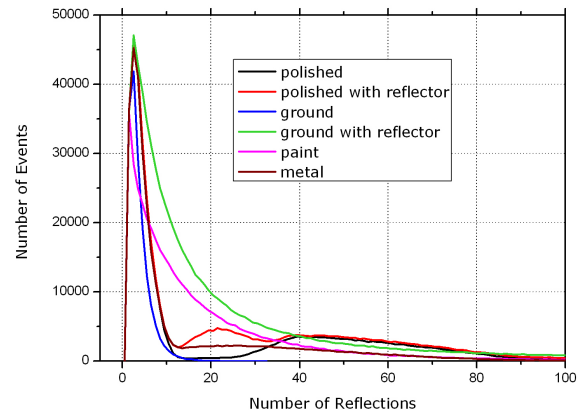
no additional reflector	polish BSR	polish FSR	ground BSR	ground FSR
counted photons (%)	42.09	41.38	6.29	0.78
escaped photons (%)	47.28	47.68	93.14	98.68
bulk absorbed photons (%)	10.62	10.93	0.56	0.54
surface absorbed photons (%)	0.00	0.00	0.00	0.00
mean flight trajectory (mm)	59.04	62.17	7.04	17.76
mean number of reflections	6.70	26.92	3.98	25.51
specular reflector RC=0.98	polish BSR	polish FSR	ground BSR	ground FSR
counted photons (%)	53.03	52.42	63.14	43.06
escaped photons (%)	32.09	32.60	27.62	42.92
bulk absorbed photons (%)	14.87	14.98	9.24	14.02
surface absorbed photons (%)	0.00	0.00	0.00	0.00
mean flight trajectory (mm)	68.31	66.87	48.08	95.86
mean number of reflections	7.57	27.32	4.67	28.88

Another important point regarding long narrow scintillation crystals is how many reflections a photon executes before being detected. This is also interesting for the alternating FSR and BSR structure as the mean flight trajectory differs with the point of gamma ray absorption within the crystal. For this purpose a single LYSO crystal with a direct readout at one front side surface was simulated to obtain the mere influence of the crystal length and of the used reflector. Figure 7.4 illustrates the histograms of the number of reflections for different crystal lengths (a), for different reflector materials (b)

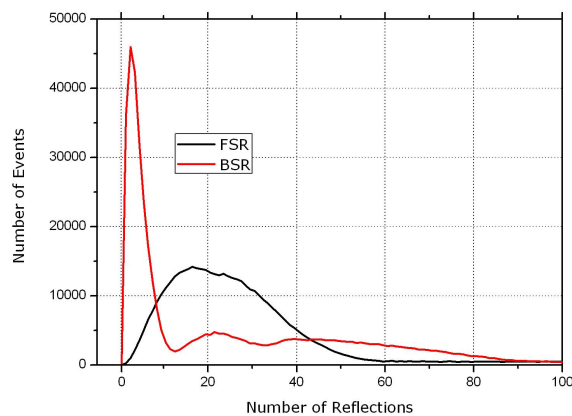
and for the two readout geometries FSR and BSR (c). For the scenarios in (a) and (b) optical photons were generated in the first third of the crystal which again refers to the part of the crystal, which is close to side where the crystal is irradiated by the beam source. The majority of photons needs only a small number of reflections (less than 10) to reach the readout surface, but also a few photons undergo a long flight trajectory in the crystal as indicated by the long tail of the histograms. The mean number of reflections for the 20 mm long crystals is around 7. Regarding figure 7.4 (a), the shorter the crystal, the fewer reflections are needed before the photon is detected. All the simulations show a certain dip in the right shoulder.



(a)



(b)



(c)

Figure 7.4: Distribution of the number of reflections that a photon undergoes before being detected. (a) Number of reflection for different crystal lengths. (b) Number of reflections depending on the crystal surface treatment. (c) Number of reflections for FSR and BSR of 20 mm long crystal with a polished crystal surface without an external reflector.

Focusing on the the 10 mm crystal in figure 7.4 (a), the dip appears at a value of 8 reflections and the corresponding shoulder at a value of 12 reflections. As all the generated optical photons will be emitted equally in all directions, it can be assumed that a certain amount of photons is travelling directly or with only a few reflections towards the readout surface. This amount of photons will lead to the peak between 0 and 7 reflections. In contrast to that a quantity of photons will travel in the opposite direction hitting the near end of the crystal or the side surfaces first before being reflected towards the readout surface. Therefore, these photons undergo more reflections and contribute to the right shoulder at a value of around 12 reflections. Analysing the flight trajectory of all the optical photons hitting the rear end of the crystal opposite to the readout surface, 80% of these photons will experience between 9 and 15 reflections. Figure 7.4 (b) depicts that the number of reflections increases if an additionally external reflector is used. The overall highest number of reflections can be achieved with a ground crystal surface and an external reflector with $RC=0.98$ representing an almost perfect Lambertian reflecting surface. In figure 7.4 (c) the two different readout geometries were compared for a polished crystal surface without an external reflector. In the case of BSR fewer reflections are needed than for FSR. This can be explained due to the fact that for FSR a large number of photons will travel first towards the rear end of the crystal before reaching the readout surface leading to a higher number of reflections. The higher the number of reflections the higher is the probability for being transmitted through the crystal and/or the reflector or being bulk absorbed by the crystal material, which causes light loss for the FSR geometry.

So far a simplified single crystal readout geometry has been studied with one front side surface as a perfect detecting surface (quantum efficiency=1.00). For the next simulation set up all components as described at the beginning of this chapter (see. figure 7.2) will be included to study their influence on the light detection in one single crystal coupled to one SiPM detector. All surface finishes of the crystal are again assumed to be polished with a high reflection coating ($RC = 0.98$). A thin layer of optical glue was directly attached to one front side surface of the crystal, with the dimensions of $1.0 \times 1.0 \times 0.1 \text{ mm}^3$ and a refractive index of 1.55 [10]. The SiPM detector element was designed as a thin layer of epoxy measuring $1.0 \times 1.0 \times 0.3 \text{ mm}^3$ with a refractive index of 1.66. One front side surface ($1 \times 1 \text{ mm}^2$) opposite to the optical glue and the scintillation crystal was defined as sensitive area of the SiPM detector. The epoxy layer was embedded in a plastic shell of $2.0 \times 2.0 \times 0.5 \text{ mm}^3$ with a cavity in the middle for the epoxy layer and sensitive area of the SiPM. The quantum efficiency of the sensitive area was set to 0.25% [6]. All optical photons passing through the optical glue, the epoxy layer and reaching the border surfaces of plastic shell were counted as escaped from the system.

Compared to the values achieved for the light collection under optimized conditions the amount of recorded photons goes down to 8.53% for BSR and 9.1303% for FSR. The quantity of transmitted photons around 26% reflects the amount of photons which are impinging on the sensitive area of the SiPM but not being detected due to the low overall quantum efficiency of the SiPM. Around 18% of all generated photons escape from the simulated system through the crystal side surfaces and the epoxy layer. The number of absorbed photons can be divided into two groups. 15% of all generated photons are absorbed through the bulk material of the crystal defined by the mean free path length of absorption and roughly 32% of the photons are surface absorbed by the dead area of the plastic shell of the SiPM.

Table 7.4: Light collection for a single LYSO crystal coupled to one SiPM detector. The given values are mean values out of 10^6 simulations. The uncertainty on the percentage values is in the range of $\pm 0.01\%$.

	BSR	FSR
counted photons (%)	8.53	9.13
escaped photons (%)	18.05	18.70
bulk absorbed photons (%)	15.06	14.86
surface absorbed photons (%)	32.35	30.74
transmitted photons (%)	26.00	26.57
mean flight trajectory (mm)	61.08	70.47
mean number of reflections	7.88	28.14

As already indicated in table 7.1 the thickness of the epoxy layer is increasing the amount of scattered events in the detector. Its influence has been studied in terms of light collection or light loss. The thickness of the epoxy layer was varied between 0.1 to 0.4 mm. For each photo electric absorption 16352 optical photons were generated in the upper third of the crystal. The crystal surface was assumed to be polished with an specular reflector ($RC=0.98$). The sensitive area of the SiPM was defined as a perfect detecting surface (quantum efficiency = 1.00) in order to obtain the mere influence of the different epoxy layers. The results in table 7.5 characterize that the light collection strongly depends on the thickness of the epoxy layer. Reducing the thickness of the epoxy layer from 0.3 mm to 0.1 mm would increase the number of detected photons by about 10%.

Table 7.5: Light collection for a single LYSO crystal coupled to one SiPM detector for different epoxy layers. The given values are mean values out of 10^6 simulations. The uncertainty on the percentage values is in the range of $\pm 0.01\%$.

epoxy layer (mm)	0.1	0.2	0.3	0.4
counted photons (%)	46.35	41.31	36.83	33.94
escaped photons (%)	10.03	15.32	19.09	21.48
bulk absorbed photons (%)	11.31	11.31	11.56	12.03
surface absorbed photons (%)	32.31	32.05	32.52	32.55

Figure 7.5 depicts how the optical photons impinge onto the sensitive area of a SiPM for different crystal surfaces and epoxy layers. In the simulation 10^6 gamma rays were absorbed in the upper third of the LYSO crystal. For each gamma ray absorption again 16352 were generated whose final position was recorded. The SiPMs used for MADPET-3 consist of 400 Geiger-mode APDs per 1.0 mm^2 each measuring $50.0 \times 50.0 \mu\text{m}^2$. Each of those individual Geiger-mode APDs has an active area of $39.21 \times 39.21 \mu\text{m}^2$ which was modelled with a quantum efficiency of 0.70 [6]. All the optical photons impinging onto the readout surface were additionally analysed if they were hitting a sensitive area of one Geiger-mode APDs of the SiPM or if they were hitting one dead area between the individual Geiger-mode APDs. For the simplified simulation set-up in figure 7.5 (a) under optimized conditions without any epoxy layer and a specular reflector ($RC=0.98$)

the two-dimensional histogram of all photons reaching the sensitive area of the SiPM shows a uniform distribution over the whole area of the SiPM. After including an epoxy layer with a thickness of 0.3 mm into the simulation the spatial distribution involves a center-focused structure with more photons impinging on the center of the SiPM (figure 7.5 (b)). This can be explained by additional reflections that occur at the side surfaces of the epoxy layer, which will change the direction of the incoming photon towards the center. Adding an additional layer of black paint on the side surfaces of the epoxy layer will maintain a uniform distribution for the detected photons as in figure 7.5 (a) without an epoxy layer. Also different positions for the light generation were tested. As all optical photons are emitted isotropically and their spreading is mainly defined by their relative angle to the surfaces of the crystal the distribution offered no significant difference for the crystals with a specular reflector. The similar simulations as in figure 7.5 (a) and (b) were performed for a diffuse reflecting material ($RC=0.98$) as crystal surfaces. As the influence of an 0.3 mm thick epoxy layer was insignificant for a crystal with a diffuse reflector regarding the spatial distribution of detected photons, only the results without an epoxy layer are presented in figure 7.5 (c) and (d). Even without any epoxy layer the distribution in figure 7.5 (c) possesses a center-focused structure. In the simulation corresponding to figure 7.5 (d) a position at the lower edge of the crystal has been chosen as interaction point for the gamma rays. Although the optical photons originated from the upper third of crystal the original position of generation is maintained in the final distribution as there are more photons reaching an area between 0.0 and 0.5 mm in x-direction and y-direction. As SiPMs have a limited dynamic range due to their number of Geiger-mode APDs they can only be operated properly within a certain range. Every Geiger-mode APD requires a certain time to recover before being capable to detect another incoming photon. Therefore a uniform distribution would be advantageous for the incoming photons on the SiPM surface.

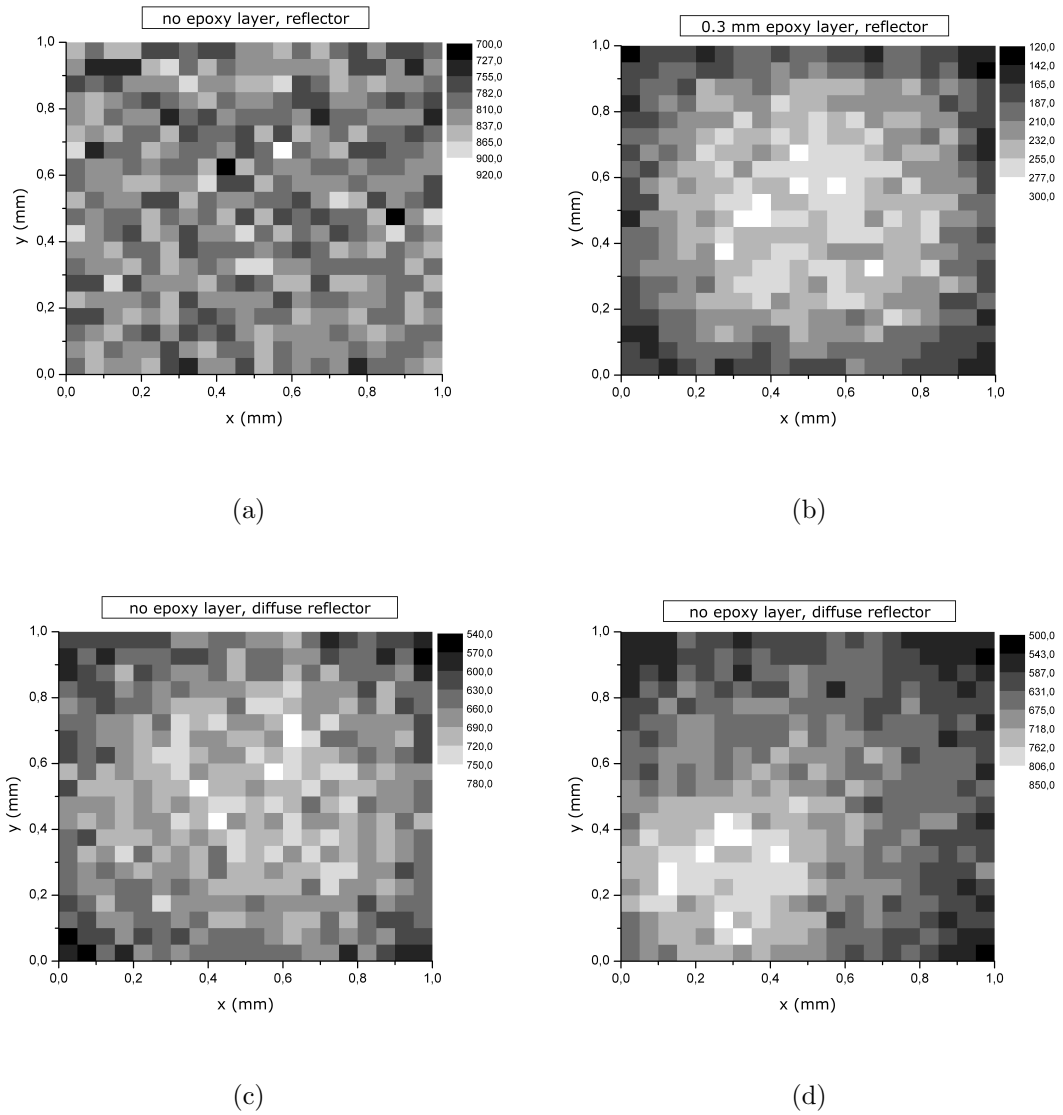


Figure 7.5: Two-dimensional histograms of the spatial distributions of photons impinging onto the sensitive area of the SiPM with 400 Geiger-mode APDs per 1.0 mm^2 : (a) single polished crystal with no epoxy layer and a specular reflector, (b) single polished crystal coupled to an SiPM, (c) single polished crystal with no epoxy layer and a diffuse reflector; light generation at the center of the crystal, (d) single polished crystal with no epoxy layer and a diffuse reflector. Optical photons were generated in the center of the SiPM (0.5,0.5,15.0 mm) in the case of (a),(b) and (c) whereas in the case of (d) light generation proceeded at the edge of the crystal (0.25,0.25,15.0 mm). The maximum value for incident photons was denoted as white and the minimum value as black for each subfigure.

7.1.2 Simulation Results for a Single SiPM Detector Module

A single SiPM detector module has been simulated with the GATE Monte Carlo Simulation toolkit. One of the central crystals (crystal no. 18 in figure 7.6) has been irradiated with a collimated beam source for 30 seconds. The source was directly pointed to the center of the front surface of the crystal. For all generated gamma rays the coordinates of interaction points in the scintillation crystal, as well as the deposited energy have been recorded. A low energy threshold of 100 keV was applied, which represents a commonly used level to cut off noise for small animal PET scanners [9]. Figure 7.7 shows the histogram of all absorbed gamma rays in the SiPM detector array. 79.4% of all detected gamma rays are collected in the irradiated central crystal. Only half of these events generate optical photons through electric effect. The other half deposits energy in the crystal through single or multiple Compton scattering. A histogram of all the single events occurring in the irradiated central crystal no. 18 is illustrated in figure 7.8. Due to Compton scattering the remaining 20.6% of all detected gamma rays are spread over many crystals in the detector array as illustrated in figure 7.10). 2.0% of all Compton scattered events will be detected in the direct neighbouring crystal within one 1×4 SiPM sub-array (crystal no. 19 and 17 in figure 7.6), those scintillation crystals and SiPM are arranged without any gap between them. The other direct neighbouring crystals, which are separated by a small air gap and a thin layer of barium sulphate are collecting 1.6% (crystal no. 22 and 14 in figure 7.6) of all detected gamma rays due to Compton scattering. All the recorded events through Compton scattering in neighbouring crystals will lead to mispositioning of the source in the resulting reconstructed images as in this case the wrong crystal and therefore also the wrong LOR will be assigned for the detected event in a certain voxel.

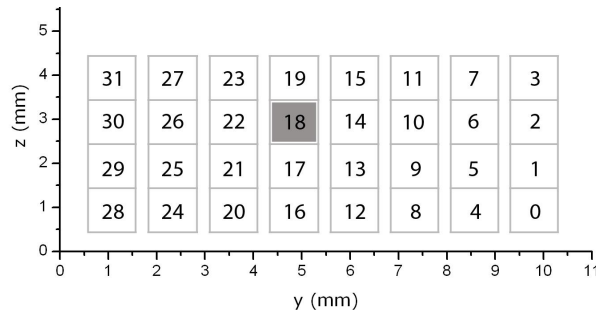


Figure 7.6: Position of crystal no. 18 within the SiPM detector array in the y-z plane.

One possibility to suppress events to be counted after Compton scattering is to apply a higher low energy threshold as cut off. Figure 7.7 presents the histogram of all absorbed gamma rays in the SiPM detector array for a 400 keV low energy threshold. For this energy threshold 94.2% of all detected gamma rays will be collected in the direct irradiated crystal. Only 5.8% of all detected gamma rays are recorded as scattered event within the whole array. In the direct neighbouring crystal (crystal no. 19 and 17) with air gap in between around 0.6% Compton scattered photons are detected and the neighbouring crystals separated by a small air gap and a thin layer of barium sulphate are collecting 0.5% (crystal no. 22 and 14) of all detected gamma rays due to Compton scattering.

To characterize how many wrong coincidences could be assigned due to Compton scattering between two SiPM detector modules the following simulation set-up has been

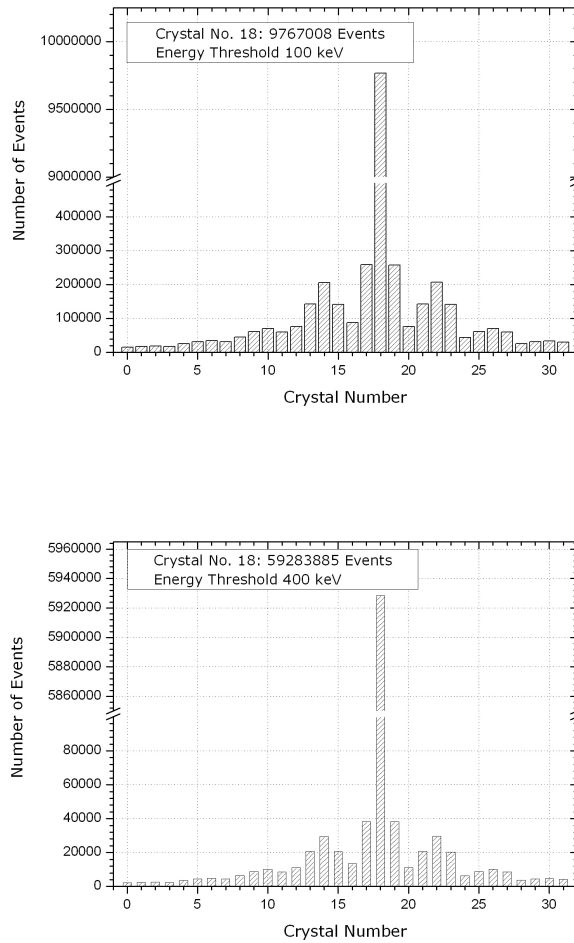


Figure 7.7: Distribution of all generated gamma ray interactions over the whole SiPM detector array. The low energy threshold was set to 100 keV (top) and to 400 keV (bottom).

analysed. Two SiPM detector modules were arranged in front of each other in a distance of 70 mm. A collimated beam source was modelled pointing directly to the front side surface of one crystal in the center of each SiPM module as already indicated in figure 7.6. For both detector modules the same crystal was irradiated by the source. The collimated beam source was producing pairwise gamma rays emitted at an angle of 180° . The activity of the source was 3.7 MBq and the total simulation run time was set to 10 seconds. The list of single events output by the GATE toolkit was post-processed using a custom-made C++ code to generate the list of coincidence events and differentiate true coincidences between the two crystals which were directly irradiated by the source and inter-crystal coincidences due to Compton scattering as well as random coincidences produced by two simultaneously detected events within the coincidence time window. A coincidence window of 20 ns was applied for a low energy threshold of 100 keV and 400 keV. During the simulation in total 59002880 events were generated. Using a low energy threshold of 100 keV 16.55% true coincidences are detected by the two irradiated crystals, 3.90% are recorded as inter-crystal coincidences due to Compton scattering and

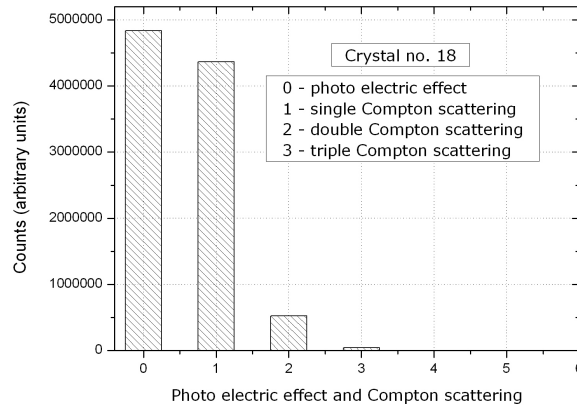


Figure 7.8: Gamma ray absorption through photo electric effect and Compton scattering for the direct irradiated crystal. From all detected gamma rays around 50% are absorbed through photo electric effect. The other half undergoes single or multiple Compton scattering.

0.37% of all detected events occur as random coincidences. By applying a low energy threshold of 400 keV only 24043285 events lie above the energy threshold. From this number 16.07% of all events are accounted as true coincidences, 4.16% as inter-crystal coincidences and 1.08% as random coincidences. Relating these numbers to the total number of generated events (59002880) a low energy threshold of 400 keV will lead to loss in sensitivity of 11.26% regarding the number of true coincidences. This can also be visualized in the resulting reconstructed images in figure 7.9. For two SiPM detector modules a SM covering the small volume between the two modules, has been calculated with the DRF model. This SM was used to reconstruct the collimated beam source in one plane with an ML-EM reconstruction algorithm for the two low energy thresholds. For the low energy threshold of 100 keV the list of single events was processed in two different ways. In the first step only true coincidences were considered for the reconstruction (left column of figure 7.9). In the second step the inter-crystal coincidence were treated as "normal" coincidences in addition to the true coincidences in the reconstruction code to visualize their influence in the resulting image (right column of 7.9). For comparison in center column of figure 7.9 the beam source was reconstructed for the low energy threshold of 400 keV. As only two detector modules were simulated the beam source appears as horizontal line in the coronal and transverse view of the reconstructed images representing the LOR between the two irradiated detector modules. Figure 7.9 shows the results after 20 iterations and all images are normalized to the same maximum value. The loss in sensitivity is clearly visible comparing the images with a low energy threshold of 100 keV and 400 keV as the one with 400 keV appears much darker. Also additional LORs can be slightly recognized in the right column of figure 7.9 due to inter-crystal coincidences leading to a broadening in the appearance of the source.

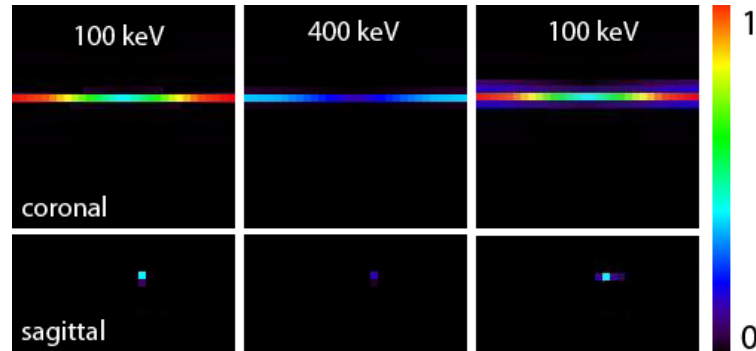


Figure 7.9: Reconstructed images for two SiPM detector modules. One central crystal of both detector modules was directly irradiated by a collimated beam source. Left: A low energy threshold of 100 keV was applied. Only true coincidences were considered for the reconstruction. Middle: A low energy threshold of 400 keV was applied. Right: For the reconstruction true and inter-crystal coincidences were taken into account by a low energy threshold of 100 keV. The coronal and sagittal views show the results after 20 iterations with an ML-EM reconstruction. The SM was pre-calculated based on the DRF model. All figures are normalized to the same maximum value.

As the epoxy layer turned out to be the most critical part within one SiPM detector array for good crystal identification, a special focus was set to study its influence for the generation and propagation of optical photons. Therefore, one SiPM detector module was simulated with the DETECT2000 software package. The different components for the SiPM detector module were modelled in a similar way as for a single LYSO crystal coupled to one SiPM. The main difference is that every 1×4 SiPM sub-array of the detector module is attached to one common epoxy layer and one common layer of optical glue measuring $1.0 \times 4.0 \times 0.3 \text{ mm}^3$ and $1.0 \times 4.0 \times 0.1 \text{ mm}^3$ as this would also be the case for the SiPM detector module. Each crystal surface was defined as a perfectly polished surface covered with a diffuse reflecting material ($RC = 0.98$) to represent the barium sulphate layer between the crystals. Additionally a small air gap (thickness 0.01 mm) was put between the crystals and the reflecting material to maintain to ability of total internal reflection on the crystal side surfaces. Optical photons were generated in one central crystal (crystal no. 18) of the SiPM detector module and the coordinates of each detected photon within the module was recorded. Figure 7.10 identifies how the generated photons were distributed over the whole detector module. The most distinctive light crosstalk occurs between the crystals which are attached to one common layer of optical glue and epoxy layer (crystal no. 20, 19 and 17).

To ascertain if the distribution of detected photons is determined by the properties of the external reflector or the common layer of optical glue and epoxy several scenarios were simulated. The table shows the results for different external reflectors ranging from a perfect one with a reflection coefficient of 1.00 to a pure polished crystal surface without any external reflector. Regarding the case of a perfect external reflector ($RC = 1.00$), which represents LYSO crystals with a perfect light collection within the crystal, 7.26% of all detected photons are counted in the crystal where the photons have been generated. As the light collection in this case is optimal concerning the crystals properties, the light crosstalk of 3.27% (sum of detected photons in crystals no.20, 19 and 17) in the other

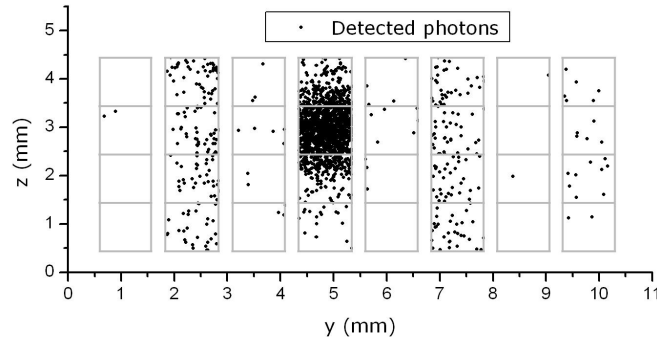


Figure 7.10: Distribution of detected photons in one SiPM detector module.

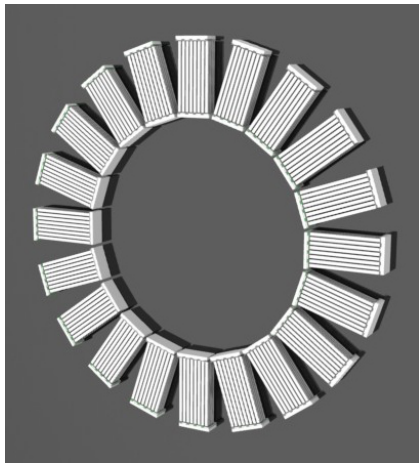
three crystals of the same 1×4 sub-array can only be induced due to light propagation in the commonly attached layer of optical glue and epoxy. If the reflection coefficient of the external reflector is addressed to a lower value of 0.98 corresponding to the one for barium sulphate, the number of detected photons in crystal no. 18 and in the three neighbouring crystals provides similar results (difference in light detection in crystal no. 18 $< 1.5\%$ and difference in light crosstalk in the crystal no. 20, 19 and 17 $< 0.5\%$). Even in a SiPM detector module without any additional external reflector on the crystal surfaces the detecting efficiency for crystal no. 18 decreases only about 2% and the light distribution into the three neighbouring crystal is in the same order of magnitude. This indicates that the light collection and detection is mainly supported by the air gap between the crystal surfaces and the external reflector as it does not change significantly with the detection coefficient of the reflector. Removing the air gap between the crystal surfaces and the reflector leads to an almost uniform distribution of detected photons among the four crystals in one 1×4 SiPM sub-array. All results are summarized in table 8.6.

Table 7.6: Light distribution in one SiPM detector module for different surface finishes and reflectors. Optical photons were generated in crystal no. 18 in the upper third of the crystal length. The given values are mean values out of 10^6 simulations. The uncertainty on the percentage values is in the range of $\pm 0.01\%$.

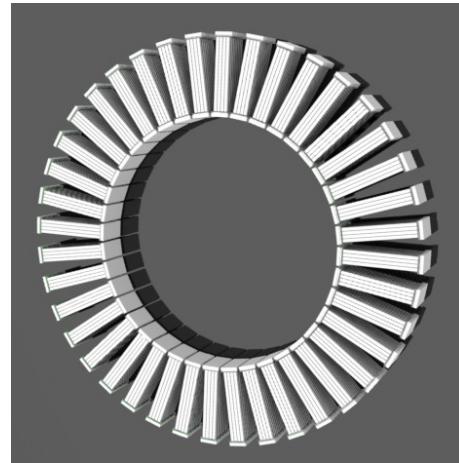
Reflection coefficient	1.00	0.98	0.50	0.00	no air gap
counted photons (%)	12.77	11.15	9.79	8.86	6.85
escaped photons (%)	9.64	30.13	28.99	51.96	60.53
bulk absorbed photons (%)	39.73	25.48	32.02	13.14	11.83
transmitted photons (%)	37.85	33.24	29.20	26.05	20.78
counted photons in					
crystal no. 20 (%)	0.16	0.12	0.09	0.09	1.37
crystal no. 19 (%)	1.58	1.43	1.21	1.09	1.42
crystal no. 18 (%)	7.26	6.24	5.31	5.17	1.51
crystal no. 17 (%)	1.53	1.33	1.21	1.05	1.20

7.1.3 Simulation of the MADPET-3 System

GATE was used to model a prototype small animal PET scanner based on the SiPM detector modules described in chapter 5.2 with different geometries. There are basically two possibilities to arrange the SiPM detector modules in one ring: 20 detector modules with 8 crystals facing the center of the scanner and 40 detector modules with 4 crystals facing the center of the scanner (figure 7.11).



(a) MADPET-3 with 20 detector modules



(b) MADPET-3 with 40 detector modules

Figure 7.11: Two different scanner geometries for MADPET-3. (a) 20 Detector modules with 4 crystal rings in the axial FOV and (b) 40 detector modules with 8 crystal rings in the axial FOV. The diameter for both scanners measures 70 mm.

For both geometries SMs were calculated based on the DRF model described in chapter 7. As integral precision, required for the SM calculation in the DRF model, a value of 30 has been chosen, which was found to be an appropriate value for MADPET-2 [11]. The the maximum intrinsic resolution of a PET scanner with scintillation crystals measuring $1 \times 1 \times 20 \text{ mm}^3$ is defined by half of the crystal front side surface length. Therefore, the voxel size has to be chosen smaller than the maximum intrinsic resolution resulting a voxel size of 0.25 mm^3 . As the corresponding size of the SMs is quite huge the calculation were done on a 8-way AMD Opteron cluster with a working memory of 32 GB per node provided by the Leibniz-Rechenzentrum. One node was needed for the SM calculation of the scanner geometry with 20 detector modules and three nodes for the scanner geometry with 40 detector modules. All characteristics that have been considered for the SM calculation of the two MADPET-3 geometries as well as the required computational time and storage account are listed in table 7.7.

To characterize and compare the different SMs prior to the evaluation of the reconstructed images sensitivity matrices have been generated. A sensitivity matrix is obtained by summing up all the SM elements H_{ij} over the LORs for a specific voxel j , representing the detection probability of an annihilation event emitted from this voxel by the whole system. Therefore, the sensitivity matrix elements S_j are calculated by [13]:

$$S_j = \sum_{i=0}^I H_{ij} \quad (7.3)$$

Table 7.7: Characteristics of the two MADPET-3 geometries used for the SM calculation

	MADPET-3-20	MADPET-3-40
Number of crystals	640	1280
Number of LORs	409600	1638400
Number of voxels	280 x 280 x 16	280 x 280 x 40
Voxel size	0.25 x 0.25 x 0.25 mm ³	0.25 x 0.25 x 0.25 mm ³
Axial detector rings	4	8
Number of crystals per detector ring	160	160
Diameter	70 mm	70 mm
Size of System Matrix	23 GB	74 GB
Computing Time	26h	60h

The sensitivity matrix for the central slice of the transverse, coronal and sagittal plane is presented in 7.12 for the studied geometries. Both pictures are normalized to the same maximum. The sensitivity matrices obtain certain loop-like structures and a few internal rings. These loop-like structure are mainly representing the total number of detector modules and their dead space between them, as the spikes of the outer internal rings count up to a number of 20 and 40, respectively. The rings are coincident with the missing sampling due to the distance between the detector modules, shown in figure 7.13 on the left side for the MADPET-3 geometry with 20 detector modules. Another common characteristic is that the sensitivity of the SM is increasing radially from the center to the edges of the FOV. Voxels at the edge of the FOV obtain a larger solid angle and a more effective crystal length to absorb gamma rays (see right side of figure 7.13). The increase in effective crystal length can be understood qualitatively, assuming that the detection probability of gamma rays is proportional to the distance traversed by the photon within the crystal ring. Annihilation events leaving a voxel close to the center of the FOV pass more or less the same distance in the crystal ring (marked by the red bars in right side of figure 7.13). In contrast to that annihilation events emitted from a voxel at the edge of the FOV travel a larger distance in the crystal ring (marked by the violet bars in right side of figure 7.13). Therefore, photons emitted from the edge of the FOV have a higher probability of being detected. Line profiles of the sensitivity matrices for the two geometries through the central slice of the transverse plane are presented in figure 7.14 and the corresponding difference between both. The two scanner geometries possess a local maximum in sensitivity of similar intensity (difference in sensitivity < 4%) in the center of the FOV. In a small region around the center of the FOV (± 10 mm) the scanner geometry with 40 detectors modules reveals stronger fluctuations in sensitivity compared to the geometry with 20 modules. For the scanner geometry with 40 detectors modules the fluctuations compared to the maximum value of sensitivity are 51.47% and for scanner geometry with 20 detectors modules 28.57%.

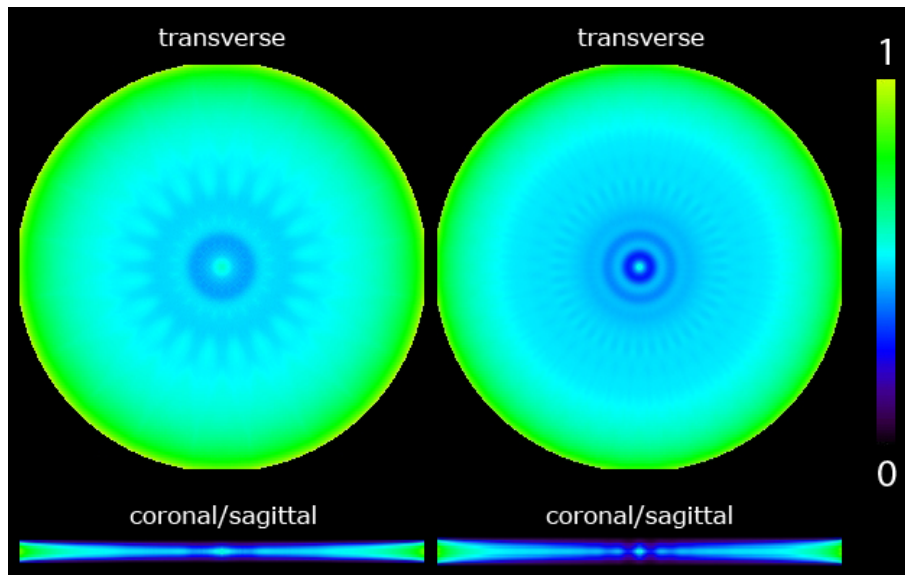


Figure 7.12: System matrix for MADPET-3 based on the DRF model with 20 detector modules (left) and 40 modules (right). The top view shows the sensitivity map of the transverse plane, the bottom view the sensitivity plots of the coronal and sagittal plane which are identical due to the scanners symmetries. All plots are normalized to the same maximum value.

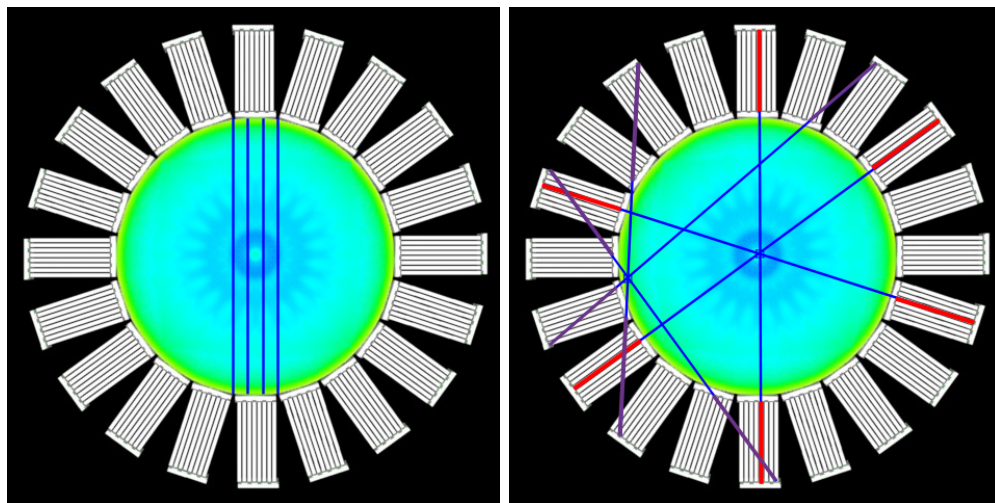


Figure 7.13: Graphical explanation of the loop-like structures of the sensitivity matrix and the increase of sensitivity towards the edge of the FOV. The central black ring is corresponding to the under-sampled areas due to the dead space between the detector modules as indicated by the blue lines in the left figure. In the right figure two voxels are marked, one in the center and one at the edge of the FOV. For the voxel in the center many coincidences can be found where the intersection of the photon pair is perpendicular to the crystal front side. The corresponding intersection length is indicated by the red bars. In contrast, one voxel at the edge of the FOV most of the intersection are not perpendicular and the corresponding intersection lengths (violet bars) are much longer. As the probability of detection is proportional to intersection length of the photon pair in the detector, the voxels closer to the edge obtain a higher probability.

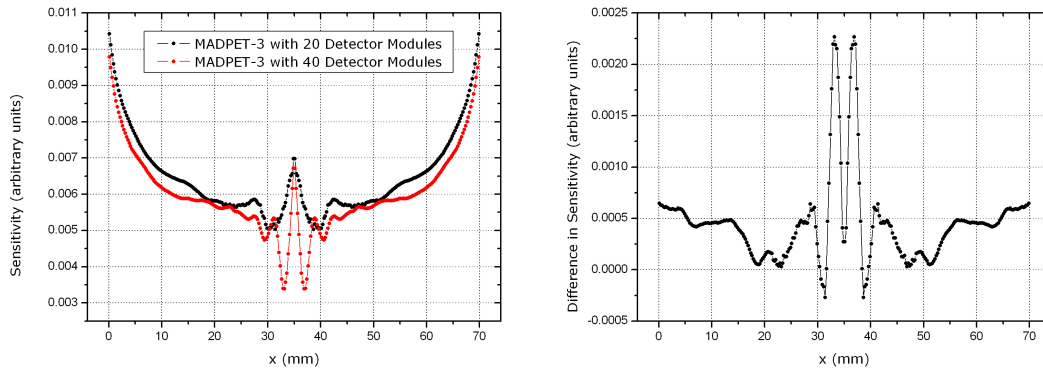


Figure 7.14: Left: Line profiles of the sensitivity matrices for the two geometries through the central slice of the transverse plane. Right: Difference of the two line profiles.

To study the image quality obtained by using the two SMs, the following sources have been simulated with GATE:

- ◇ A Uniform phantom represented by a homogeneously filled cylindrical phantom with a diameter of 30.0 mm a height of 8.0 mm covering around 40% of the FOV. The cylinder was filled with an activity of 6.6 MBq and the acquisition time of the simulation was 100 seconds. This phantom was used to study how homogeneously the cylinder could be reconstructed in the resulting images.
- ◇ A Derenzo-like phantom consisting of five 8.0 mm long rod sources with diameters of 1.0, 1.5, 2.0, 2.5, 3.0 mm, respectively. The activity concentration was 118 kBq/mm³. The acquisition time of the simulation was 100 seconds as for the uniform phantom.

For both phantoms the recorded single events were stored and analysed with ROOT. In order to focus on the image quality provided by the SMs, there was no attenuation material included in the simulated sources and therefore neither scattered events nor attenuation within the phantoms was considered. This approximation seems reasonable as the contribution of scattering or attenuation in the imaged objects for small animal PET scanners is rather small in comparison to scattering in the detectors [14], [15], [16], [17]. For comparison and due to the larger crystal volume for the scanner geometry with 40 detector modules, only 4 crystals instead of 8 rings towards the axial FOV were considered in the SM and in the simulation of the phantoms. That way the same number of crystals (160) and with it the same detecting crystal volume was maintained for both geometries. Reconstruction was performed in 3D using an ML-EM iterative reconstruction algorithm. In figure 7.15 the reconstructed images for the uniform phantom are drawn for the transverse, coronal and sagittal plane of the central slice. Every slice of the three planes reveals a significant decrease of sensitivity in a small region around the center of the FOV. This area is coincident with the region of the sensitivity matrices where the strong fluctuations in intensity occurred as shown in figure 7.14. Regarding the line profiles (figure 7.14) through the reconstructed images there is a decrease of sensitivity of

around 77% for MADPET-3 with 40 detector modules and around 30% for MADPET-3 with 20 detector modules. The region, where the decrease of sensitivity appears, is smaller for the scanner geometry with 40 detector modules (± 2.5 mm around the center of the FOV) than the one 20 detector modules (± 8 mm around the center of the FOV). Additionally the overall sensitivity is around 44% higher in the case of scanner geometry with 40 detector modules.

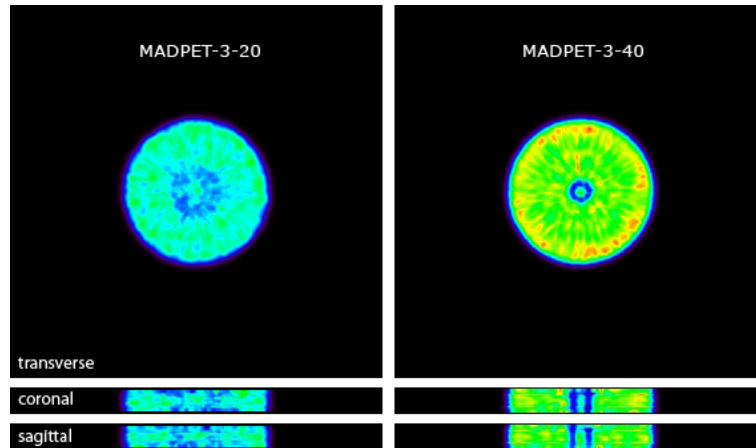


Figure 7.15: Reconstructed uniform phantom after 30 iterations for the two MADPET-3 scanner geometries with 20 detector modules (left) and with 40 detector modules (right). The pictures are normalized to the same maximum value.

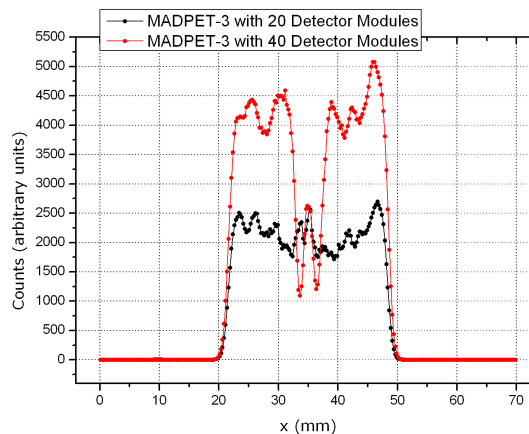


Figure 7.16: Line profile through the central slice in the transverse plane.

The same uniform phantom was re-reconstructed with new SMs. For the new SMs the integral precision has been doubled to a value of 60. The value of 30 for the integral precision and therefore for the calculation of the SM weights was used with success for the MADPET-2 scanner [11]. But it should be mentioned that the scintillation crystals

in the MADPET-2 scanner are much bigger ($2.0 \times 2.0 \times 6.0 \text{ mm}^3$ in the first crystal layer and $2.0 \times 2.0 \times 8.0 \text{ mm}^3$ in the second crystal layer) than the ones used for MADPET-3 [12]. This fact may justify the assumption that the inhomogeneity in the reconstructed images could result from inappropriate sampling in the calculation of the SMs. Figure 7.17 shows the reconstructed images for the uniform phantom with an integral precision of 60. The improvement is clearly visible in reconstructed images but also in the line profiles as shown in figure 7.18.

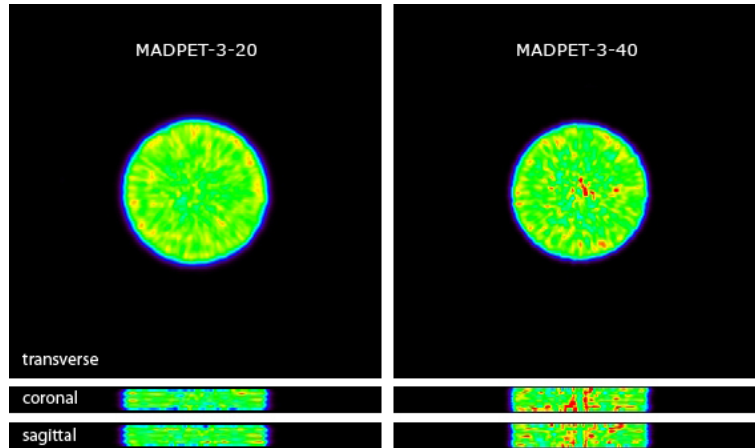
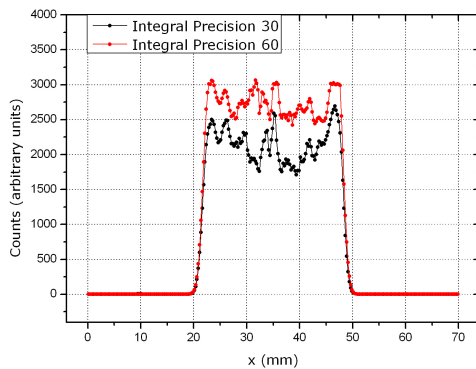
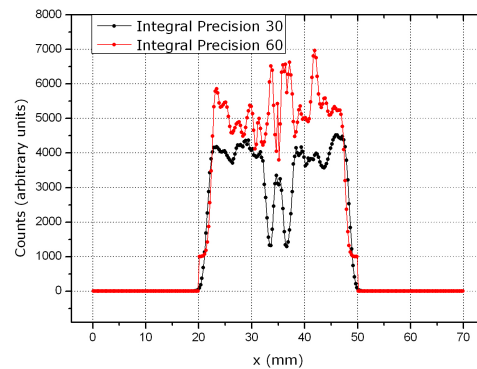


Figure 7.17: Reconstructed uniform phantom after 30 iterations with an integral precision of 60 for the two MADPET-3 scanner geometries with 20 detector modules (left) and with 40 detector modules (right). All pictures are normalized to the same maximum value.



(a) MADPET-3 with 20 detector modules



(b) MADPET-3 with 40 detector modules

Figure 7.18: Line profile through the central slice in the transverse plane for both scanner geometries and for an integral precision of 30 and 60, respectively.

For quantitative comparison between the two scanner geometries and the SMs the mean value, the variance, the standard deviation as well as the maximum and minimum value within the reconstructed uniform phantoms are presented in table 7.8. The Derenzo-like phantom was reconstructed in the same way as the uniform phantom. The results for

the transverse and coronal plane for the two scanner geometries are presented in figure 7.19 after 30 iterations. Here also a better image quality can be achieved using a SM with an higher integral precision of 60. Especially for the smaller rods the shape is not perfectly spherical when using a SM with a integral precision of 30. For all the studied cases each rod was fitted with a Gaussian and the corresponding FWHM values with their uncertainty are summarized in table 7.8.

Table 7.8: This table summarizes the mean value, the variance, the standard deviation, the minimum and maximum values for the reconstructed uniform phantom.

Data Set	Mean	Var	Std Dev [%]	Min	Max
MADPET-3-20 int. prec. 30	2080.07	87484.3	14.22	1245.11	3080.4
MADPET-3-20 int. prec. 60	2761.14	71600.9	9.69	1816.67	3800.74
MADPET-3-40 int. prec. 30	3626.18	457441	18.65	1014.67	5469.19
MADPET-3-40 int. prec. 60	3797.14	370280	16.03	2208.2	8217.93

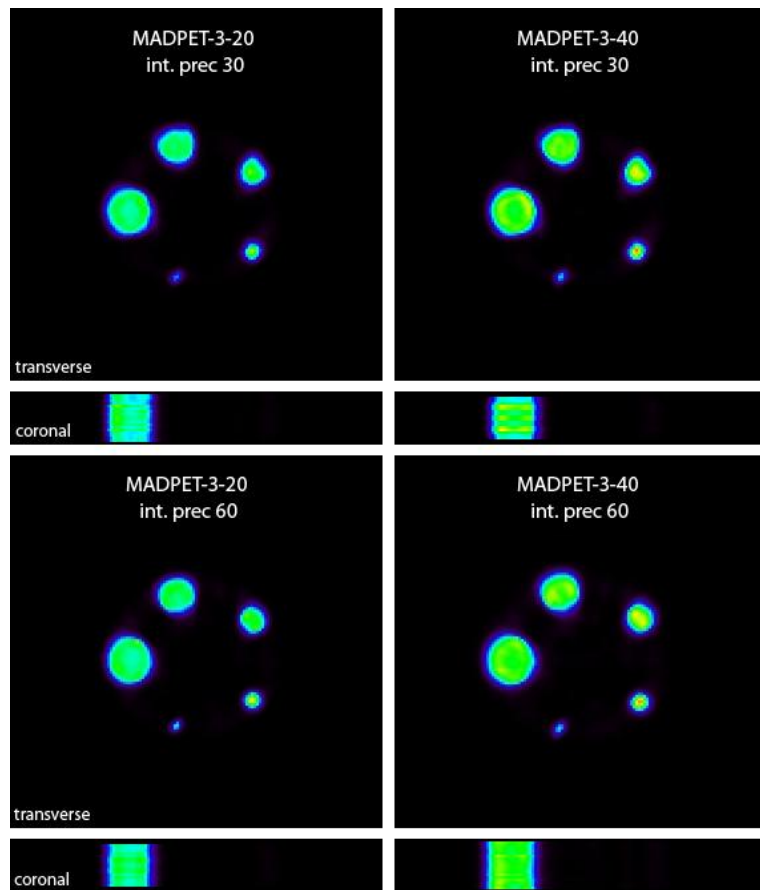


Figure 7.19: Reconstructed images for the cylindrical phantom after 30 iterations. The left column shows the transverse and coronal view for MADPET-3 with 20 detector modules with an integral precision of 30 (top) and 60 (bottom) and the right column depicts the corresponding results for MADPET-3 with 40 detector modules. In the central coronal plane only the biggest rod with a diameter of 3.0 mm is visible. All pictures are normalized to the same maximum value.

Table 7.9: FWHM values for the reconstructed Derenzo-like phantom.

	MADPET-3-20		MADPET-3-40	
	prec 30	prec 60	prec 30	prec 60
FWHM	$0.79 \pm 1.78 \cdot 10^{-5}$	$0.68 \pm 1.15 \cdot 10^{-5}$	$0.82 \pm 2.45 \cdot 10^{-5}$	$0.74 \pm 1.25 \cdot 10^{-5}$
FWHM	$1.18 \pm 7.29 \cdot 10^{-6}$	$1.21 \pm 8.48 \cdot 10^{-6}$	$1.15 \pm 9.55 \cdot 10^{-6}$	$1.30 \pm 7.61 \cdot 10^{-6}$
FWHM	$1.90 \pm 1.05 \cdot 10^{-5}$	$1.95 \pm 1.27 \cdot 10^{-5}$	$1.96 \pm 1.26 \cdot 10^{-5}$	$1.99 \pm 1.05 \cdot 10^{-5}$
FWHM	$2.88 \pm 1.39 \cdot 10^{-5}$	$3.03 \pm 1.79 \cdot 10^{-5}$	$2.96 \pm 1.78 \cdot 10^{-5}$	$3.12 \pm 1.44 \cdot 10^{-5}$
FWHM	$3.31 \pm 1.78 \cdot 10^{-5}$	$3.64 \pm 2.15 \cdot 10^{-5}$	$3.83 \pm 2.15 \cdot 10^{-5}$	$3.89 \pm 1.79 \cdot 10^{-5}$

As already shown in the reconstructed images of the uniform phantom, the image quality improves by increasing the integral precision from 30 to 60. Inhomogeneities are visible in the coronal regarding the biggest rod with a diameter of 3.0 mm for an integral precision of 30 (right column, top view of figure 7.19). Comparing the FWHM values of the Gaussian fits with the true diameter values every rod is slightly underestimated except for the biggest rod by the reconstruction code.

7.2 Measurements with MADPET-3

As described in chapter 5.2 a small animal PET scanner consisting of two SiPM detector modules was build. In order to provide enough space required by the readout boards of the detector modules it was necessary to increase the FOV from 70 mm to 100 mm. To keep the computational time and storage demands for the reconstruction at a feasible level a geometry similar to the scanner geometry with 20 detector modules was chosen for MADPET-3 but with 24 detector modules in total. All characteristics for MADPET-3 and the corresponding SM are listed in table 8.10. The SM was generated based on the DRF model with an integral precision of 60 as the reconstructed images showed better results when using a higher integral precision in the previous chapter.

Table 7.10: Characteristics of the MADPET-3 scanner used for the SM calculation.

MADPET-3	
Number of crystals	768
Number of LORs	589824
Number of voxels	$400 \times 400 \times 16$
Voxel size	$0.25 \times 0.25 \times 0.25 \text{ mm}^3$
Axial detector rings	4
Number of crystals per detector ring	160
Diameter	100 mm
Size of System Matrix	51 GB
Computing Time	34 h

The sensitivity matrix for the central slice of the transverse, coronal and sagittal plane is presented in figure 7.20 for MADPET-3. All pictures are normalized to the same

maximum. Due to the similar geometry as for the scanner geometry with 20 detector modules as in figure 7.12 the sensitivity matrix of MADPET-3 contains the same loop-like structures and internal rings. This SM was used as basis for the ML-EM reconstruction. As MADPET-3 contains only 2 detector modules instead of 24 which are considered in the SM, the scanned objects have to be rotated in steps of 15° and should not exceed the volume covered by the two opposite detector modules which measures $9.75 \times 9.75 \times 4.00 \text{ mm}^3$.

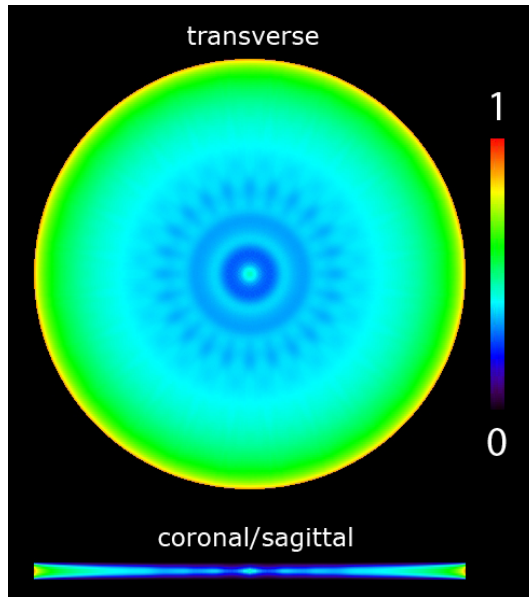


Figure 7.20: System matrix for MADPET-3 based on the DRF model. The top view shows the sensitivity map of the transverse plane, the bottom view the sensitivity plots of the coronal and sagittal plane which are identical due to the scanners symmetries. All plots are normalized to the same maximum value.

During the first performance tests with MADPET-3, one SiPM of Module 1 showed a much higher current drain than the other SiPMs of the SiPM array. In one SiPM array with 16 SiPMs in total, all SiPMs in one 1×4 SiPM sub-array are connected to the same cathode. A high current drain in one SiPM will affect the performance of the other three SiPMs within the 1×4 SiPM sub-array. Therefore it was necessary to disable all four SiPMs for data acquisition. Therefore, these SiPMs are considered as dead channels. The four dead channels are located at the edge of the detector modules indicated by the red crystals in figure 7.21, which additionally narrows the FOV that can be used for the objects of interest to $8.75 \times 8.75 \times 4.0 \text{ mm}^3$. But not only the dead channels affect the reconstructed images, also the individual detection efficiency among the SiPMs has to be taken into account in the SM. For that purpose a cylindrical phantom made of plastic filled with $200 \text{ MBq } ^{18}\text{F}$ was measured for 600 seconds. To measure the

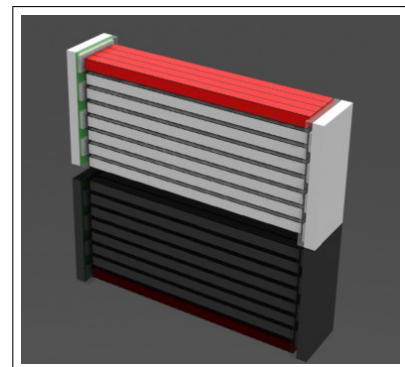


Figure 7.21: One detector module of MADPET-3. The dead channels of this module are indicated by the red crystals.

individual sensitivity of all SiPMs it was not necessary to rotate the source. The cylinder had a diameter of 7 mm and a height of 4 mm covering 80% of the available FOV. The number of counts for each SiPM has been recorded. For the low energy threshold a value of 480 keV and for coincidence window of time of 20 ns was set. Figure 7.22 (a) reflects the number of acquired counts for each SiPM detector for the two modules. The sensitivity has a deviation of 66.67% between the SiPM with the highest counts and the one with the lowest counts. The SiPM with the lowest number of counts (SiPM no.22) was taken as basis for normalization of the corresponding weighting factors. The weighting factors of each SiPM detector are indicated in figure 7.22 (b). The weighting factor for SiPM no.22 was placed to the maximum value 1.00 and all other weights in relation to that value. Figure 7.22 (b) emphasizes that there is a huge variation among the weighting factors for the different SiPMs up to 45.75%.

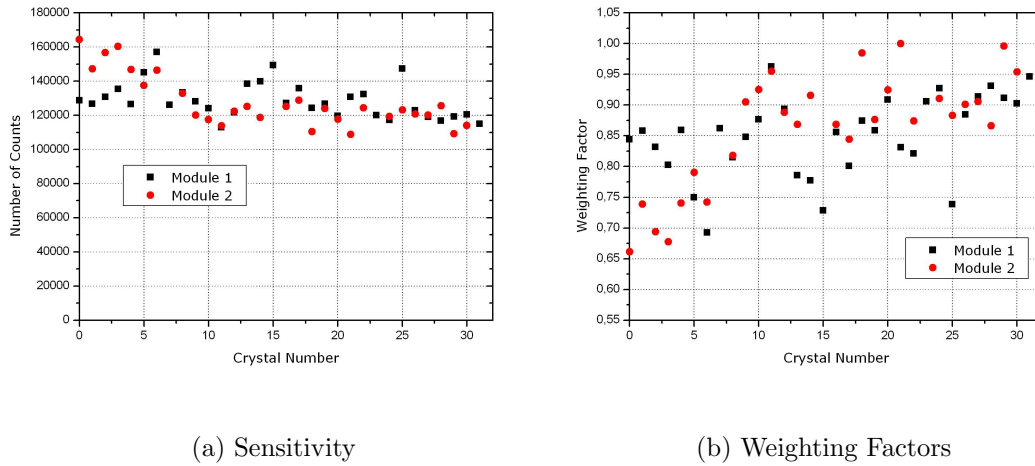


Figure 7.22: (a) Individual number of counts for each SiPM for module 1 (black) and module 2 (red). (b) Weighting factors for MADPET-3 that will be incorporated in the SM. The four dead SiPM are not considered in the plots.

These weighting factors were incorporated into the SM for MADPET-3 according to the following equation:

$$H_{ij}^{new} = H_{ij}^{old} \cdot factor[d_1] \cdot factor[d_2] \quad (7.4)$$

where H_{ij}^{new} and H_{ij}^{old} represent the new and old weights in the SM for voxel j and the LOR i defined by the two detectors d_1 and d_2 . The previous described cylindrical phantom was then scanned for all rotation steps and reconstructed with three different SMs. The first was the originally calculated one not considering any inhomogeneities within the detectors. The other two were taking into account the four dead SiPMs and finally all individual sensitivities from each detector. As the measurement time was 600 seconds for one rotation step, the decay of the used isotope ^{18}F had to be taken into account otherwise the statistics would degrade during the rotation steps and lead to inconsistency. Therefore, the measurement time of each step was slightly increased accordingly to the half life of ^{18}F to maintain an equal number of radioactive decays in each rotation

steps. The required time by the motor to perform one rotation is negligibly short (≈ 3 seconds). Figure 7.23 shows the results after 30 iterations for all three SMs. In the left column of figure 7.23 no corrections were applied in the SM. The reconstructed phantoms contain certain inhomogeneities in activity, especially in a small area on the right edge of the cylinder (see transverse plane of figure 7.23). This inhomogeneity is still present in the reconstructed phantom if the dead detectors are considered in the SM. But in general the cylinder offers a more uniform appearance as e.g. the mean value of the voxels within the phantoms increases (see also table 7.11). Including all detector sensitivities in the SM leads to significant improvement of the uniformity. A slight degradation in sensitivity in an small region on the right edge of the cylinder is still noticeable but certainly less distinguished. For quantitative comparison between the three SMs the mean value, the variance, the standard deviation as well as the maximum and minimum value within the reconstructed uniform phantoms are presented in table 7.11. As region of interest a volume slightly smaller the whole cylinder (diameter 6 mm, height 3 mm) was used for the analysis.

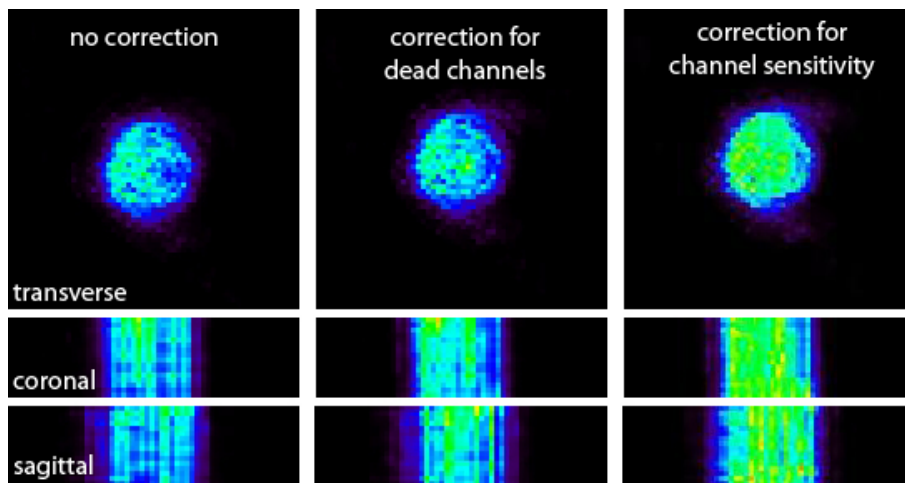


Figure 7.23: Reconstructed uniform phantom for MADPET-3. Left column: No additional correction was considered in the SM. Center column: Dead channels were taken into account for the SM. Right column: Dead channels and the individual detection efficiency were considered in the SM. All plots are normalized to the same maximum value. Results are shown after 30 iterations.

Table 7.11: This table summarizes the mean value, the variance, the standard deviation, the minimum and maximum values for the reconstructed uniform phantom. As region of interest a volume slightly smaller the whole cylinder (diameter 6 mm, height 3 mm) was used.

MADPET-3	Mean	Var	Std Dev [%]	Min	Max
no corrections	85837.7	$8.11881 \cdot 10^8$	22.84	42290.0	133151.0
dead channels	88297.1	$4.49526 \cdot 10^8$	19.52	36607.9	166362.0
channel sensitivity	117637.0	$3.84399 \cdot 10^8$	16.93	24429.4	344294.0

The main challenge to test the performance achievable with MADPET-3 and the calculated SM was to develop suitable phantoms with small structures that would fit in the small FOV covered by the two detector modules and demonstrate the high resolution. For that purpose different sources were developed: Thin line sources where generated by using a injekt printer [18], [19]. The ink cartridge of a Canon Pixma ip 4200 injekt printer was opened und refilled with 1.0 ml ink and 0.3 ml ^{18}F with an activity of 2 GBq. Several vertical lines where printed as shown in figure 7.24 with thickness of 0.1 mm and distance of 0.9 mm in the center. Every new line towards the edges has a smaller distance of 0.1 mm to the previous one. The distance towards the edges was reduced to 0.5 mm. The same piece of paper has been reprinted with the pattern shown in figure 7.24 100 times in order to put an reasonable about of radioactivity on the small printed structures. After 100 prints an activity of 2.71 MBq was collected in all printed lines.



Figure 7.24: Printed phantom consisting of 11 vertical lines of a thickness of 0.1 mm and a distance of 0.9 mm in the center. The distance towards the edges was reduced by 0.1 mm for each new line down to 0.5 mm. The outer dimensions of the phantom measures $92 \times 56 \text{ mm}^2$.

One problem of printed phantoms is that paper and tape, which is used to fix the phantom in the FOV, are not appropriate materials to stop positrons within their small volume. Therefore a few simulations where performed in order to find out which material and thickness is required to achieve a stopping of positrons within a small volume. Following the printed source in figure 7.24 several scenarios were investigated:

- ◇ A printed phantom with no attenuating materials and a gamma source emitting 2 photons according to the specified activity. The radioactive decay itself was not modelled. Within the GATE software this type of source is indicated by the term back-to-back. This scenario was chosen to identify what kind of results are to be expected under ideal conditions.
- ◇ A printed phantom with all the materials around the source. The paper was defined by the chemical compounds of cellulose ($\text{C}_6 \text{H}_{10} \text{O}_5$) and the tape was defined by the properties of polypropylene (PP) ($\text{C}_3 \text{H}_6$). The thickness of the paper was assumed as 0.1 mm and the layer of PP a thickness of 1.0 mm. A positron source with all the properties of ^{18}F source was modelled.
- ◇ A printed phantom with all the materials around the source and additionally a thin layer (thickness 1 mm) of Aluminium or Copper was defined and the paper and tape was put in between.

The printed phantom was simulated by 8 lines with a thickness of 0.5 mm and a length of 8.0 mm. The distance between each line measured 1.0 mm from the center point of one line to the next one. This geometry represents the maximum spatial resolution that can theoretically be achieved with MADPET-3. The simulation was also used to study if

the spatial resolution degrades towards the edges of the FOV e.g. due to parallax errors caused by the long crystals. For each simulation a total run time of 60 seconds was set, the activity was put to 2.0 MBq, and the low energy threshold to 400 keV. The list of single events was sorted in time and sorted in coincidences. The coincidences time windows was 20 ns. The single events were reconstructed by an ML-EM reconstruction algorithm and a pre-calculated SM based on the DRF model.

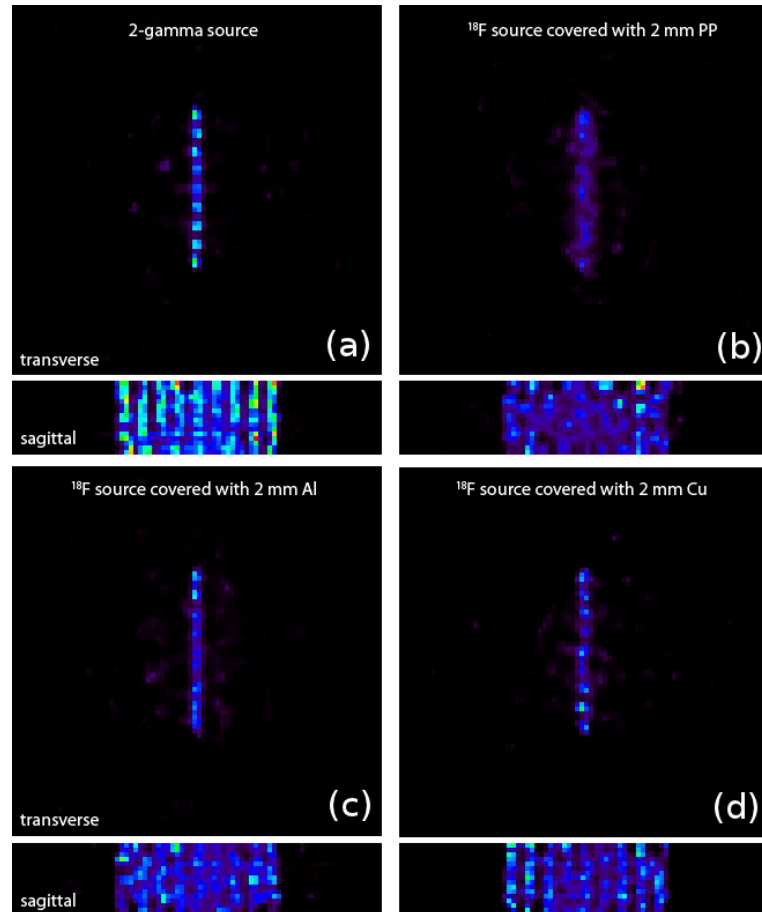


Figure 7.25: Simulated printed phantom with different simulation set-ups: (a) Pure gamma source emitting two photons accordingly to the activity. No attenuating materials nor the radioactive decay was modelled. (b) ^{18}F source with a 1.0 mm layer of polypropylene on the front and back side of the paper was defined as attenuating media. (c) ^{18}F source with a 1.0 mm layer of polypropylene and 1.0 mm layer of Aluminium on the front and back side of the paper. (d) ^{18}F source with a 1.0 mm layer of Copper instead of Aluminium. All the plot are normalized to the same maximum value

In figure 7.25 the results after 30 iterations are presented. For the pure gamma source all lines of the source can be clearly separated in the images (figure 7.25 (a)). Whereas for the ^{18}F source with a 1.0 mm layer of polypropylene on the front and back side of the paper none of the lines could be distinguished (figure 7.25 (b)). Adding an additional layer of Aluminium or Copper the nine lines are observable again. Due to the higher Z value of Copper, this material has a higher stopping capability for positrons and leads therefore to a better separation of the different lines. After these considerations the printed line phantom as shown in figure 7.29 was measured with a 1.0 mm thick layer

of Copper on each side of the paper. Images were reconstructed with an iterative ML-EM reconstruction algorithm and a SM based on the DRF model. The results after 30 iterations are presented in figure 7.26. Figure 7.26 (a) reflects the transverse and sagittal view and figure 7.26 (b) the corresponding line profile through the center plane. 8 of the 11 printed lines can be separated as seen in the line profile. The three missing lines may be lost due to misalignment in the positioning of the phantom in the FOV and therefore located outside the FOV.

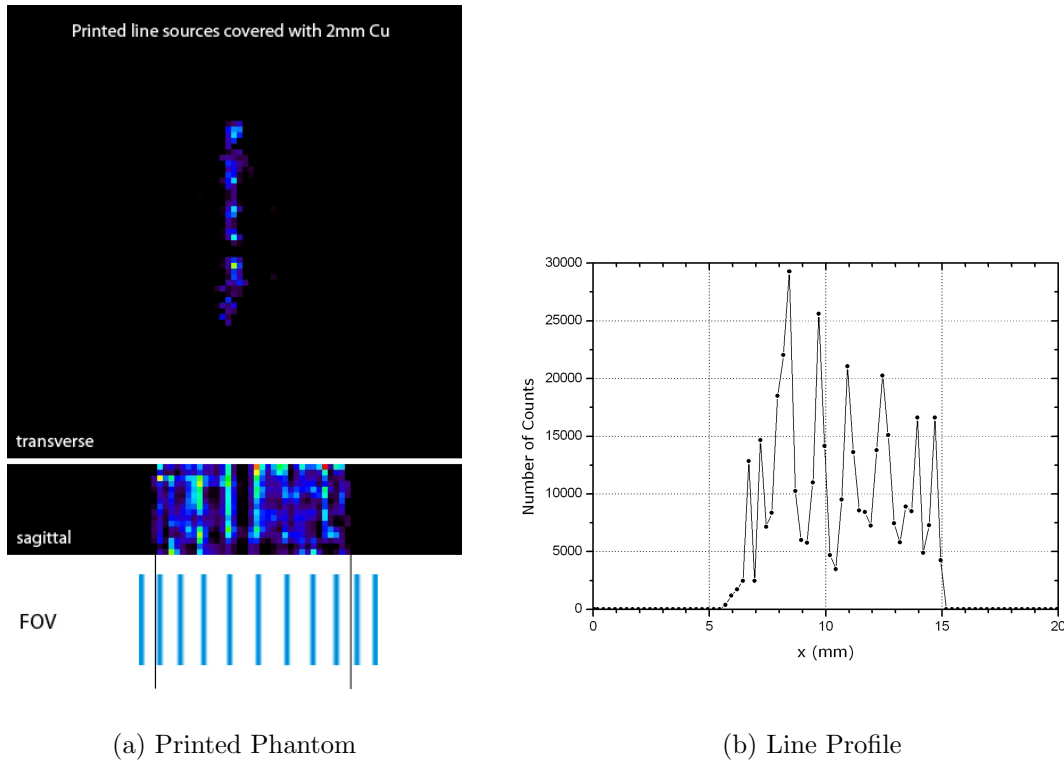


Figure 7.26: (a) Reconstructed images of the printed line phantom for the transverse and sagittal plane after 30 iterations. (b) Corresponding line profile through the central slice in the transverse plane. Since the FOV cross section (8.5×4.0 mm) is smaller than the phantom dimensions (92×56 mm²), one expects a maximum of 8 lines in the image, which can be separated.

Another possibility to generate small structures that can be used as phantom for MADPET-3 could be realized by building phantoms with Alginate. Alginate or Alginic acid is an anionic polysaccharide produced by brown algae and bacteria. Through binding water it forms a viscous gum. In extracted form it absorbs water quickly and is capable of absorbing 200 to 300 times its own weight in water [20]. Alginates are useful for the productions of micro- or nanostructures and therefore widely used for medical applications. Due to gelation in the presence of divalent cations such as Ca^{2+} it is possible to build small 3D structures [21]. Three Alginate spheres were produced by extruding small amounts of alginate through a syringe. The activity concentrated in of three spheres was 5.0 MBq in total. Data was acquired for 240 seconds for each projection. A low energy threshold of 480 keV and a coincidence time window of 20 ns were applied. The reconstructed images of the transverse, coronal and sagittal planes are presented in figure 7.27. Applying a Gaussian fit to the Alginate spheres leads to values of 1.19, 1.05

and 1.12FWHM. Due to the ductile structure of the Alginate spheres their actual size is hard to determine. According to the values given by the Gaussian fit their size can be estimated to be below 1.5 mm in diameter.

As last option to estimation of the spatial resolution that can be achieved with MADPET-3 measurements were performed with three injection needles. Two syringes were filled with ^{18}F -FDG which was extruded through the needles. Small amounts of ^{18}F -FDG are assumed to remain in the small cannulas of the needles. The needles were removed from the syringes and assembled together with a third empty needle to retain a certain distance between the two filled one. The outer diameter of a needle was measured to 0.36 mm. The distance from the center point of one needle filled with radioactivity to the next filled one is approximately 0.72 mm. The activity in the two needles was 0.1 MBq. Therefore, a long measurement time of 600 seconds for each rotation step was needed. The reconstructed image and the corresponding line profile through the central plane is shown in figure 7.28. Obviously the second needle was not complete filled with radioactivity showing a gab in the middle which does not contain any accumulation of activity in the image. As the two needles can be clearly separated the spatial resolution of MADPET-3 can be assumed to be less than 1.0 mm.

The results of all three developed and analysed phantoms, the printed line source, the Alginate spheres and the needles showed that the spatial resolution of MADPET-3 can be assumed to be less than 1.0 mm.

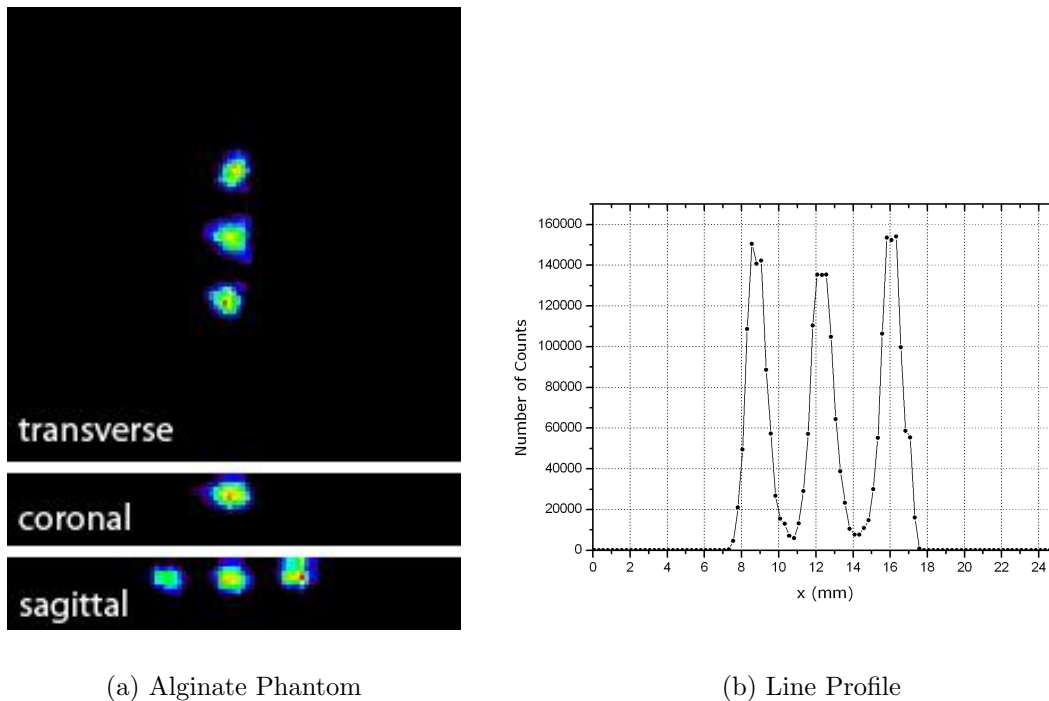
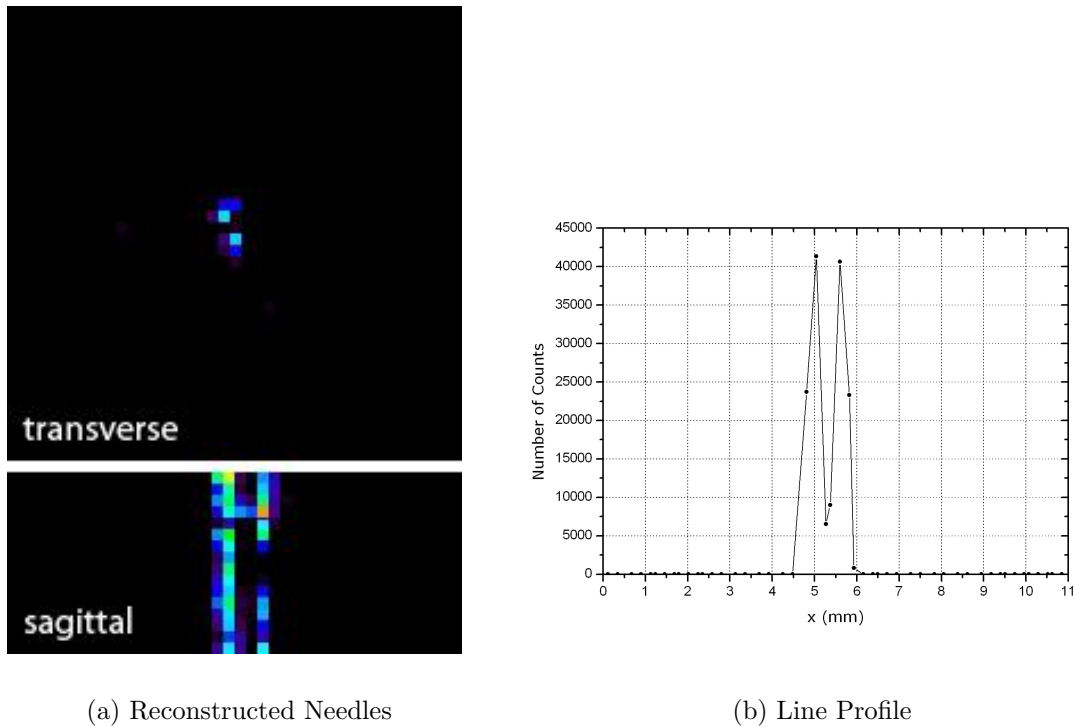


Figure 7.27: (a) Reconstructed images of the three Alginate spheres for the transverse, coronal and sagittal plane. (b) Corresponding line profile through the central slice in the transverse plane. The line profile allows to estimate the relative position and size of the spheres.



(a) Reconstructed Needles

(b) Line Profile

Figure 7.28: (a) Reconstructed images of the two needles for the transverse, coronal and sagittal plane. (b) Corresponding line profile through the central slice in the transverse plane. The line profile allows to estimate the relative position and size of the needles.

Parallax Effect

In order to estimate how well the quite extreme crystal geometry is incorporated in the proposed DRF, another SM was generated in which the crystal length of 20 mm was not taken into account. This SM was based on simple solid angle calculations considering only the coordinates of one front surface ($1.0 \times 1.0 \text{ mm}^2$) for defining the appropriate LOR. Also the intersection lengths of a gamma ray crossing a crystal is not included in the calculation of the corresponding weights of the SM. The possible effects of such a SM may become only distinctive for phantoms extending towards the edges of the FOV. As the FOV with two detector modules is probably too small for studying these effects a phantom covering a larger area of the FOV was simulated. 23 rods with a diameter of 0.5 mm each and a distance from center to center of 1.5 mm were modelled. Simulation run time was set to 60 seconds and a low energy threshold of 400 keV was applied together with a 13 ns coincidence time window. In the simulation a complete ring of 24 detector modules was generated to estimate how good the parallax effect can be reduced by the DRF model. This effect may only occur for oblique angles between two detectors which is not the case for two opposite detector modules as in the MADPET-3 demonstrator. Therefore, a whole detector ring was modelled. Reconstruction was performed with a SM based on the DRF model and with a SM based on solid angle calculations. The resulting images are presented in figure 7.30 after 50 iterations and the corresponding line profiles through the center plane are shown in figure 7.31.

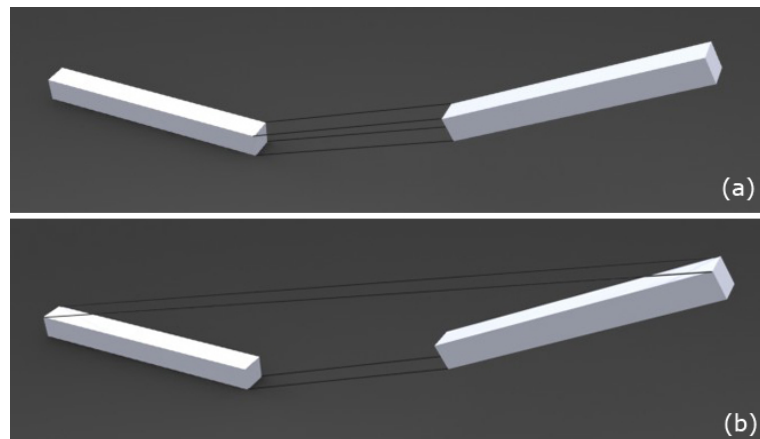


Figure 7.29: (a) LOR between two crystals if the crystal length and therefore intersection point for the deposited photons within the crystal is not considered in the reconstruction. The LOR is defined by the 8 vertices at the front side-face of the two crystals. (b) The LOR is defined by the maximum volume that can be built between two crystals. The whole length of the crystal is considered in the SM and the reconstruction.

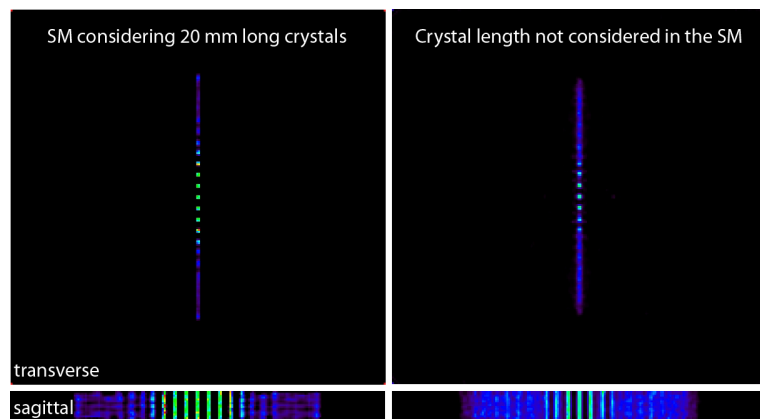


Figure 7.30: Left: Reconstructed phantom with a SM where the crystal geometry is included in the DRF model. Right: Reconstructed phantom for which the crystal length was not taken into account.

Applying a SM, where the crystal length is not considered only 7 of the 23 rods in total can be separated in the reconstructed images. The remaining rods can not be distinguished. Whereas with the DRF model based SM 14 rods can be separated in the images.

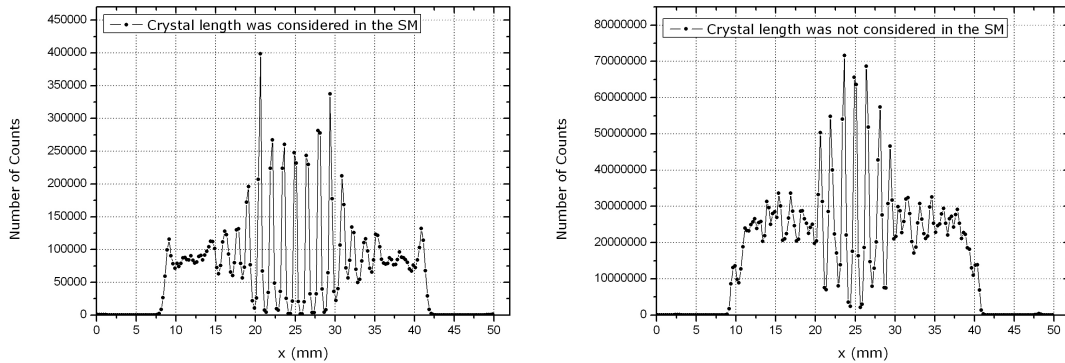


Figure 7.31: Line profiles through the central slice of the transverse plane for the simulated phantom. Left: If the crystal geometry is included in the SM, 14 from 23 rods in total can be separated. Right: Using a SM based on solid angle calculations only 7 rod can be separated.

7.3 Results for MADPET

As described in chapter 6 SMs were generated for the MADPET scanner based on the DRF model, based on MC simulations and based on point source measurements. For all the SMs a voxel grid of $30 \times 30 \times 1$ voxels with a voxel size of $1.85 \times 1.85 \times 1.85 \text{ mm}^3$ was used. For the calculations based on the DRF model the integral precision was set to a value of 60. The resulting sensitivity maps for the three SMs in two dimensions are shown in figure 7.32. Additionally, the requirements needed for the generation of the different SMs and the size of the SM are summarized in table 7.12. The value given for the computational time needed for the SM based on point source measurements represents only the time for the calculation and data processing, the measurement time for the various point source positions is not included. Regarding the storage requirements and the computational time the DRF model seems to be advantageous compared to the other two methods.

Table 7.12: This table summarizes the requirements needed for the generation of the different SMs and the size of the SM. The value given for the computational time needed for the SM based on point source measurements represents only the time for the calculation and data processing, the measurement time for the various point source positions is not included.

	DRF model	MC simulation	Point source measurements
Size of the SM	14.6 MB	27.1 MB	52.7 MB
Storage requirements	14.6 MB	200 GB	2.0 TB
Computational time	10 min	3 weeks	3 weeks

All three sensitivity matrices obtain similar loop-like structures and a few internal rings due to the number of detector modules and the dead space between them. An important aspect that has to be considered for the SM based on point source measurements, is the extended size of the point source. The small point source with a diameter of 0.5 mm is embedded in a small capsule of plastic measuring $3 \times 3 \times 8 \text{ mm}^3$. Due to the positron range

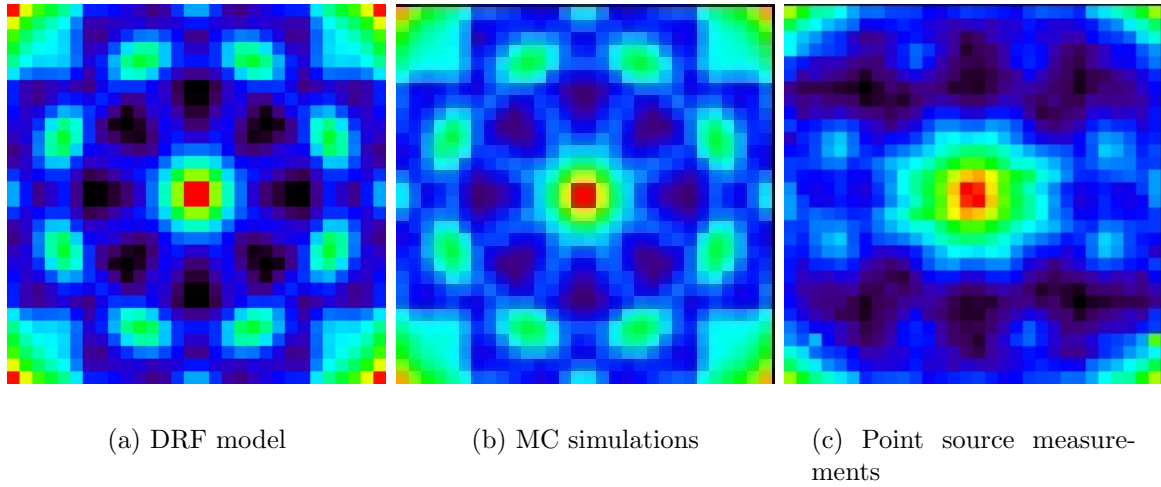


Figure 7.32: Generated SMs for MADPET: (a) SM analytically calculated with the DRF model, (b) SM based on MC simulations, (c) measured SM with a point source. For all three cases a $30 \times 30 \times 1$ voxel grid and a voxel size of $1.85 \times 1.85 \times 1.85 \text{ mm}^3$ was used.

in plastic the actual size of the source is broadened by the surrounding material. This is a limitation for the applicability of this method as the point source has to be smaller than the voxel size used for the reconstruction. This may explain why the sensitivity matrix generated with point source measurements is not perfectly symmetric as for the ones based on MC simulations and on the DRF model.

For two different phantoms similar to the ones used in the Gate simulation described in chapter 7.1 measurement data was acquired and reconstructed with the different SMs.

A Derenzo-like phantom was measured consisting of five rods with diameters of 5.0, 4.5, 3.5, 2.5 and 1.5 mm and a height of 8.6 mm as shown in figure 7.33. The phantom was filled with ^{18}F with an activity of 5 MBq. Data was acquired for 120 seconds per rotation step. The results after 30 iterations with an ML-EM reconstruction algorithm are presented in figure 7.34. For all the studied cases each rod was fitted with a Gaussian and the corresponding FWHM values with their uncertainty are summarized in table 8.12. The smallest rod with a diameter of 1.5 mm has not been considered for the analysis as whose diameter is smaller than the voxel size that was used.

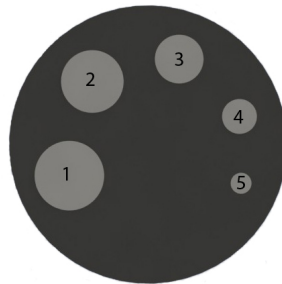


Figure 7.33: Schematic drawing of the measured Derenzo-like phantom consisting of five rods with diameters of 5.0, 4.5, 3.5, 2.5 and 1.5 mm.

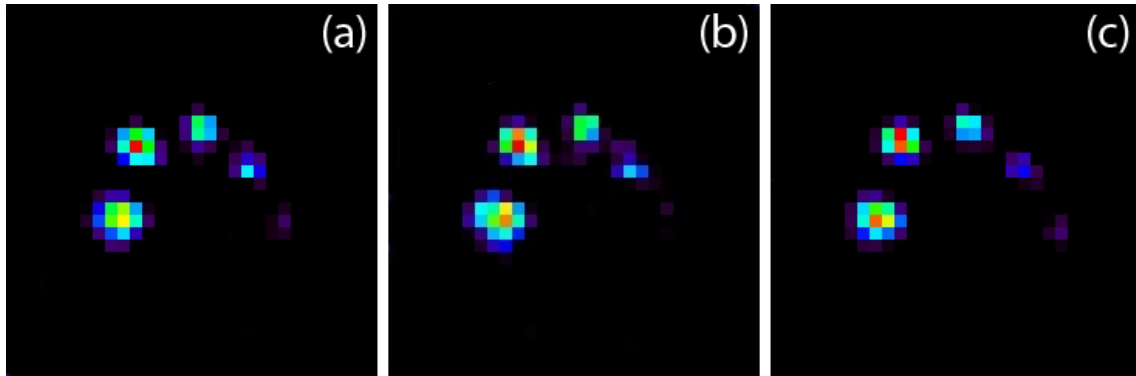


Figure 7.34: Reconstructed Derenzo-like phantom after 30 iterations. (a) Reconstruction with a DRF calculated SM, (b) reconstruction based on a MC generated SM, (c) reconstruction based on the measured SM. For all SMs a voxel grid of $30 \times 30 \times 1$ voxels with a voxel size of $1.85 \times 1.85 \times 1.85 \text{ mm}^3$ was used.

Table 7.13: FWHM values for the reconstructed Derenzo-like phantom. The SMs were generated with three different methods.

System Matrix	DRF	MC	Measurements
1st rod (FWHM)	$5.20 \pm 7.93 \cdot 10^{-6}$	$5.10 \pm 7.93 \cdot 10^{-6}$	$4.98 \pm 5.34 \cdot 10^{-6}$
2nd rod (FWHM)	$4.47 \pm 6.76 \cdot 10^{-6}$	$4.45 \pm 6.76 \cdot 10^{-6}$	$4.43 \pm 4.88 \cdot 10^{-6}$
3rd rod (FWHM)	$3.60 \pm 5.72 \cdot 10^{-6}$	$3.58 \pm 5.72 \cdot 10^{-6}$	$3.60 \pm 2.24 \cdot 10^{-5}$
4th rod (FWHM)	$2.50 \pm 1.17 \cdot 10^{-5}$	$2.48 \pm 1.17 \cdot 10^{-5}$	$2.54 \pm 2.04 \cdot 10^{-5}$

Additionally a cylindrical phantom was reconstructed with the three different SMs to represent the uniformity. The uniform phantom with a diameter of 33.0 mm and a height of 7.4 mm was homogeneously filled with an aqueous solution of ^{18}F with an activity of 40.0 MBq. The results after 30 iterations with an ML-EM reconstruction algorithm are shown in figure 7.35 together with the corresponding values for the variance and standard deviation for a region of interest covering 90 % of the uniform phantom summarized in table 7.13.

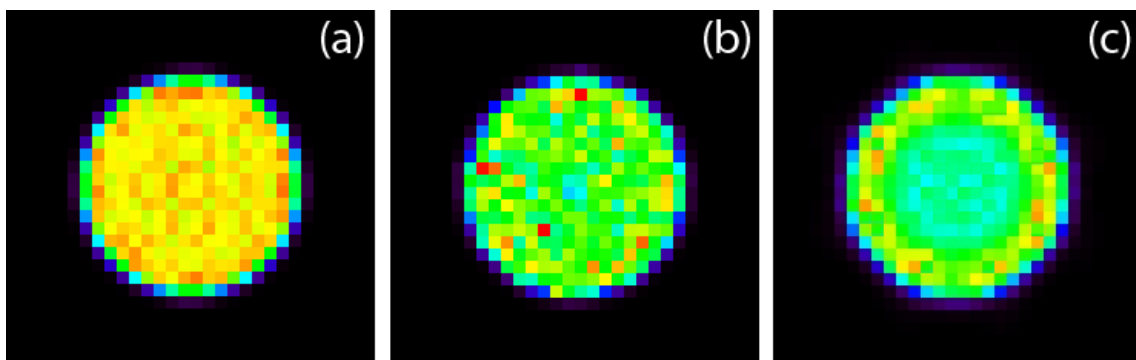


Figure 7.35: Reconstructed uniform phantom after 30 iterations. (a) Reconstruction with a DRF calculated SM, (b) reconstruction based on a MC generated SM, (c) reconstruction based on the measured SM. For all SMs a voxel grid of $30 \times 30 \times 1$ voxels with a voxel size of $1.85 \times 1.85 \times 1.85 \text{ mm}^3$ was used.

A line profile for the reconstructed uniform phantom through the central slice is presented in figure 7.36 for all three different SMs. The number of counts is noticeable higher for the reconstructed uniform phantom with a DRF model based SM.

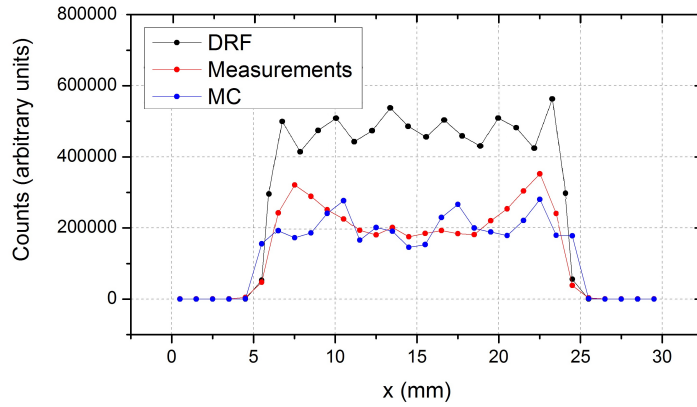


Figure 7.36: Line profiles through the central slice of the reconstructed uniform phantom for three different SMs.

Table 7.14: This table summarizes the mean value, the variance, the standard deviation, the minimum and maximum values for the reconstructed uniform phantom. As region of interest a volume covering 90 % of the whole cylinder was used.

Data Set	Mean	Var	Std Dev [%]	Min	Max
DRF Model	472559	$1.27 \cdot 10^9$	9.65	387964	579396
MC Simulations	207833	$1.38 \cdot 10^6$	12.85	121027	329396
Measurements	238618	$3.62 \cdot 10^6$	15.23	175297	446106

The DRF model allows re-calculation of a SM within a short time to change certain parameters that cannot be addressed that easily in a simulation or measurement. Another SM was computed with a finer voxel grid of $60 \times 60 \times 1$ voxels and a corresponding voxel size of $0.925 \times 0.925 \times 0.925 \text{ mm}^3$ with the DRF model. The new sensitivity matrix is presented in figure 7.37 in comparison to the originally used voxel grid of $30 \times 30 \times 1$ and a voxel size of $1.85 \times 1.85 \times 1.85 \text{ mm}^3$. By doubling the number of voxels also the size of the SM and the computational time were increasing from xxx to xxx.

The phantoms were re-reconstructed with the new SM. The images are presented after 30 iterations in figure 7.38 and 7.39. The overall image quality is better when using a SM considering a finer voxel grid. Due to smaller voxel size for a SM with a voxel grid of $60 \times 60 \times 1$ the shape of the rods appears more spherical. All rods were fitted by a Gaussian curve and the corresponding values for the FWHM are listed in table 7.12. The values for the Gaussian fit are in good agreement with the dimensions of the rods. It was possible to include the smallest rod with a diameter of 1.5 mm which was not the case for the $30 \times 30 \times 1$ voxel grid. Values for the variance and standard deviation for a region of interest covering 90 % of the uniform phantom are summarized in table 7.16. Also the

reconstructed uniform phantom provides an improvement in terms of image quality and homogeneity.

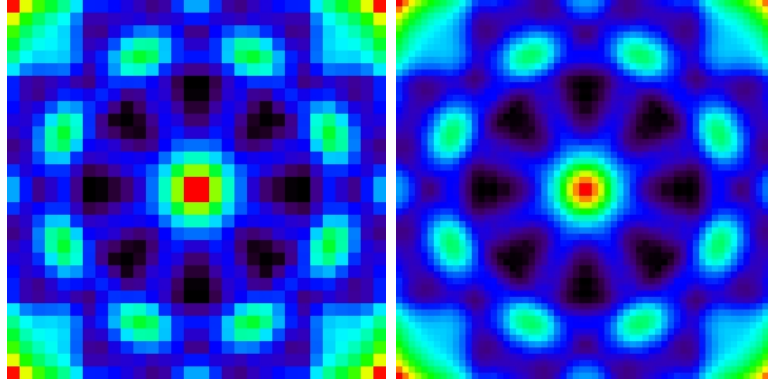


Figure 7.37: Generated SMs for MADPET based on the DRF model. Left: SM with a $30 \times 30 \times 1$ voxel grid and a voxel size of $1.85 \times 1.85 \times 1.85 \text{ mm}^3$. Right: SM with a finer voxel grid of a $60 \times 60 \times 1$ voxel grid and a voxel size of $0.925 \times 0.925 \times 0.925 \text{ mm}^3$. The plots are normalized to the same maximum value.

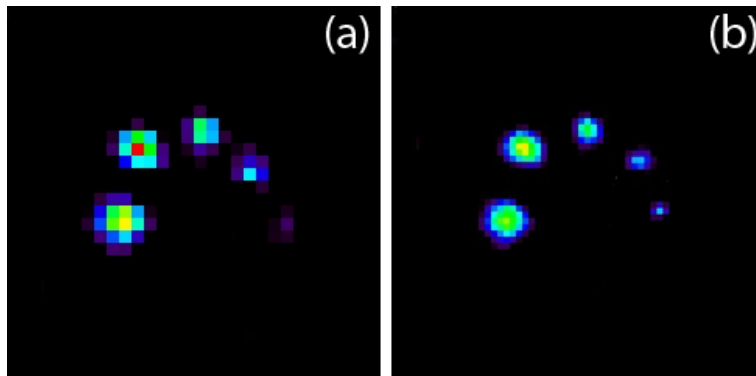


Figure 7.38: Reconstructed Derenzo-like phantom after 30 iterations. (a) Reconstruction with a DRF calculated SM with a voxel grid of $30 \times 30 \times 1$ voxels with a voxel size of $1.85 \times 1.85 \times 1.85 \text{ mm}^3$, (b) reconstruction with a DRF calculated SM with a voxel grid of $60 \times 60 \times 1$ voxels with a voxel size of $0.925 \times 0.925 \times 0.925 \text{ mm}^3$.

Table 7.15: FWHM values for the reconstructed Derenzo-like phantom. Values are given for a SM calculated with the DRF model with two different voxel grids and voxel sizes.

Voxel Grid	$30 \times 30 \times 1$	$60 \times 60 \times 1$
Voxel Size	$1.85 \times 1.85 \times 1.85 \text{ mm}^3$	$0.925 \times 0.925 \times 0.925 \text{ mm}^3$
1st rod (FWHM)	$5.20 \pm 7.93 \cdot 10^{-6}$	$5.10 \pm 7.93 \cdot 10^{-6}$
2nd rod (FWHM)	$4.47 \pm 6.76 \cdot 10^{-6}$	$4.45 \pm 6.76 \cdot 10^{-6}$
3rd rod (FWHM)	$3.60 \pm 5.72 \cdot 10^{-6}$	$3.58 \pm 5.72 \cdot 10^{-6}$
4th rod (FWHM)	$2.50 \pm 1.17 \cdot 10^{-5}$	$2.48 \pm 1.17 \cdot 10^{-5}$
5th rod (FWHM)	not analysed	$1.42 \pm 7.47 \cdot 10^{-6}$

Table 7.16: This table summarizes the mean value, the variance, the standard deviation, the minimum and maximum values for the reconstructed uniform phantom. As region of interest a volume covering 90 % of the whole cylinder was used.

Voxel Grid	Mean	Var	Std Dev [%]	Min	Max
$30 \times 30 \times 1$	472559	$1.27 \cdot 10^9$	9.65	387964	579396
$60 \times 60 \times 1$	212531	$6.10 \cdot 10^7$	3.68	191155	237961

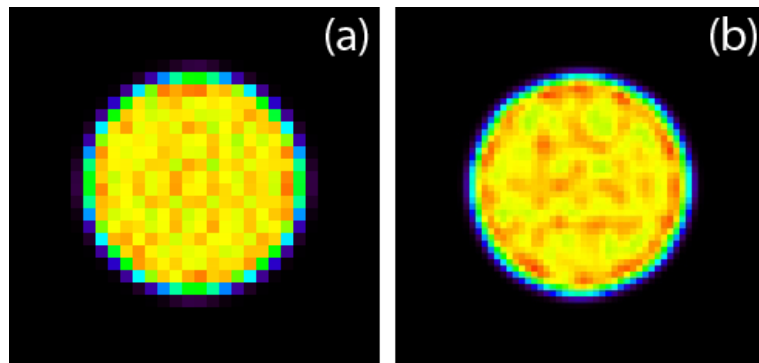


Figure 7.39: Reconstructed uniform phantom after 30 iterations. (a) Reconstruction with a DRF calculated SM with a voxel grid of $30 \times 30 \times 1$ voxels with a voxel size of $1.85 \times 1.85 \times 1.85 \text{ mm}^3$, (b) reconstruction with a DRF calculated SM with a voxel grid of 60×60 voxels with a voxel size of $0.925 \times 0.925 \times 0.925 \text{ mm}^3$.

References

- [1] GATE: GEANT4 APPLICATION FOR TOMOGRAPHIC EMISSION, <http://www.opengatecollaboration.org/>
- [2] C. MOISAN, F. CAYOUILLE, AND G. McDONALD, *DETECT2000, The Object Oriented C++ Language Version of DETECT*, Laval University, Quebec, Canada, Version 5.0, 2001
- [3] J.S. KARP ET. AL., *Performance Standards in Position Emission Tomography*, J. Nucl. Med. vol. 12, no. 32, pp. 2342-2350, 1991
- [4] M.N. WERNICK AND J.N.AARSVOLD; *EMISSION TOMOGRAPHY: The Fundamentals of PET and SPECT*, Elsevier Acad. Press, ISBN 0-12-744482-3, pp. 71-73, 2004
- [5] ROOT, *A data analysis framework*, <http://root.cern.ch/>
- [6] MPPC - MULTI PIXEL PHOTON COUNTER, data sheet, <http://sales.hamamatsu.com/de/produkte/solid-state-division/si-photodiode-series/mmpc.phc>
- [7] R. MAIER, HAMAMATSU PHOTONICS, Personal conversation, September 2009.
- [8] A. VELROYEN, *Development of a Novel Detector Module for PET/MR Imaging Based on SiPMs and Fast Scintillation Crystals*, Diploma Thesis in Physics, Fakultät für Physik, Ludwig-Maximilians-Universität München, Munich, Germany, 2010
- [9] SAINT-GOBIN CRYSTALS, PreLude 420 Data sheet
- [10] J. PULKO, *A Monte Carlo Model of a Silicon Photomultiplier*, PhD Thesis, Physics Department E18, Technische Universität München, Munich, Germany, 2012
- [11] P. PEDRON, *Implementation of an analytical 3D model for generation the system matrix of a PET scanner*, Bachelor Thesis in Informatics, Technische Universität München, Munich, Germany, 2009
- [12] S.I. ZIEGLER, B.J. PICHLER, G. BOENING, M. RAFECAS, W. PIMPEL, E. LORENZ, N. SCHMITZ, AND M. SCHWAIGER, *A Prototype High-resolution Animal Positron Tomograph with Avalanche Photodiode Arrays and LSO-Crystals*, Eur. J. Nucl. Med. Mol. Img., 28(2), pp. 136-143, 2001
- [13] I. TORRES ESPALLARDO, *Image Reconstruction and Correction Methods for MADPET-II based on Monte Carlo Techniques*, PhD Thesis in Physics, Departament de Física Atòmica, Molecular y Nuclear, Universitat de València, València, Spain, 2009
- [14] K.P. Schäfers, A.J. READER, M. KRIENS, C. KNOESS, O. SCHOBER, M. SCHÄFERS, *Performances Evaluation of the 32-Module quadHIDAC Small-Animal PET scanner*, J. Nucl. Med., vol. 46, pp. 996-10024, 2006

-
- [15] R. LECOMTE, *Technology challenges in small animal PET imaging*, Nucl. Instr. Meth., vol. A 527, pp. 157-165, 2004
- [16] Y. YANG, S.R. CHERRY, *Observations Regarding Scatter Fraction and NEC Measurements for Small Animal PET*, IEEE Trans. Nucl. Sci., vol. 53, pp. 127-132, 2006
- [17] W. LEHNERT, S.R. MEIKKE, D.F. NEWPORT, *Count Rate Performance of the MicroPET Focus 220 Animal Scanner in Singles Transmission Scanning Mode*, IEEE Trans. Nucl. Sci., vol. 55, pp. 2493-2500, 2008
- [18] R. SCAFÈ, P. BENNATI, P. AUER, L. LA PORTA, F. PISCANE, M. NERINA CINTI, R. PELLEGRINI, G. E. VINCENTIS, G. CONTE AND R. PANI, *Multi-printed Inkjet Phantoms for Radionuclide Molecular Imaging*, IEEE NSS MIC Conf. Record, N02-295, pp. 1081-1087, 2008
- [19] J.A. VAN STADEN, H. DU RAAN, M.G. LÖTTER, A. VANS ASWEGEN AND C.P. HERBST, *Production of radioactive quality assurance phantoms using a standard inject printer*, Phys. Med. Bio., vol. 52, pp. 329-337, 2007
- [20] R.C. ROWE, *Adipic Acid*, Handbook of Pharmaceutical Excipients, RPS Publishing, ISBN 978-0-85369-792-3, 2009
- [21] B.H.A. REHM, *Microbial Production of Alginate: Biosynthesis and Applications*, Microbial Production of Biopolymer Precursors, Caister Academic Press, ISBN 978-1-904455-36-3, 2009
- [22] F. R. SCHNEIDER, *Setup and Commissioning of a Positron Emission Tomograph for a Student's Advanced Laboratory Course*, Master Thesis in Engineering Physics, Technische Universität München, Munich, Germany, 2009

Chapter 8

Summary and Outlook

THE first commercial PET/MR whole body system with simultaneous PET and MRI imaging is the Biograph mMR [1] by Siemens (Munich, Germany) which uses block detectors with APDs. The use of SiPMs in a fully integrated PET/MRI whole body scanner has not been realized so far but are currently being tested [2]. SiPM are a promising detector concept for combined PET/MRI scanners as they operation in high magnetic fields was proven feasible and as they are offering many properties which makes them advantageous compared to APDs [3]. The aim of this work was to develop a small animal PET prototype scanner based on SiPM offering a high spatial resolution (below 1 mm) and a high sensitivity. With respect to both requirements a quiet extreme geometry for the scintillation crystals has been chosen. For the MADPET-3 prototype scanner LYSO scintillation crystals measuring $1.0 \times 1.0 \times 20.0 \text{ mm}^3$ were coupled with one-to-one correspondence to two SiPM arrays.

Many simulation studies were undertaken in this work to investigate the light collection in this needle-like scintillation crystals. According to the simulations the best light collections can be achieved with a diffuse white reflector which was defined as a ground crystal surface covered with a high reflecting material within the DETECT2000 simulation software package. A slightly worse results for the light collection were observed for a polished crystal surface covered with a specular reflector. It was also observed that the light collection is more efficient if an air gap is left between the scintillator and the reflector. The predominance of diffuse reflecting materials such as Teflon, Barium sulphate over specular ones can also be found in [4], [5] and [6], but all of them require a certain thickness of the layer with which the scintillation crystals would have to be covered in order to achieve an reflection coefficient. For a reflection coefficient of 97% with Barium sulphate a layer with a thickness of 0.5 mm is needed [7]. This requirement implicits certain limitations for building highly dense PET detector modules with many crystals and tiny gaps between them. The DETECT2000 software packages offers another model for a diffuse surface with is denoted as a "paint" surface which should offer the properties of a diffuse white painted surface as Barium sulphate. During the simulation studies this painted surface resulted in light collection efficiency far below the ones achieved with a polished or ground surface. This may indicated that the model implemented in the DETECT2000 is properly not accurate enough to represent a white diffuse reflector. Additionally the thickness of the painted layer is also not incorporated in the model which defines the properties of the diffuse paint.

Apart from the light collection in a single LYSO crystal, the light collection and distribution was simulated for a detector module to estimate the module performance.

The common and relatively thick layer of epoxy for each 1×4 SiPM sub-array turned out to be the most critical part for the individual crystal readout in terms of light crosstalk within the module. Even for a slightly decrease in thickness the light collection would benefit from. One possibility to overcome this problem would be to apply trenches in the epoxy layer between the SiPMs for better separation. In these trenches the light could be absorbed or trapped before reaching the neighbouring detector. With the trenches also the crosstalk between the signals from two neighbouring SiPM detectors could be suppressed.

The Simulations performed with GATE provided valuable insights into severity effects such as inter-crystal scatter due to the crystal geometry and scattering affected by the alternating FSR and BSR. The influence of inter-crystal scatter for BSR was found to be negligible. The simulations showed that the fraction of inter-crystal scattered events can successfully be suppressed by applying a low energy threshold of 400 keV. The advantages of suppressing inter-crystal scattering comes at the cost increasing the sensitivity. For the proposed SiPM detector modules two possible designs for whole a small animal system were simulated with GATE. This delivered valuable insights to estimate the possible performance characteristics and limitations. System matrices were calculated for each geometry allowing to perform reconstructions with simulated phantoms. For the system matrices an analytical DRF model proposed by [8] was implemented on a Linux cluster architecture. The implementation on a cluster architecture allows to calculate a system matrix within a short computational time and to handle the storage requirements for the possibly huge sizes of a system matrix. The storage capabilities provided by a cluster also offer a fast image reconstruction. Therefore, it was possible to obtain system matrices for MADPET-3 within a time frame of a few days and the finally the reconstructed images after a few minutes with an iterative ML-EM reconstruction code.

As described in chapter 5.2 the small animal PET system MADPET-3 was built consisting of two opposing SiPM detector modules with an alternating FSR and BSR. SM for MADPET-3 was generated for a full detector ring with 24 modules in total. To compensate for the missing modules the measured phantoms were rotated. To test the performance achievable with MADPET-3 and the calculated SM appropriate phantoms were built with small structures that would fit in the small FOV covered by the two detector modules. The spatial resolution was estimated to be in the range between 0.5 mm and 1.0 mm. The SM for MADPET-3 was complemented by an additional measurement providing information over the individual sensitivity of each detector. For larger phantoms such as the uniform filled cylinder covering 90% of the FOV, the effect of the individual detector sensitivities can not be neglected to maintain an artefact free image.

In order to estimate how well the quite extreme crystal geometry is incorporated in the proposed DRF, another SM was generated in which the crystal length of 20 mm was not taken into account. This SM was based on simple solid angle calculations considering only the coordinates of one front surface for defining the appropriate LOR. Also the intersection lengths of a gamma ray crossing a crystal is not included in the calculation of the corresponding weights of the SM. To study the parallax effect a phantom consisting of 23 rods with a diameter of 0.5 mm each and a distance from center to center of 1.5 mm was simulated. In the reconstructed images obtained with a SM based on solid angle calculations only 7 of the 23 rods in total can be separated whereas with a SM based on the DRF model 14 rods can be separated. These results show that a SM calculated with the DRF model can improve the degradation by the parallax effect better than a SM based

on solid angle calculations.

A validation for the DRF model was accomplished by comparison with two other SMs that have been generated by MC simulation and based on point source measurements for each voxel of the field of view. The comparison of the different SMs was done with the predecessor model MADPET, as MADPET-3 consists only of two detector modules not allowing to measure the complete SM for each voxel with a point source. As MADPET is a sector tomograph not covering a full detector ring all scanned phantoms and sources have to be rotated as for MADPET-3. Therefore, also the voxel grid used for the point source measurements required by the SM had to be rotated. For that purpose the main challenge was to rotate the voxel grid during the point source measurements in the same way as data is acquired during a measurement of a phantom and to sort, analyse and store the point source measurement data in a appropriate way.

Several phantoms were reconstructed for MADPET with the three different SMs leading to similar results in terms of spatial resolution, homogeneity and image quality in general. With regard to the storage requirements and the computational time needed by the generated SMs with MC simulations and with point source measurements, the DRF model seems to be a reasonable alternative. Additionally, the DRF model offers to re-calculated a SM within a sort time to change or modify certain parameters of interest.

Additionally SM was computed for a finer voxel grid of $60 \times 60 \times 1$ voxels and a corresponding voxel size of $0.925 \times 0.925 \times 0.925 \text{ mm}^3$ with the DRF model. The Derenzo-like and the uniform phantom were re-reconstructed with this new SM. The overall image quality was better in both cases. For the Derenzo-like phantom the shape of the rods appears more spherical and also the smaller could be resolved correctly which was not possible using a SM with a $30 \times 30 \times 1$ voxel grid. The reconstructed uniform phantom offered a higher homogeneity.

At good compromise between the huge storage requirements required by point source measurements and the relatively fast computation of a SM with the DRF model could be realized by combining both methods. One could think of performing point source measurements not over the whole FOV but for a certain limited number of voxels. The missing not measured voxels could then be interpolated by the values given by the DRF model based SM. With that approach also large PET systems can be scanned and analysed, where measurements for each voxel with a point source would not be feasible.

References

- [1] SIEMENS, Biograph mMR, http://www.medical.siemens.com/siemens/en_INT/gg_mr_FBAs/files/multimedia/Biograph_mMR/PET_MR_Applied_Radiology_Supplement.pdf
- [2] HYPERIMAGE, <http://www.hybrid-pet-mr.eu>
- [3] V.C. SPANOUDAKI, A.B. MANN, A.N. OTTE, I. KONOROV, I. TORRES-ESPALLARDO, S. PAUL, AND S.I. ZIEGLER, *Use of Single Photon Counting Detector Arrays in Combined PET/MR: Characterization of LYSO-SiPM Detector Modules and Comparison with a LSO-APD Detector*, J. Instr., 2(12), pp. 0-16, 2007
- [4] S. CHERRY, Y. SHAO, M. TORNAL, S. SIEGEL, A. RICCI, AND M. PHELPS, *Collection of scintillation light from small BGO crystals*, IEEE Trans. Nucl. Sci., vol. 42, pp. 1058-1063, 1995
- [5] T. SMITH, AND B.M. JASANI, *Assessment with various reflectors used with rectangular scintillation detectors*, J. Phys., vol. E 5, pp. 1083-1088, 1972
- [6] A. WIRRWAR, N. SCHRAMM, H. VOSBERG, AND H.-W. MULLER-GARTNER, *Influence of crystal geometry and wall reflectivity on scintillation photon yield and energy resolution*, IEEE NSS Conference Record, pp. 1443-1445, 1999
- [7] W. DÄHN, GIGAHERZ-OPTIK, Personal conversation, February 2008.
- [8] D. STRUL, R.B. SLATES, M. DAHLBOM, S.R. CHERRY, AND P.K. MARDSEN, *An improved analytical detector response function model for multilayer small animal PET scanners*, Phys. Med. Biol., vol. 48, pp. 979-994, 2003

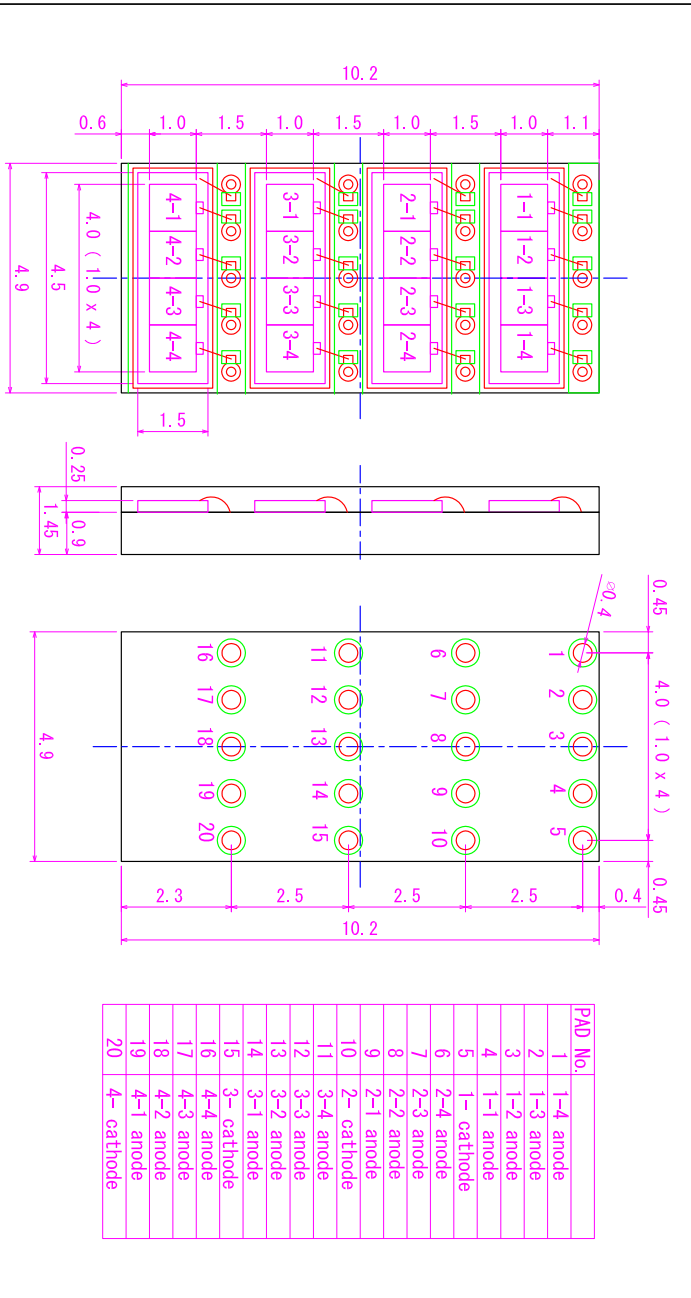
Appendix

Properties of LYSO

Table A.1: Properties of Lutetium Yttrium Oxyorthosilicate

Properties of $\text{Lu}_{1.8} \text{Y}_{0.2} \text{SiO}_5\text{:Ce}$ (LYSO)	
Density [g/ cm ³]	7.1
Hygroscopic	no
Attenuation length for 511 keV [mm]	12
Wavelength of emission maximum [nm]	420
Refractive index at emission maximum	1.82
Decay time [ns]	41
Light yield [photons/MeV]	32 000

SiPM Detector Module



MARK 記号	CONTENTS 記事	DATE 年月日	APPR 承認	CHK 検図	DESIGN 設計	DRAW 製図	REF 備考	UNIT 単位	SCALE 尺度	TITLE 名称	DWG.No. 図番	REV 改訂
	FIRST ISSUE 初発行	2007/12/24						mm	1/1	4ch-MPPCx4-PR3		
								PROJ 三角法		PRELIMINARY		
										HAMAMATSU PHOTONICS K.K.		
										浜松ホトニクス株式会社		

Description and Usage for the DRF-Code and the ML-EM Reconstruction on a Cluster Architecture

The DRF-Code is arranged in seven different folders:

- ◇ bin - Executable programs
- ◇ cfg - Configuration of the scanner geometry
- ◇ in - Folder used for the input files
- ◇ mpi - Hostfile for the mpi
- ◇ obj - Containing all the *.o files
- ◇ out - Folder used for the output files
- ◇ src - Source code files including the makefile

and four programs with the following functions:

- ◇ drfmatrix - Calculation of the system matrix
- ◇ csr3toimg - Generation of a sensitivity maps of the system matrix
- ◇ adaptsens - Modifying the system matrix taking into account the individual sensitivity of each detector
- ◇ csrmlm - ML-EM reconstruction code

drfmatrix calculates the system matrix based on the DRF model and stores the matrix in the csr3-compressed format with the following command:

```
mpirun -hostfile mpi/hostfile -np <(number of nodes)×(number of slots)> bin/drfmatrix  
cfg/<inputfile>(*.petconfig) sm/<systemmatrix>(*.csr3) <integral-precision>
```

hostfile: Describes the architecture of the cluster

<(number of nodes)×(number of slots)>: Defines how many nodes and slots from the cluster shall be used

<inputfile>(*.petconfig): Configuration file for the PET geometry

<systemmatrix>(*.csr3): Output file for the system matrix

<integral-precision>: Integral precision used to calculate the system matrix entries

csr3toimg creates a three- or two-dimensional sensitivity map for a given system matrix and saves it in a *.img file, which can be open and analysed with the open source

program amide.

```
mpirun -hostfile mpi/hostfile -np <(number of nodes)×(number of slots)> bin/csr3toimg
sm/<systemmatrix>(*.csr3)
```

adaptsens offers to modify a system matrix taking into account the individual sensitivity of each detector.

```
./adaptsens <inputmatrix>(*.csr3) <outputmatrix>(*.csr3) <listfile>(*.txt)
```

<inputmatrix>(*.csr3): Input system matrix in a *.csr3 file format

<outputmatrix>(*.csr3): modified system matrix in a *.csr3 file format

<listfile>(*.txt): File containing the individual sensitivity of all detectors in a ASCII file

csrmlm reconstructs a input file for a given system matrix using an ML-EM reconstruction algorithm.

```
mpirun -hostfile mpi/hostfile -np <(number of nodes)×(number of slots)> bin/csrmlm
sm/<systemmatrix>(*.csr3) in/<Truesfile>(*.LMsino) -g <bpr> <bpc> <block col-
umn width> <iterations> <iteration step> out/<outputfile>(*.img)
```

<inputmatrix>(*.csr3): Input system matrix in a *.csr3 file format

<Truesfile>(*.LMsino): Input file generated by measurement or a simulation

<bpr>,<bpc>,<block column width>: This parameters describe how the system matrix is distributed an the cluster. <bpr> and <bpc> should be chosen with respect to the architecture specified in the hostfile. For the <block column width> a value of 200000 was found to be an appropriate value.

<iterations>: Number of iterations

<iteration step>: Iteration step after which a new output file will be written.

<outputfile>: Output file in a *.img file format

Acknowledgments

Zuerst möchte ich mich bei Frau Professor Ziegler bedanken für die Bereitstellung des sehr interessanten Themas, für das entgegengebrachte Vertrauen und die Betreuung dieser Arbeit. Ich habe mich in Ihrer Gruppe immer sehr wohlgefühlt.

Dann möchte ich mich bei Herrn Professor Böni bedanken, der die Betreuung dieser externen Arbeit von Seiten des Physikdepartements übernommen hat und stets für fachliche Gespräche zur Verfügung stand.

Weiterer Dank gebührt Tilman Küstner für die Zusammenarbeit und Implementierung des DRF-Modells und der Rekonstruktionsalgorithmen auf einer Clusterarchitektur. Danke für deine Unterstützung bei allen Belangen der Programmierung und Implementierung, für die Bereitschaft neue Ideen mit mir zu diskutieren und schließlich umzusetzen.

Außerdem geht ein großes Dankeschön an Irene Torres-Espallardo. Auch wenn unsere gemeinsame Zeit am Klinikum nur sehr kurz war, so war sie doch für mich sehr wertvoll. Danke für die umfassende Einführung in GATE und PET-Rekonstruktion sowie die Bereitschaft und Geduld mir auch über größere Entfernung hinweg alle meine Fragen zu beantworten.

Besonderer Dank gilt natürlich auch meinen beiden engsten Mitstreitern Jožef Pulko und Florian Schneider. Danke Jožef für die zahlreichen Diskussionen über SiPMs und Statistik, deine große Begeisterung für das Lösen komplizierter Gleichungssysteme bis hin zur umfangreichen Erweiterung meines Slowenischen Wortschatzes. Najlepsa ti hvala! Imela sva nekaj dobrih trenutkov skupaj. Danke Florian für deine Hilfe bei sämtlichen Messungen an MADPET und MADPET-3 von denen einige doch sehr zeitaufwendig waren, für deine Einführung in SolidWorks womit ich einen Großteil der Zeichnungen und Abbildungen in dieser Arbeit angefertigt habe und auch dafür, daß du auch sonst immer ein offenes Ohr für Probleme diverser Natur für mich hattest. Ich habe die Zusammenarbeit mit euch beiden sehr genossen und geschätzt.

Großer Dank geht auch an Ralph Bundschuh, der mich immer in allen Lebenslagen unterstützt hat und nicht zuletzt für seine Freundschaft.

Schließlich möchte ich mich bei meinen Eltern Renate und Peter Hohberg bedanken, die mir nicht nur diese Ausbildung und Studium ermöglicht haben sondern mich auch sonst in jeder Hinsicht immer unterstützt haben und mich meinen eigenen Weg gehen lassen. Danke!

